Ida Lægreid Andersen

The Effect of Exposure to Elevated Temperatures on the Mechanical Properties of Age Hardenable AlMgSiCu-Alloys

June 2019

Master's thesis

2019

Ida Lægreid Andersen

NTNU
Norwegian University of
Science and Technology
Faculty of Natural Sciences
Department of Materials Science and Engineering

NTNU
Norwegian University of
Science and Technology

NTNU
Norwegian University of
Science and Technology

NTNU

Norwegian University of
Science and Technology

The Effect of Exposure to Elevated Temperatures on the Mechanical Properties of Age Hardenable AlMgSiCu-Alloys

Ida Lægreid Andersen

Materials Science and Engineering
Submission date: June 2019
Supervisor: Bjørn Holmedal
Co-supervisor: Feng Lu

Norwegian University of Science and Technology
Department of Materials Science and Engineering

Preface

This project report is submitted as the product for *TMT4905 - Materials Technology, Master's Thesis* at the Norwegian University of Science and Technology (NTNU). The research has been conducted at the Department of Materials Science during the spring of 2019. The work is a continuation of the author's project thesis from the autumn of 2018.

The work is part of the competence project Aluminium alloys with Mechanical Properties and ElectRical conductivity at Elevated temperatures (AMPERE). Research partners in the project are NTNU and SINTEF, and industrial partners are Hydro, Hydro Extruded Soutions, Nexans, Raufoss Technology Neuman and Gränges. An aim for the project is to investigate correlations between microstructure, mechanical properties and electrical conductivity at elevated temperatures. This work is part of Work package 2, which concerns mechanical properties.

I would like to thank my supervisor Professor Bjørn Holmedal for his competent supervision and enthusiasm for my work. I would also like to thank my co-supervisor PhD candidate Feng Lu for close cooperation this year, and for always being available. Thank you to Postdoctoral Fellow Tomas Manik for taking the time to perform FEM analysis during his paternity leave, and to Chief Engineer Pål Christian Skaret for his help with set up and execution of experiments.

Finally, I would like to thank my friends and family for all their support, and my fellow students for five nice years in Trondheim.

Abstract

With the increased demand for light, strong materials for the automotive industry comes an increased demand for knowledge on the mechanical properties of these materials. It is well known that age hardenable aluminium alloys have a high strength due to a large density of second phase precipitates, but their work hardening behaviour is not fully understood.

In this thesis, the effect of exposure to elevated temperatures on mechanical properties and work hardening behaviour for three age-hardenable aluminium alloys with silicon, magnesium and copper as the main alloying elements has been studied. Specimens of the alloys were solution heat treated and artificially aged at 180°C to a series of underaged and overaged conditions. Tensile tests were performed at room temperature, 100°C and 150°C with synchronized image capturing.

True stress-strain curves and work hardening curves (Kocks-Mecking curves) were constructed. From the curves, key values describing the mechanical properties were determined. The values are the basis for a discussion about the mechanical properties and interaction between dislocations and precipitates at various aging conditions.

The results show that the tolerance for overaging of the strength increases with increasing copper content, both in regards to overaging and elevated temperature during deformation.

Based on the work hardening behavior, an aging time between 24 hours and 1 week is suggested as the transition point for shearable and non-shearable precipitates.

Sammendrag

Med et økt behov for lette, sterke materialer for bilindustrien, kommer også et økt behov for kunnskap om de mekaniske egenskapene til disse materialene. Det er godt kjent at utherdbare aluminiumlegeringer har høy styrke på grunn av en høy tetthet av presipitater av en annen fase enn matriksmaterialet, men arbeidsherdingsegenskapene er ikke fullstendig avklart.

I denne avhandlingen blir effekten av å utsettes for økte temperaturer på de mekaniske egenskapene og arbeidsherdingsoppførselen til tre utherdbare alumiumlegeringer med silisium, magnesium og kobber som hovedlegeringselemeter studert. Prøver av legeringene ble innherdet og kunstig eldet ved 180°C. Strekktester ble utført ved romtemperatur, 100°C og 150°C med synkronisert bildeopptak. Sanne spenning-tøyning kurver og arbeidsherdingskurver (Kocks-Meckingkurver) ble konstruert. Fra kurvene ble nøkkelverdier som beskriver de mekaniske egenskapene bestemt. Verdiene er basis for en diskusjon rundt de mekaniske egenskapene og interaksjonen mellom dislokasjoner og presipitater ved ulike eldingstilstander.

Resultatene viser at toleransen for overelding til styrken øker med økende kobberinnhold, både når det gjelder overelding og ved økt temperatur under deformasjon.

Basert på arbeidsherdingensoppførselen, foreslås en eldingstid mellom 24 timer og en uke som punktet hvor presipitatene går fra å være skjærbare til å bli ikke-skjærbare.

Table of Contents

1 Introduction

In recent years,the use of age-hardened aluminium alloys for structural parts in the automotive industry has increased. Because aluminium is a light metal, this is an important step towards achieving more environmentally friendly transportation with a lower fuel consumption. According to the European Aluminium Association, the amount of aluminium in the average car has increased from 50 kg in 1990 to 151 kg in 2016 [1].

Replacing the steel in crash components for vehicles could give a weight reduction of up to 40% [2]. However, the weight reduction cannot be on the expense of safety. The purpose of the crash management system in a vehicle is to absorb a large amount of energy in case of a car crash by deforming, as shown in Figure 1.1. The goal is to prevent passengers from being injured and the vehicle itself from serious damage.

Figure 1.1: Crash component before and after deformation. Image from [2]

The age hardenable aluminium alloys from the AA6XXX and AA7XXX-series have great potential, due to high strength, formability and corrosion properties [3]. The high strength of the age hardenable aluminium alloys is mainly due to precipitates from alloying elements, which form during heat treatment. The strength is determined by the duration and temperature of the heat treatment, as well as the composition of the alloy.

The crash compnent is located close to the brakes, and can be heated during operation of the vehicle. This is one of the reasons why the tolerance of materials for high temperature applications is so important.

The development of yield strength with aging time has been studied extensively, but how work hardening behaviour is affected, especially up to large strains, is not fully understood [4]. The work hardening behaviour for an age hardenable alloy is affected by the interaction between dislocations and precipitates.

The aim of this thesis is to study the mechanical properties and work hardening behavior for three aluminum alloys in the 6XXX-series at three different temperatures after various heat treatment.

2 Theory

2.1 Stress and strain

Stress is defined as the intensity of force at a point [5]. If the force is uniformly distributed, the stress is given by equation 2.1, where P is the force and A is the area.

$$\sigma = \frac{P}{A} \tag{2.1}$$

If the object subjected to the force is deformed, the area will change, and one must distinguish between the true stress, as presented in equation 2.1, and the engineering stress, presented in equation 2.2, where A_0 is the area before deformation.

$$s = \frac{P}{A_0} \tag{2.2}$$

If a small cubic volume element of a material is considered, the stress acting on it can be split into nine components, as illustrated in Figure 2.1. The components can be presented as a stress tensor, as in equation 2.3.

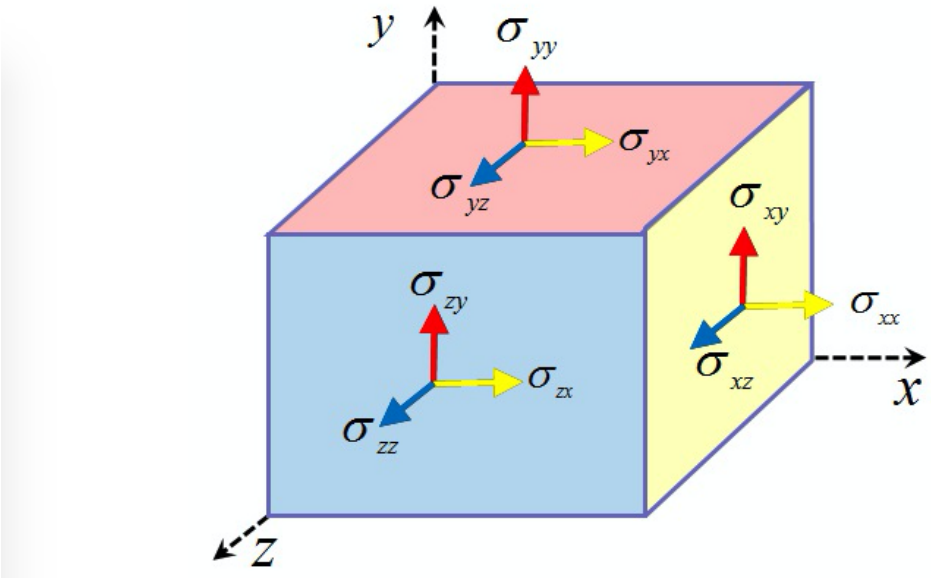

Figure 2.1: Stress components on a volume element. Figure from [6]

$$\sigma = \begin{bmatrix} \sigma_{xx} & \sigma_{xy} & \sigma_{xz} \\ \sigma_{yx} & \sigma_{yy} & \sigma_{yz} \\ \sigma_{zx} & \sigma_{zy} & \sigma_{zz} \end{bmatrix} \tag{2.3}$$

The first subscript is the direction if the normal of the plane the stress is acting on. The second subscript is the direction of the stress component. If the subscripts are the same, it is a normal stress component. If they are different, it is a shear stress component, and is usually labeled τ_{ij}. Additionally, $\tau_{ij} = \tau_{ji}$, due to moment balance of the element. Equation 2.3 can be changed to Equation 2.4.

$$\sigma = \begin{bmatrix} \sigma_{xx} & \tau_{xy} & \tau_{xz} \\ \tau_{xy} & \sigma_{yy} & \tau_{yz} \\ \tau_{xz} & \tau_{yz} & \sigma_{zz} \end{bmatrix} \tag{2.4}$$

Strain is the measure of deformation. An elastic strain is when the deformed shape returns to its original shape when the stress is removed. A plastic strain is a permanent deformation, where the shape does not return to its original shape.

Normal strains come from changes in length and thickness. The strain in the length direction is considered. The simplest method to measure the strain is by applying the engineering strain equation, given in Equation 2.5.

$$e = \frac{L - L_0}{L_0} \tag{2.5}$$

Here, L_0 is the initial extensometer length and L is the instantaneous extensometer length. Equation 2.5 is accurate for small strains, but for larger strains, it must be taken into account that the gauge length changes during the deformation. This is done with the true strain, ϵ, where the total strain is measured as the sum of smaller strain contributions. Each contribution is found similarly as in Equation 2.5 but the gauge length is updated for each contribution, as shown in Equation 2.6.

$$\epsilon_{zz} = \frac{L_1 - L_0}{L_0} + \frac{L_2 - L_1}{L_1} + \frac{L_3 - L_2}{L_2} + ... \tag{2.6}$$

If the length changes are infinitesimal, the expression can be integrated to the definition of true strain, given in Equation 2.7.

$$d\epsilon_{zz} = \frac{dL}{L} \rightarrow \epsilon_{zz} = ln\left(\frac{L}{L_0}\right) \tag{2.7}$$

A shear strain is a change in the angle between two lines, as illustrated in Figure 2.2, where the right angles are changed by θ.

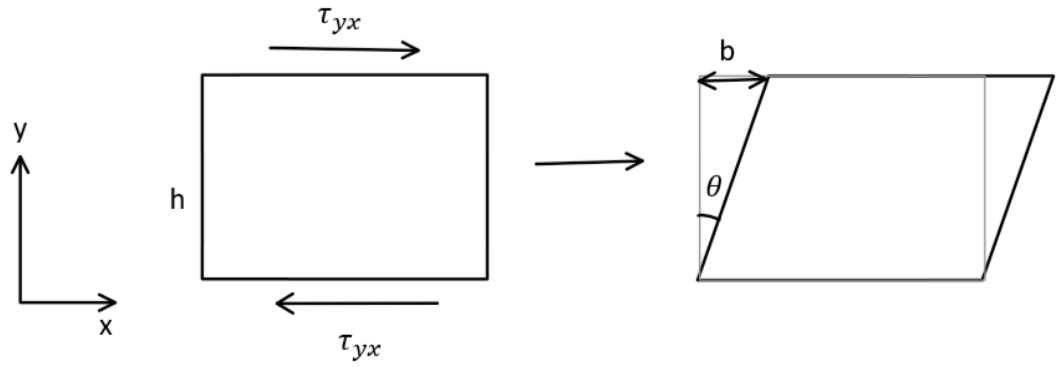

Figure 2.2: Shear strain

The engineering shear strain is defined as the tangent of the angle, but for small angles the shear strain can be approximated as the angle itself.

$$\gamma = \tan\theta = \frac{b}{h} \approx \theta \tag{2.8}$$

Engineering shear strain is not an optimal measure of deformation because a pure rotation will be counted as a strain by the definition in Equation 2.8. Also, the engineering shear strain is not symmetric. The true shear strain can be determined by splitting the shape change into a pure rotation term and a pure deformation term. This is illustrated in Figure 2.3 for the same deformation as in Figure 2.2.

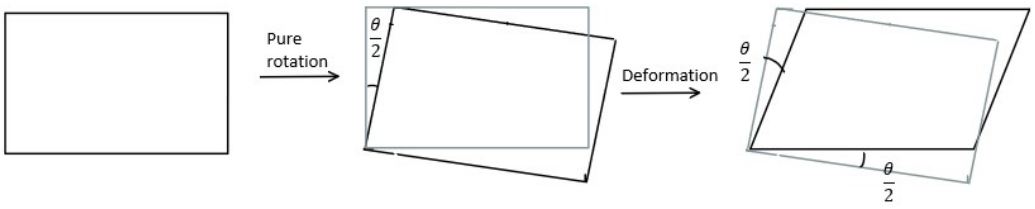

Figure 2.3: True shear strain

Comparison of Figures 2.2 and 2.3 illustrates that $\epsilon_{xy} = \epsilon_{yx} = \frac{\gamma}{2}$, where ϵ_{xy} and ϵ_{yx} are the true shear strain components for two dimensions. The true engineering strain is symmetric, and pure rotation is ignored.

2.2 Crystal structure of aluminium and deformation by slip

2.2.1 The FCC unit cell

The atoms in a metal are arranged in a crystal structure. In the structure, repeated units can be found, and the smallest repeated unit is called the unit cell of the structure. The unit cell for the structure of aluminium is called face-centered cubic (FCC). The position of the atoms for the FCC unit cell is illustrated in Figure 2.4. There is an atom in each corner and on each side of the cube.

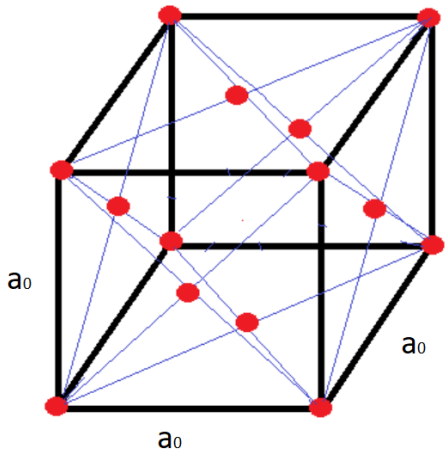

Figure 2.4: The position of atoms in an FCC unit cell

An axis system placed in one of the corners can be used to define crystallographic planes and directions. These are described by Miller indices. Crystallographic planes (hkl) are defined by the reciprocal of the intersection between the plane and the axes. Because the axes can be placed in an arbitrary corner, every plane will have different, equivalent sets of Miller indices. A set of equivalent planes is called a family of planes, $\{hkl\}$. The indices of crystallographic directions $[uvw]$ are found with the same method as when finding vector components. A set of equivalent directions is called a family of directions, $\langle uvw \rangle$.

2.2.2 Dislocations

Dislocations are line defects in a crystal structure. Their existence was proposed to explain the low yield strength observed in crystals, compared to the theoretical value if no crystal defects were assumed [7]. If the condition for yielding was gliding of the whole plane, the critical shear stress for pure copper would be 414 MPa, while the observed value is 1 MPa [5]. Taylor, Orowan and Polanyi explained this deviation between theory and practice by line defects, called dislocations, and that slip could occur stepwise by dislocation movement [5].

The two special types of dislocations are called edge and screw dislocations. An edge dislocation is an extra half-plane in the crystal. The edge dislocation, as well as slip by glide of an edge dislocation, is illustrated in Figure 2.5.

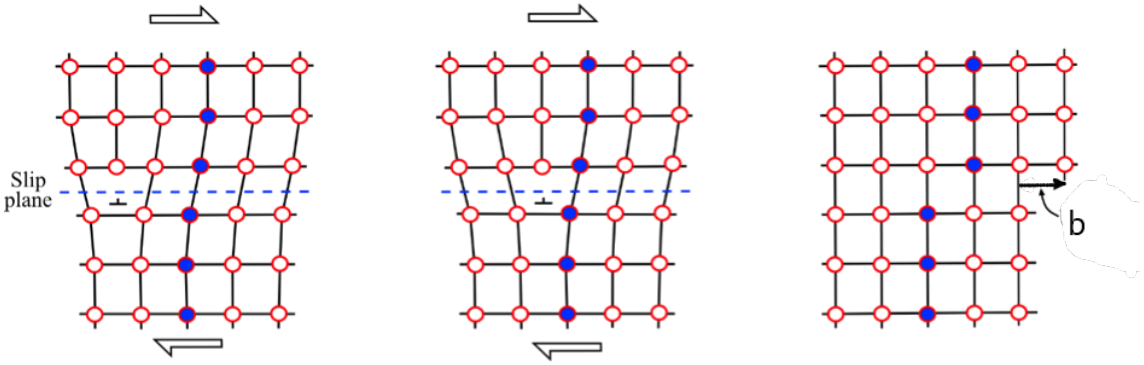

Figure 2.5: The edge dislocation. Figure from [8]

A screw dislocation, illustrated in Figure 2.6, can be imagined as a part of the crystal being shifted one atomic distance relative to other parts. In Figure 2.6, the line between A and B represents the border between the deformed and the undeformed crystal.

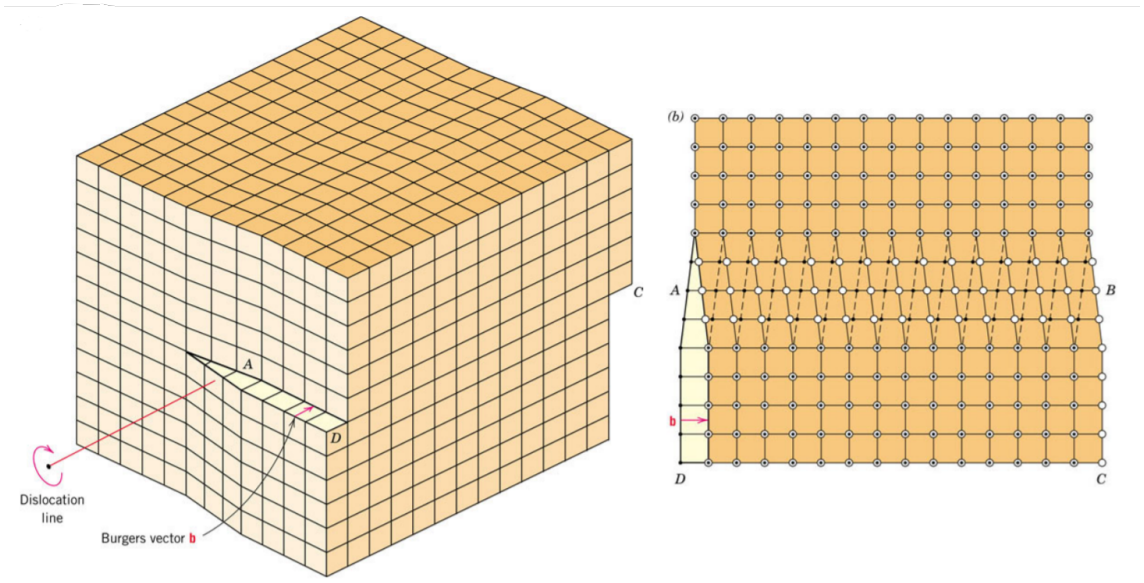

Figure 2.6: The screw dislocation. Figure from [9]

In general, dislocations have both edge and screw components. These are called mixed dislocations.

The magnitude and direction of the the deformation caused by one dislocation is called Burgers's vector of the dislocation. The direction of the Burger's vector is the the same as the close-packed direction the dislocation

glides in. The magnitude is the atomic distance in the close-packed direction. The Burger's vectors for both edge dislocations and screw dislocations are illustrated in Figures 2.5 and 2.6 respectively.

2.2.3 Dislocation glide in FCC single crystals

A dislocation can glide in a slip system, which consists of a crystallographic plane and a direction in the plane. The slip planes are usually the most densely placed planes in the crystal, and the direction is close packed. In FCC crystals, the slip systems are made up of the close packed $\{111\}$-planes and the $\langle 110 \rangle$-directions, in total 12 systems.

The magnitude and direction of the resolved shear determine which systems are activated. If a single crystal is subjected to a force P, as illustrated in Figure 2.7, the resolved shear stress component τ_R in the different slip systems is determined by the orientation of the slip system.

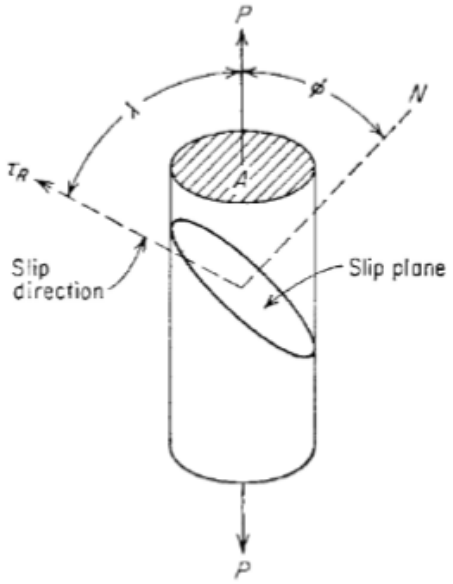

Figure 2.7: Uniaxial stress applied to a single crystal. Figure from [7]

If ϕ is the angle between the direction of the applied stress and the slip plane normal, and λ is the angle between the applied stress and slip directions, the resolved shear stress component is given by Equation 2.9, where m is defined as the Schmid factor.

$$\tau_R = \frac{P}{A} cos\phi cos\lambda = \sigma m \tag{2.9}$$

Schmid hypothesized that τ_R is the only stress component controlling the glide [5]. Glide will occur first in the slip system with the largest Schmid factor, given that τ_R is larger than the critical resolved shear stress. This is the primary slip system, and this is called Stage I of deformation. How the critical resolved shear stress changes with strain is illustrated in Figure 2.8. The concept of strain hardening is explained further in Section 2.3.

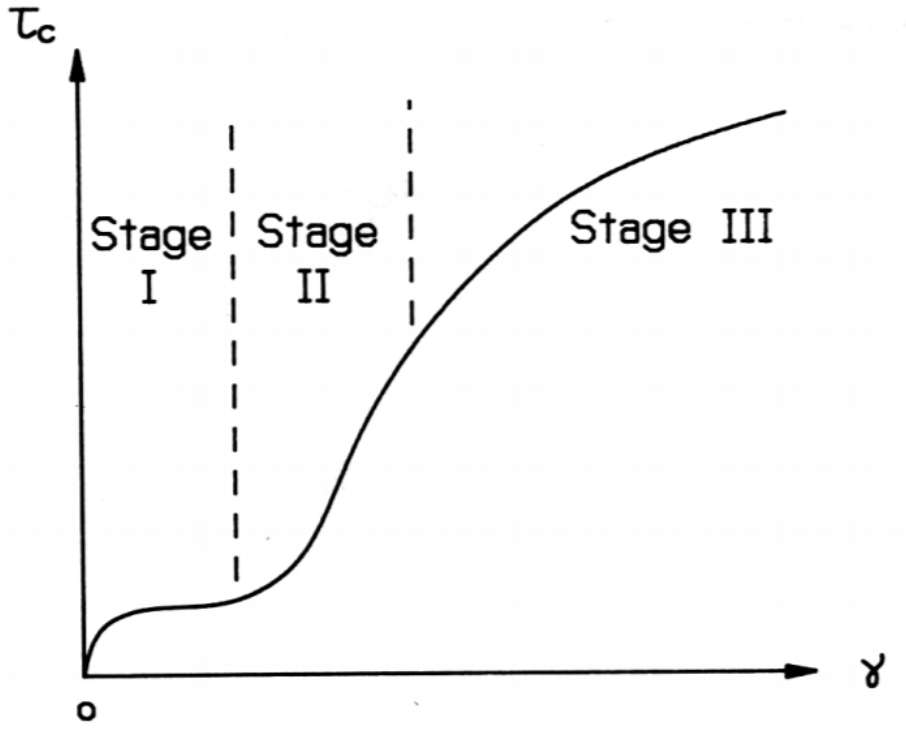

Figure 2.8: Stages of deformation for single crystal

The slip causes rotation of the slip planes, and at some point, multiple slip systems will be activated because they have the same Schmid factor [7]. This marks the transition to Stage II, which is characterized by a linear increase in critical resolved shear stress with strain. Stage III is characterized by a decreased slope. This is due to dynamic recovery of dislocations, which will be explained in Section 2.3.

2.2.4 Dislocation glide in FCC polycrystals

When tensile force is applied to a polycrystal, all the grains have their own orientation and set of angles λ and ϕ. This means that multiple slip systems will be activated. A consequence of this is that there is no Stage I stress-strain behaviour for polycrystals. Another consequence of multiple grains is that the deformation of each grain must be compatible with the deformation of its neighbouring grains. For a polycrystal, the connection between resolved shear stress in the glide planes and global stress, as well as the connection between the shear strain and the strain in the stress direction i given by equation 2.10. M is the Taylor factor, which is in the range of 2.5-3.5.

$$M = \frac{\sigma}{\tau} = \frac{\gamma}{\epsilon} \tag{2.10}$$

The stages of deformation for a polycrystal are illustrated in Figure 2.9

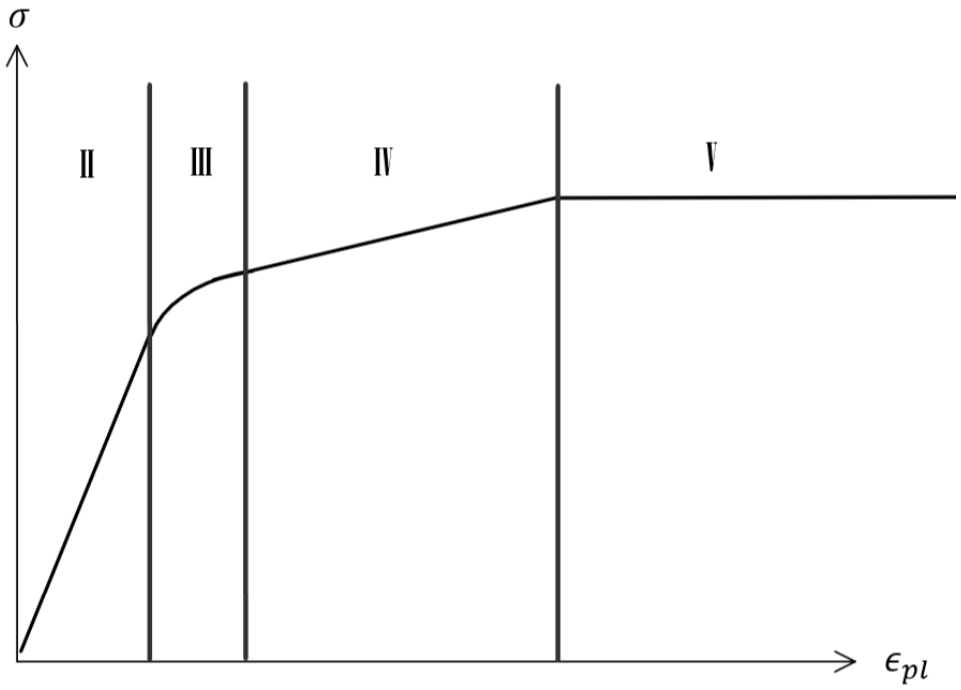

Figure 2.9: Stages of deformation of a polycrystal

Stage II and III have the same characteristics as in a single crystal. Stage IV has, similarly to Stage II, a linear increase in stress, but with a much lower slope. In Stage V the stress is constant.

2.2.5 Obstacles for dislocation glide

Obstacles in the glide plane make dislocation movement more difficult, and increase the resolved shear stress required for dislocation glide. Weak obstacles can be passed by dislocations, but the stress is increased due to elastic stress fields around the obstacles, which the dislocations interact with locally.

Strong obstacles cannot be deformed by dislocations. A dislocation which encounters a strong obstacle is forced to bow aroud it. When a critical curvature is reached, a loop is left around the obstacle, and the rest of the dislocation can glide further. This process is illustrated in Figure 2.10

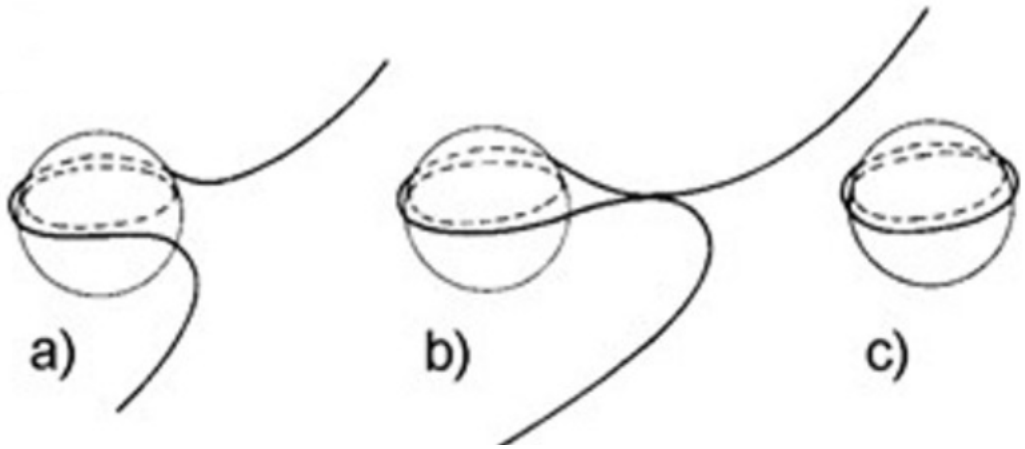

Figure 2.10: Dislocation bowing around strong obstacle. Figure from [10]

With an average distance between strong obstacles being λ or the density of strong obstacles being ρ, the required increase in resolved shear stress is given by Equation 2.11.

$$\tau_{strong\ obstacle} = \frac{Gb}{\lambda} \tag{2.11}$$

$\lambda \propto \frac{1}{\rho}$, so Equation 2.11 can be rephrased as Equation 2.12.

$$\tau_{strong\ obstacle} = \alpha G b \sqrt{\rho} \tag{2.12}$$

Equations 2.10 and 2.12 can be combined to determine the global stress increase, given in Equation 2.13.

$$\sigma_{strong\ obstacle} = M \alpha G b \sqrt{\rho} \tag{2.13}$$

2.3 Strain hardening

Much research has been devoted to describing how the strength of a material changes with deformation. This is called strain hardening or work hardening. A simple and empirical description of how the strength changes with plastic deformation is given by Hollomon's law, given in Equation 2.14.

$$\sigma = K \epsilon_p^n \tag{2.14}$$

K is called the strength coefficient, n is the strain hardening exponent and ϵ_p is the plastic strain.

There are different models that attempt to describe the development of strength with strain as the main variable, but for more accurate descriptions of the work hardening behavior, the microstructure of the material must be considered. In this section, a model where dislocation density is the only microstructural parameter is explained. Additionally, more sophisticated models with multiple parameters are introduced.

2.3.1 One-parameter model based on dislocation density

Stored dislocations act as pinning points for mobile dislocations, and an increase in dislocation density will give an increased strength. In this section, dislocations are assumed to be the only strong obstacles, with a density ρ_d. Inserted in Equation 2.12, the contribution to the strength because of dislocations is given by Equation 2.15.

$$\tau_{dislocations} = \alpha G b \sqrt{\rho_d} \tag{2.15}$$

where G is the shear modulus, b is the length of the burgers vector, and $\alpha \approx 0.3 - 0.5$ is a constant, accounting for not all dislocations acting as strong pinning points and their spacial distribution. The first model describing the change of the dislocation density with strain was published by Kocks in 1976 [11]. He proposed that the change in dislocation density was determined by a combination of storage and dynamic recovery of dislocations, as described by Equation 2.16.

$$d\rho_d = d\rho_{storage} - d\rho_{recovery} \tag{2.16}$$

The storage term is based on the statistical chance that a dislocation is stopped by obstacles in the crystal. A volume containing a glide plane with N dislocation sources is considered. The produced dislocation loops expand until they are pinned by obstacles and stored [12]. This is illustrated in Figure 2.11

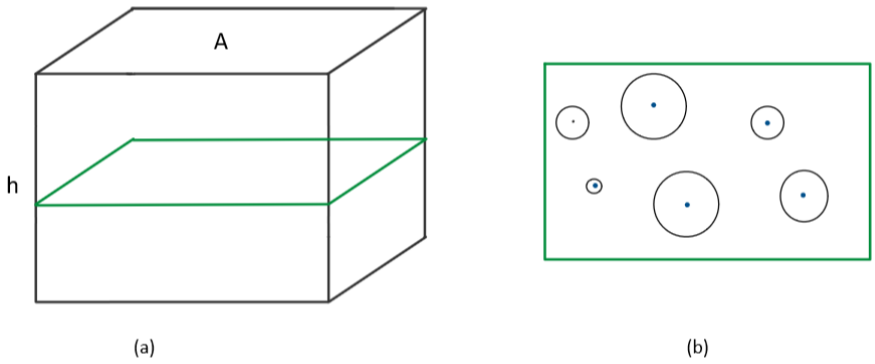

Figure 2.11: (a) Illustration of volume containing a glide plane (b) Top view of the glide plane with dislocation sources and stored dislocation loops.

The produced dislocation loops expand until they are pinned by obstacles and stored. The average radius of the stored loops is L. The increase in dislocation density due to these sources is given by Equation 2.17. n is the density of the dislocation sources and $2\pi L$ is the average dislocation length for each loop.

$$\Delta\rho_{storage} = 2\pi\frac{N}{V}L = 2\pi Ln \tag{2.17}$$

The loop expansion causes strain. First, the strain produced by one loop is considered. When the loop expands, the produced shear strain is $\Delta\gamma = \frac{\Delta l}{h}$ which is illustrated in Figure 2.12.

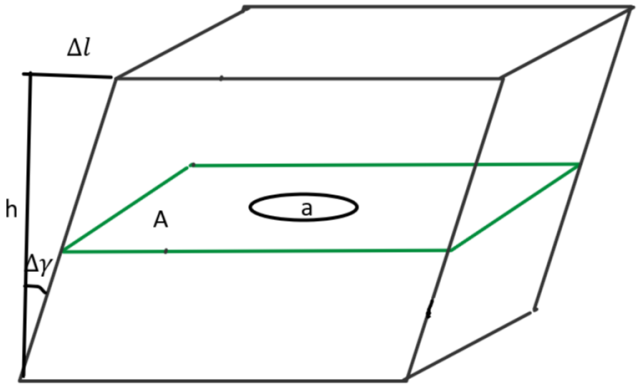

Figure 2.12: Shear strain from expansion of dislocation loop

When the loop expands to the edges of the volume, $\Delta l = b$, where b is the length of the Burger's vector. Earlier, Δl is between 0 and b. Similarly, the area inside the dislocation loop, $a = \pi L^2$, increases from 0 when $\Delta l = 0$ to A when $\Delta l = b$. This can be expressed as Equation 2.18.

$$\Delta l = \frac{a}{A}b \tag{2.18}$$

The resulting shear strain is given by Equation 2.19.

$$\Delta\gamma = \frac{\Delta l}{h} = \frac{ab}{Ah} = \frac{\pi L^2 b}{Ah} \tag{2.19}$$

When all N dislocation loops are considered, the total shear strain is given in Equation 2.20.

$$\Delta\gamma = N\frac{\pi L^2 b}{Ah} = n\pi L^2 b \tag{2.20}$$

Combination of Equations 2.17 and 2.20, gives a relationship between shear strain and dislocation density, given in Equation 2.21.

$$\frac{\Delta\rho_{storage}}{\Delta\gamma} = \frac{2\pi Ln}{n\pi L^2 b} = \frac{2}{bL} \rightarrow \frac{d\rho_{storage}}{d\gamma} = \frac{2}{bL} \tag{2.21}$$

The average slip length decreases with dislocation density, $L = \frac{c}{\sqrt{\rho}}$, where $c \approx 100$.

The dynamic recovery term, representing a decrease in dislocation density, comes from the process where opposite dislocations attract each other and annihilate. The process is illustrated in Figure 2.13.

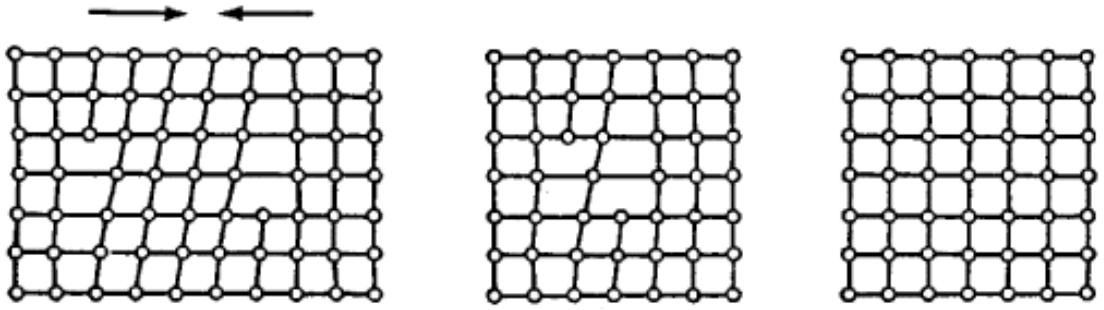

Figure 2.13: Annihilation of opposite dislocations. Figure from [13]

The dynamic recovery rate is proportional with dislocation density, because the dislocations are potential recovery sites for each other dislocations [11]. The development of dislocation density with strain becomes as presented in Equation 2.22.

$$\frac{d\rho}{d\gamma} = \frac{2}{bL} - K\rho \tag{2.22}$$

Equation 2.22 can be combined with Equations 2.15 and 2.10, to an equation describing the development of the stress towards saturation. This was presented by Voce [14], and is given in Equation 2.23.

$$\sigma_d = \sigma_{ds} - \sigma_{ds} \exp\left(\frac{\theta_0}{\sigma_{ds}}\epsilon^{pl}\right) \tag{2.23}$$

σ_{ds} is the saturation stress contribution for dislocations, θ_0 is the initial work hardening rate and ϵ^{pl} is the plastic strain. σ_{ds} and θ_0 are marked in Figure 2.15.

2.3.2 Multiparameter models

An assumption for the one-parameter model is that the dislocation density is the only microstructural parameter necessary to predict work hardening behaviour. However, when the dislocation density increases during plastic deformation, the dislocation density is not uniformly distributed. The dislocations arrange themselves to minimize the elastic lattice energy, and form substructures within the grains.

When the strain is relatively low, the dislocations are stored in a cell structure as illustrated in Figure 2.14 a. The quantities marked on the Figure are the cell size δ, the cell wall thickness h, the dislocation densities in the cell walls ρ_b, and the dislocation density within the cells, ρ_i.

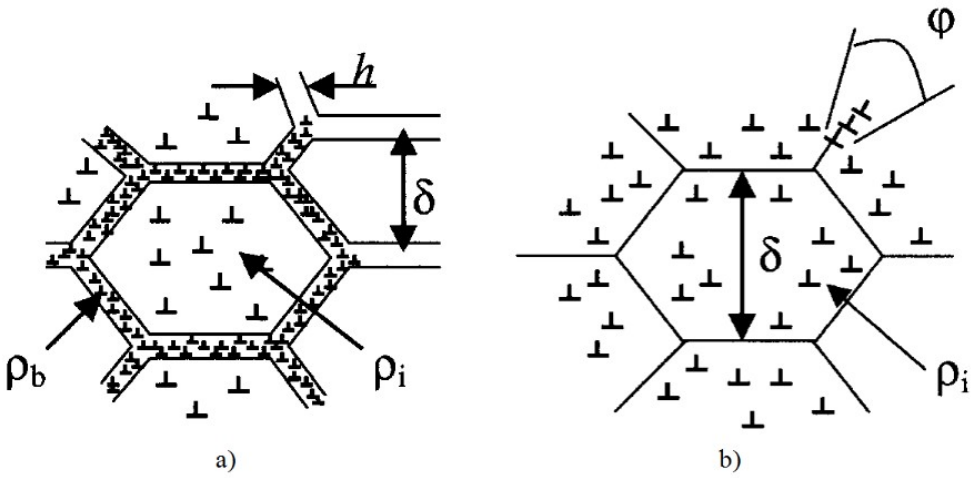

Figure 2.14: a) Cell-structure after small deformations. b) Subgrain structure after large deformation. Figure from [15]

For larger deformations, the cell walls collapse, and subgrains with a misorientation angle ϕ are formed, as illustrated in Figure 2.14 b. For the multiple parameter models, the microstructural evolution must be predicted, as well as the flow stress for a given microstructure.

Two multiparameter models were reviewed by Holmedal *et al.* [15], including the microstructural metal plasticity model, suggested by the same authors. In this model, the microstructural evolution is predicted by the cell size δ, the dislocation density within the cells ρ_i, and the misorientation angle ϕ.

The second model was the 3 internal variable model, suggested by Roters *et al.* [16]. In this model, the internal variables are the density of mobile dislocations, the density of immobile dislocations in the cell, and the density of immobile dislocations in the cell walls.

2.3.3 Kocks-Mecking plots

A convenient method of examining the strain hardening behavior of a material is to find the derivative of the flow stress with respect to the strain, in other words, the instantaneous work hardening rate $\theta = \frac{d\sigma}{d\epsilon}$. The derivative plotted against $\sigma - \sigma_y$, where σ_y is the yield strength of the material, is called a Kocks-Mecking plot. A schematic Kocks-Mecking plot is illustrated in Figure 2.15.

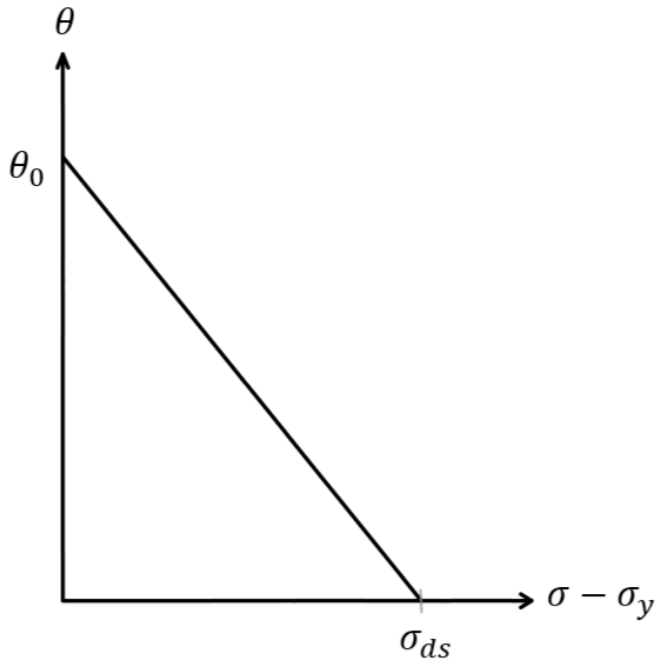

Figure 2.15: Schematic Kocks-Mecking plot. σ_{ds} and θ_0 are marked.

2.4 Precipitation hardening

In age hardenable aluminium alloys, a large strength contribution comes from precipitates of secondary phases in the aluminium matrix. The strength contribution depends on the size, structure and coherency of the precipitates.

Precipitation hardening is achieved by heat treatment in two steps. First, the alloy is heated to a high temperature in the one-phase region of the phase diagram. At this stage, all the alloying elements are in solid solution. Then it is quenched in cold water. With the lower temperature, the solid solution is not termodynamically stable, but due to slow kinetics, the elements stay in a supersaturated solid solution (ssss) with a high quenched-in vacancy concentration [17]. The next step is aging, which means heating the alloy again, but keeping the temperature within the two-phase region of the phase diagram. Due to the increased temperature, the kinetics are faster, and the alloying elements form precipitates. Depending on aging time, temperature and composition of the alloy, different precipitate structures are formed. Hardness as a function of aging time at 185°C for alloy AA6082 is given in Figure 2.16.

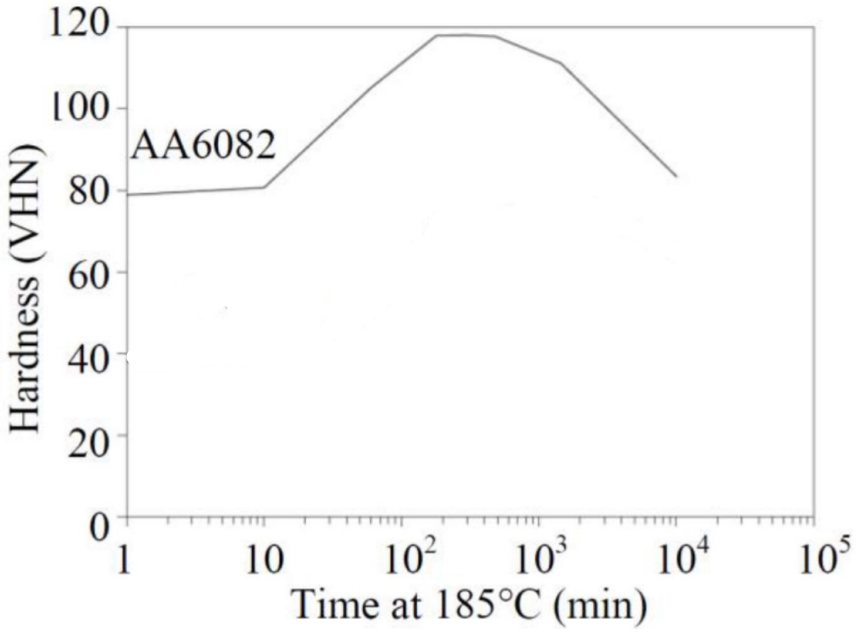

Figure 2.16: Development of hardness for alloy AA6082 with aging time. Figure from [18]

The strength increases with aging time until a peak is reached. The heat treatment where an alloy is solution heat treated and artificially aged to maximum strength is called T6. Solution heat treatment and artificially aging for a period shorter than required to reach the peak is called underaging, and for a longer time is called overaging or T7 [9] .

2.4.1 Coherency

Coherency describes the fit of the precipitate in the matrix. Coherency is one of the many factors which affect the interaction between dislocations and the precipitates. For coherent precipitates, the atom planes for the precipitate and the matrix are connected. Coherency strains in the matrix occurs if the planes are not perfectly connected. Coherent precipitates are illustrated in Figure 2.17 with (a) small and (b) large coherency strains. For semi-coherent precipitates, only some of the planes are connected, which is illustrated in Figure 2.17 (c), where the horizontal planes are connected with the matrix and precipitate are connected, but the vertical planes are not. A non-coherent precipitates have a structure which is very different from the matrix, as illustrated in Figure 2.17 d. Smaller precipitates are often coherent with the matrix, but lose coherency as they grow.

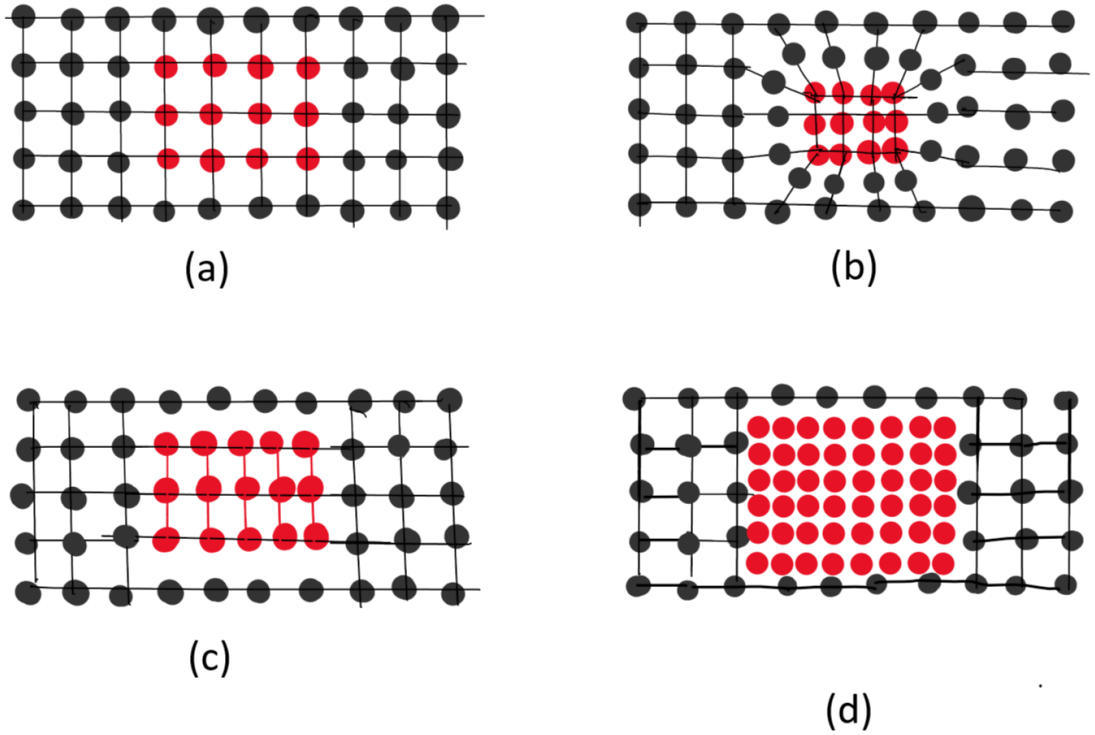

Figure 2.17: (a) A coherent precipitate with no lattice strains (b) A coherent precipitate with lattice strains (c) A semi-coherent precipitate (d) A non-coherent precipitate

2.4.2 Shearable precipitates

If a precipitate is shearable, it means that the dislocation can cut through and deform it in a similar manner as for the matrix. This is illustrated in Figure 2.18.

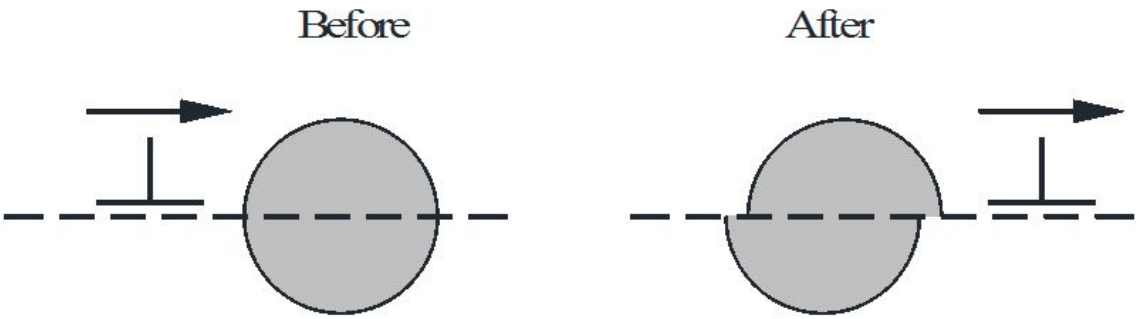

Figure 2.18: Cutting of a shearable precipitate. Figure from [19]

For a precipitate to be shearable, it has to be coherent. The strength of the alloy is increased by shearable precipitates for several reasons, described in [7] and [20].

- *Coherency strains.* As illustrated in Figure 2.17 (b), misfit strains can occur in the matrix around a coherent precipitate. This is similar as the misfit strains around an atom in solid solution. The increase in resolved shear stress due to the coherency strain increases with the difference between interatomic distance in the precipitate and in the matrix.
- *Formation of new surface.* When the precipitate is cut, new interphase surface between the precipitate and the matrix is created. Because of the surface tension, formation of new surface requires energy.
- *Breakdown of order.* When the precipitate is shifted, the bonds between the atoms are broken and new ones are formed on the shifting boundary. Often, this leads to a stacking fault, and bonds other than the preferred bonds are formed. This is illustrated in Figure 2.19.

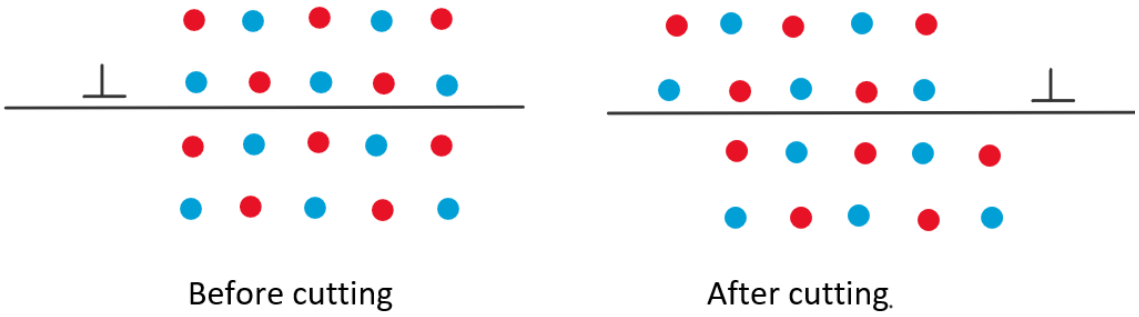

Figure 2.19: Breakdown of order and creation of a stacking fault after cutting of precipitate

- *Modulus effect.* The energy of the dislocation depends on the shear modulus. If the modulus of the precipitate is different from the modulus of the matrix, the energy of the cutting dislocation segment will be different than the other parts of the dislocation.

2.4.3 Non-shearable precipitates

Larger precipitates are typically not coherent, and thus not shearable. Coherent precipitates can also be non-shearable if the cutting energy large. In these cases, the dislocations will behave as the strong obstacles described in Section 2.2.5. If there is a volume fraction f of spherical precipitates with radius r, the average distance between neighbouring pinning points in Equation 2.11 is $\lambda \approx \frac{1.45r}{\sqrt{f}}$. The resulting strength contribution is given by Equation 2.24.

$$\tau_p = \frac{\alpha G b \sqrt{f}}{1.45r} \rightarrow \sigma_p = \frac{M \alpha G b \sqrt{f}}{1.45r} \tag{2.24}$$

A needle shaped precipitate will pierce more glide planes than a spherical precipitate with the same volume. Thus, for the same volume concentration, the obstacle density will be larger for needle shaped precipitates than for spherical precipitates. This is illustrated in Figure 2.20.

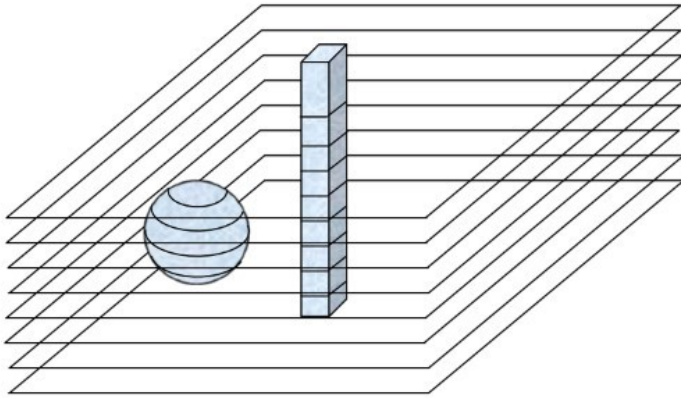

Figure 2.20: Glide plane piercing by spherical and needle shaped and precipitates. Figure from [18].

An expression for the distance between needle shaped precipitates in a FCC metal was derived by Holmedal [21]. If the precipitate length is l, the precipitate will pierce all the glide planes within a distance $\pm l \cos\theta$ from the precipitate center. θ is the angle between the length direction of the precipitates and the plane normal of the glide plane. The needle length is typically in the $\langle 001 \rangle$-directions, and the glide planes for FCC are the $\{111\}$-planes for a FCC metal. In a volume, number of precipitates with length l is given by the statistical distribution function $\phi_l\left(l\right)$. N_V is the total number of precipitates per volume. The area density P in the slip plane is given by equation 2.25.

$$P = \frac{\sqrt{3}}{3} \int_0^\infty \phi_l dl = \frac{\sqrt{3}}{3} N_V \bar{l} \tag{2.25}$$

With area density P, the average distance between the needle precipitates are $\lambda = \frac{1}{\sqrt{n}}$.

2.4.4 The Al-Mg-Si precipitation system

The quasi-binary phase diagram for Al-Mg_2Si was first presented by Kammer in 1999 [22]. The diagram has later been revised. The classic diagram with a modified solidus line (dotted) presented by Amado and Daroqui [23]

in 2005 is shown in Figure 2.21. Solutionizing is performed in the area labeled *Al solid solution*. The required temperature for achieving a solid solution depends on the composition. Artificial aging is performed at an elevated temperature within the area labeled *Al+Mg_2Si*.

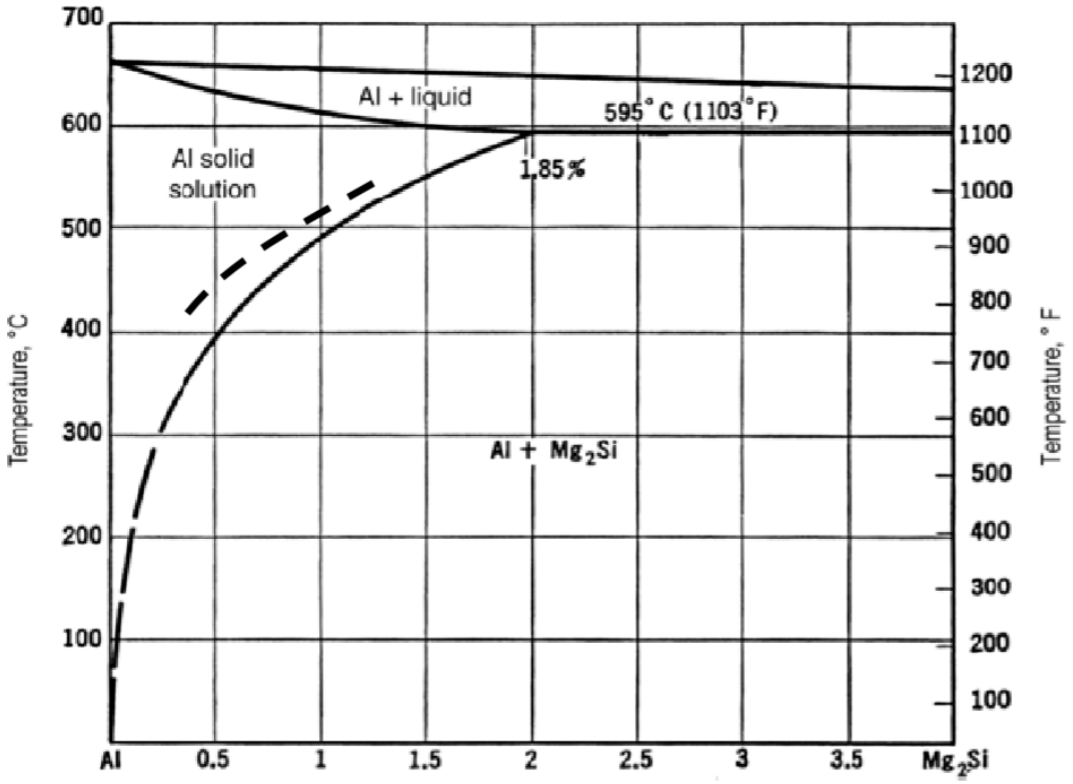

Figure 2.21: The quasi-binary for Al-Mg_2Si as presented by Amando and Daroqui [23]

The precipitation sequence for AlMgSi-alloys during artificial aging can be expressed as:

$$\alpha\left(ssss\right) \rightarrow atomicclusters \rightarrow GP-zones \rightarrow \beta'' \rightarrow \left(\beta' + B' + U1 + U2\right) \rightarrow \beta + Si \tag{2.26}$$

Atomic clusters can form at room temperature, but they can only grow to Guinier-Preson-zones (GP-zones) if the temperature exceeds 70°C. Atomic clusters and GP-zones have similar properties, but GP-zones have a higher concentration of solute atoms. The composition of the GP-zones are unknown, and they have a spherical structure [24].

The metastable β"-phase has a needle shape alligned with the <100>-directions of aluminium. The composition is Mg_5Si_6. The phase forms between 125°C and 200°C, and is the precipitate dominating at peak strength [17]. Formation of metastable β', U1, U2, B' occurs at overaging, with a loss of strength. The equilibrium phases β and Si-plates are formed at temperatures above 200°C [17].

2.4.5 Effect of addition of copper

Addition of copper to the AlMgSi-system has been shown to impact the precipitation system, even at impurity levels [25]. Murayama *et al.* [26] found that fine β'' precipitates were developed in an alloy containing 0.4 atomic % copper after aging time 30 minutes at 175°C, while only GP-zones were present in similar, but copper-free alloy. After aging time 10 hours, Cu was incorporated in the β''-precipitates. Additions of copper changes the precipitation sequence from Equation 2.26 to Equation 2.27 [3].

$$\alpha\left(ssss\right) \rightarrow atomicclusters \rightarrow GP-zones \rightarrow \beta'', L, QP, QC \rightarrow \beta', Q' \rightarrow Q \tag{2.27}$$

The size, shape and fraction of the precipitates after various aging times at 180°C have been studied in transmission electron microscope by PhD candidate Jonas Sunde [27] for the same three AlMgSiCu-alloys as are studied in this thesis. Table 2.1 show a selection of of the results. The results indicate that the degree of precipitate coarsening decreased with increasing copper content.

Table 2.1: Size and number density of precipitates at two aging times at 180°C for three AlMgSiCu-alloys.

Cu-content	Cross section area [nm^2]		Precipitate length [nm]		Number density [#/µm^3]	
	3 hours	24 hours	3 hours	24 hours	3 hours	24 hours
0.03	13	16	14	20	67024	46489
0.09	10	15	13	19	92898	47740
0.23	10	13	11	13	106525	79766

2.5 Combination of dislocations and precipitates

How the strength is affected by different obstacles has been explained, but determining the total strength, σ, of a material containing various strong obstacles is not trivial. For an alloy containing non-shearable precipitates in addition to stored dislocations, Equation 2.28 was suggested by Cheng *et al.* in 2003 [28].

$$\sigma = \sigma_{weak} + \left(\sigma_d^n + \sigma_p^n\right)^{\frac{1}{n}} \tag{2.28}$$

n is between 1 and 2, depending on the relative obstacle strength of the dislocations and the precipitates. The dislocations are strong obstacles, while the obstacle strength of the precipitates depends on their size and structure. If the obstacle strength of the precipitates is equal to the obstacle strength of dislocations, the total density of strong obstacles is the sum of the two densities. This is inserted in Equation 2.13, as in Equation 2.29, and the result is that in this situation n=2.

$$\sigma = M\alpha Gb\sqrt{\rho_d + \rho_p} \rightarrow \sigma^2 = M^2\alpha^2G^2b^2\left(\rho_d + \rho_p\right) \rightarrow \sigma = \left(\sigma_d^2 + \sigma_p^2\right)^{\frac{1}{2}} \tag{2.29}$$

If the dislocations are much stronger obstacles than the precipitates, the strong obstacle density is equal to the dislocation density. The increase in strength for other reasons than dislocation pinning is added directly, and n=1 [29]. As the precipitate strength is increased, n also increases until n=2, and the obstacle strengths of dislocations and precipitates are equal. If the obstacle strength of the precipitates is increased further, n is decreased .

During deformation, σ_d changes with strain as described in section 2.3, while σ_p can be assumed to remain constant. If this is true, Lu *et al.* [30] suggested that σ_p can be found from the yield strength for the alloy, σ_y, for pure aluminium, $\sigma_{y,pureAl}$ when a value for n is assumed, according to equation 2.30

$$\sigma_p = \left(\sigma_y^n - \sigma_{y,pureAl}^n\right)^{\frac{1}{n}} \tag{2.30}$$

Assuming n and σ_p to be constant, the contributions from dislocations in any point could be calculated from Equation 2.31

$$\sigma_d = \left(\sigma^n - \sigma_p^n\right)^{\frac{1}{n}} \tag{2.31}$$

The value for n was investigated by Cheng *et al.* [28] for different aging conditions for AA6111 and AA7030-alloys. They performed tensile tests and constructed Kocks-Mecking plots. They defined two parameters which could be read of the Kocks-Mecking plots, θ_{max} and $\frac{d\theta}{d\sigma}$. How they were determined from the two characteristic types of Kocks-Mecking plots they encountered, is illustrated in Figure 2.22.

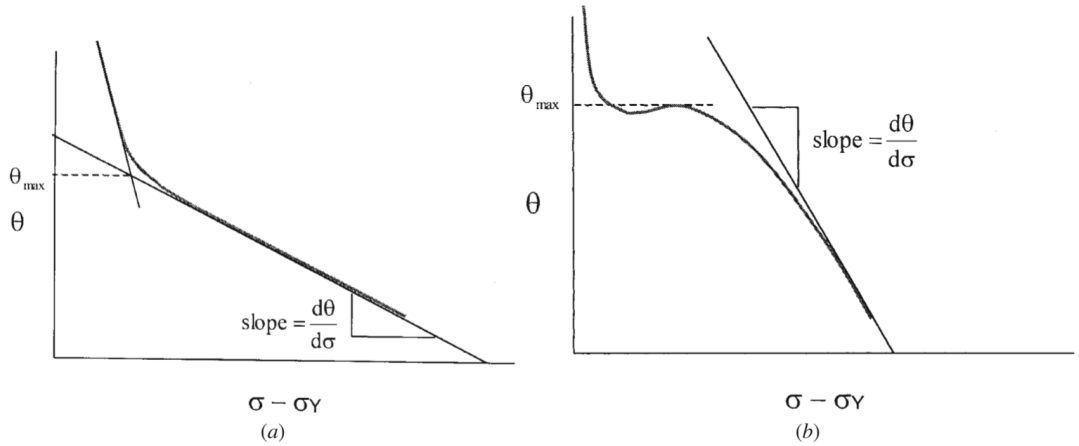

Figure 2.22: Kocks-Mecking plot with definition of the parameters θ_{max} and $\frac{d\sigma}{d\theta}$. Figure from [28]

$\frac{d\theta}{d\sigma}$ is defined as the slope in the linear section in the plastic regime, as illustrated in Figure 2.22(a). If there is no clear linear section, the slope was taken asymptotically as θ goes to zero. They showed that the physical basis of

$\frac{d\theta}{d\sigma}$ is directly proportional to the dynamic recovery rate. For n=1, $\frac{d\theta}{d\sigma} = \frac{-K}{2}$, where K is the constant in equation 2.22.

θ_{max} is defined as the maximum work hardening rate after the elastic transition if a maximum value exists, as illustrated in Figure 2.22(b). Otherwise, it is defined as the intersection between the extensions of the two linear sections, as illustrated in Figure 2.22(a). For n=1, $\theta_{max} = \theta_0$, the initial work hardening rate marked in figure 2.15, and is directly related to the storage rate for dislocations.

In their results, $\frac{d\theta}{d\sigma}$ was constant with aging time up to a certain point, where it started to increase rapidly. The explained this by an assumption that the recovery rate would not change significantly as long as the precipitates were shearable. Non-shearable precipitates will however be surrounded by loops as illustrated in Figure 2.10. The loops increase the recovery rate by both easy annihilation of loops around the same precipitate and annihilation by loops around adjacent precipitates. They estimated that the recovery rate when the precipitates were non-shearable would be twice as large after the shearable transition.

Their results for θ_{max} shows that the value decreases with aging time from underaged to peak aged. After peak aging time, the value was constant or slightly increasing up to a certain point where it increased rapidly. This was not directly linked to the shearable transition.

Their suggested shearable transition point was supported by comparison of their experimentally obtained curves with modeled work hardening behaviour for shearable and non-shearable precipitates.

2.6 The uniaxial tensile test

A common test for determining the mechanical properties of a metal is the uniaxial tensile test. A tensile test is performed by gripping both ends of a specimen of the material and applying a uniaxial force. The specimen is elongated until fracture, and the force required for elongating the specimen is registered. The tensile test is a common method for determining the following mechanical properties [31].

- Elastic deformaion properties, such as the modulus of elasticity (Young's modulus) and the Poisson's ratio
- Yield strength and ultimate tensile strength
- Ductility properties, such as elongation and reduction in area
- Strain-hardening characteristics

In this section, the methods for strain and flow stress measurement for the different stages of a uniaxial tensile test is described.

2.6.1 Stress measurement

Because the area is getting smaller during the tensile test, Equation 2.1 should be applied for stress measurement. As will be explained in Section 2.6.5, this equation is only valid until necking.

2.6.2 Strain measurement for an axisymmetric specimen

When an axisymmetric specimen is subjected to an applied stress σ_{zz} in the longitudinal direction z, the deformation will cause changes in both the diameter and the length of the specimen. Based on the length and diameter change, the longitudinal and transverse strain components can be calculated respectively. The longitudinal strain was presented in Equation 2.7, and the transverse strain is presented in Equation 2.32, where D_0 is the initial diameter and D is the instantaneous diameter.

$$\epsilon_{rr} = \frac{D}{D_0} \tag{2.32}$$

The strain components can be split into elastic parts, ϵ^{el} and plastic parts ϵ^{pl}. A simplified expression for determining the longitudinal strain when the transverse strain is known can be found by assuming that the elastic strain is negligible. In this case the volume is conserved, and Equation 2.33 is valid.

$$A_0 L_0 = AL \rightarrow \frac{L}{L_0} = \frac{A_0}{A} = \frac{D_0^2}{D^2} \tag{2.33}$$

Equation 2.7 and Equation 2.33 lead to the expression for finding the longitudinal strain based on the diameter change or on the transverse strain, presented in equation 2.34.

$$\epsilon_{zz} = 2ln\frac{D_0}{D} = -2\epsilon_{rr} \tag{2.34}$$

When the total strain is large, the plastic strain will dominate, and the error due to neglecting the elastic strain will be small. However, when the total strain is small, both terms must be considered. The splitting of the longitudinal and transverse strains into elastic and plastic parts are shown in equations 2.35 and 2.36, respectively.

$$\epsilon_{zz} = \epsilon_{zz}^{pl} + \epsilon_{zz}^{el} = \epsilon_{zz}^{pl} + \frac{\sigma_{zz}}{E} \tag{2.35}$$

$$\epsilon_{rr} = \epsilon_{rr}^{pl} + \epsilon_{rr}^{el} = \epsilon_{rr}^{pl} - \nu\frac{\sigma_{zz}}{E} \tag{2.36}$$

where E is the Young's modulus and ν is the Poisson's ratio. Due to volume conservation of plastic strain, the sum of plastic strain in the longitudinal direction and in two perpendicular transverse directions must be equal to zero. If the specimen is assumed to remain axisymmetric, the strain will be equal in all transverse directions.

$$\epsilon_{zz}^{pl} + \epsilon_{rr1}^{pl} + \epsilon_{rr2}^{pl} = \epsilon_{zz}^{pl} + 2\epsilon_{rr}^{pl} = 0 \tag{2.37}$$

Equations 2.36 and 2.37 can be combined to Equation 2.38

$$\epsilon_{zz}^{pl} = -2\epsilon_{rr}^{pl} = -2\left(\epsilon_{rr} + \nu\frac{\sigma_{zz}}{E}\right) \tag{2.38}$$

Combination of Equation 2.35 and Equation 2.38 leads to the expression in Equation 2.39, which is a more accurate measurement of longitudinal strain.

$$\epsilon_{zz} = \frac{\sigma_{zz}}{E} - 2\epsilon_{rr} - 2\nu\frac{\sigma_{zz}}{E} = \left(1 - 2\nu\right)\frac{\sigma_{zz}}{E} - 2\epsilon_{rr} \tag{2.39}$$

2.6.3 Elastic region

When a small force is applied to the specimen, the behaviour is elastic. This means that the specimen is deformed when the force is applied, but returns to its original shape when the force is removed. This is because the atoms are pulled apart, but not with a force that is large enough to cause dislocation glide. In this stress region the deformation is proportional to the applied stress. The proportionality constant is the bulk elasticity modulus, E. This deformation is called elastic strain. The relationship between stress and elastic strain is given by Equation 2.40.

$$\sigma_{zz} = E\epsilon_{zz}^{el} \tag{2.40}$$

After a certain load is applied to the metal specimen, relation between stress and strain ceases to be proportional. This point marks the onset of plastic deformation, which means that the specimen will not return to its original shape after unloading. Deformation after this point can be split into an elastic and a plastic part, as illustrated in Equation 2.35 in Section 2.6.2.

This point is called the elastic limit. A more common and convenient measurement for onset of plastic deformation is to find the stress required to produce a small amount of plastic deformation, typically 0.2%, corresponding to $\epsilon_{zz}^{pl} = 0.002$. The plastic component of the strain can be calculated by Equation 2.38.

2.6.4 Uniform plastic deformation

If the applied stress is larger than the yield strength, the specimen is elongated, and the cross section area is reduced. The material is strain hardened as explained in Section 2.3. The force required for deformation is increased by the strain hardening, but decreased by the area reduction, as shown in Equation 2.41.

$$\frac{dP}{d\epsilon} = \frac{d\sigma A}{d\epsilon} = \sigma\frac{dA}{d\epsilon} + A\frac{d\sigma}{d\epsilon} \tag{2.41}$$

If the required force is increased, the effect of strain hardening is larger than the effect of area reduction. However, a decrease in the force means that the area reduction dominates, and the condition is unstable. The necking point can be determined from the maximum force in the force-displacement curve. The stress in this point is called the true uniform strain, and is defined as Equation 2.42.

$$\sigma_u = \frac{F_{max}}{A} \tag{2.42}$$

2.6.5 Local plastic deformation

When the deformation is concentrated in a short section of the specimen, rather than uniform over the gauge length, it is called necking. This length section will receive a high local strain. After this point, there will be a lowered hydrostatic pressure in the neck and a non-uniform pressure distribution. The normal stress required for further deformation in the necking region will be lower than what is predicted by Equation 2.1, due to the contribution from the hydrostatic pressure in the center of the neck.

The stress distribution in the neck was studied for specimens with rotational symmetry around the longitudinal axis by Bridgman [32]. The minimal area was assumed to remain circular throughout the tensile test, and the neck contour was approximated by the arc of a circle, as illustrated in Figure 2.23. R is the radius of curvature for the neck arc, and a is the radius of the minimal cross section area. The axis of axisymmetry is also illustrated on the figure.

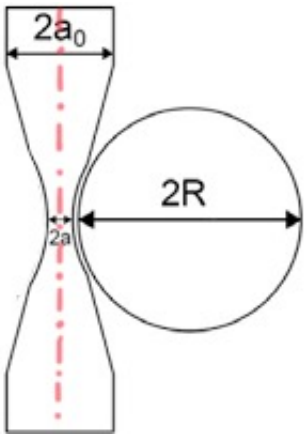

Figure 2.23: Illustration of radius of curvature and radius of minimal area in neck

Equation 2.43 was presented by Bridgman in 1944 as the first analytic expression for estimating the true stress in the neck.

$$\sigma = \frac{F}{A\left(1+\frac{2R}{a}\right) ln\left(1+\frac{a}{2R}\right)} \tag{2.43}$$

More advanced solutions have been suggested, but they can all be expressed as scaling factors on the form presented in Equation 2.44.

$$\sigma = \frac{F}{A\xi\left(\frac{a}{R}\right)} \tag{2.44}$$

An expression based on a second order series expansion was proposed by Gromada in 2011 [33].

$$\begin{aligned}
&\xi\left(\frac{a}{R}\right) = 1 - \frac{5\Lambda}{7\left(1+5\Lambda\right)} - \frac{2\left(1-6\Lambda\right)}{7\left(1+5\Lambda\right)} + \frac{2}{7} + \frac{30\Lambda\left(8\Lambda-\delta-5\delta\Lambda\right)}{49\delta\left(1+5\Lambda\right)^2} \\
&+\frac{3\left(8\Lambda-\delta-5\delta\Lambda\right)}{7\delta\left(1+5\Lambda\right)}\left(\frac{2\left(1-6\Lambda\right)}{7\left(1+5\Lambda\right)} - \frac{2}{7} - \frac{30\Lambda\left(8\Lambda-\delta-5\delta\Lambda\right)}{49\delta\left(1+5\Lambda\right)^2}\right) * \ln\left|1+\frac{7\delta\left(1+5\Lambda\right)}{3\left(8\Lambda-\delta-5\delta\Lambda\right)}\right| \\
&\delta = \frac{a}{R}, \Lambda = 1 - \frac{a_0}{a}
\end{aligned} \tag{2.45}$$

Unpublished work by Manik *et al.* [34] compared experimental tensile test data corrected with among others the Bridgman and Gromada correction factors, with finite element modelling and found that the Gromada correction was the most accurate.

The correction factors are functions of radius of the minimal cross section and radius of curvature in the neck. Because of this, the practical use of the correction factors require continuous tracking of the specimen geometry during the tensile test. This complicates the experimental setup and analysis of the results. In 1980, Leroy *et al.* [35] suggested a linear relation between the a/R-ratio and the true strain after necking.

$$\frac{a}{R} = 1.1\left(\epsilon - \epsilon_u\right) \tag{2.46}$$

2.6.6 Fracture

The tensile test ends at the fracture point. Fracture is classified by how much deformation the specimen takes before fracture. A fracture with little or no plastic deformation is called brittle. The more deformation, the more ductile is the fracture. A ductile fracture occurs after necking, by nucleation and growth of voids in the center of the neck [5].

The ductility of the specimen can be determined from the area reduction from the beginning of the test to fracture, Z. This is defined according to Equation 2.47 for round specimens.

$$Z = \frac{A_0 - A_f}{A_0} * 100\% = \frac{D_0^2 - D_f^2}{D_0^2} * 100\% \tag{2.47}$$

3 Method

3.1 AlMgSiCu-alloys

3.1.1 Materials and geometry

The compositions of the three aluminium alloys are given in Table 3.1.

Table 3.1: Composition for the aluminium alloys in weight percent

Alloy	Label	Si	Mg	Fe	Mn	Cu	Cr	Ti	V
Mg/Si>1 +Cu	M	0.64	0.77	0.26	0.26	0.23	0.02	0.02	0.007
AA6082	S	0.88	0.72	0.24	0.51	0.03	0.16	0.02	0.014
AA6082+0.1 Cu	C	0.88	0.64	0.2	0.45	0.09	0.14	0.03	0.007

Alloy S and C are both AA6082-alloys and alloy C has a larger copper content than S. Alloy M has a higher magnesium-silicon ratio the highest copper content.

Axisymmetric specimens for tensile test were machined from extruded bars. The gauge length was 18 mm, and the initial diameter of the cross section was 6 mm. The specimen geometry is illustrated in Figure 3.1. The specimen length direction was parallel to the extruded direction. The specimens were taken from close to the center of the bar, in order to avoiding the recrystallized surface layer and ensure a strong fiber texture.

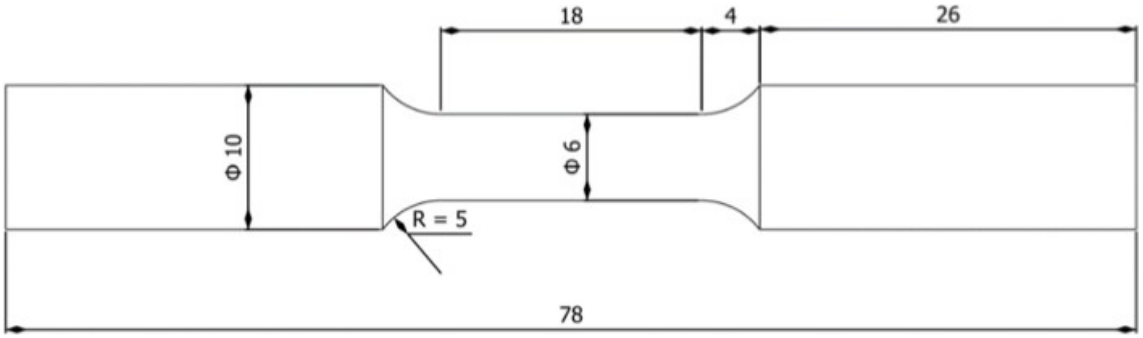

Figure 3.1: Specimen geometry

3.1.2 Heat treatment

Solutionizing was performed in a salt bath at 540°C for 12 minutes. Then the specimens were immediately quenched in cold water. After 10 minutes, the specimens were artificially aged in an oil bath. The oil bath

temperature was normally 180°C, but for three specimens of alloy S the aging temperature was 250°C. Their aging time was 24 hours. The heat treatment for aging temperature 180°C is schematically shown in Figure 3.2.

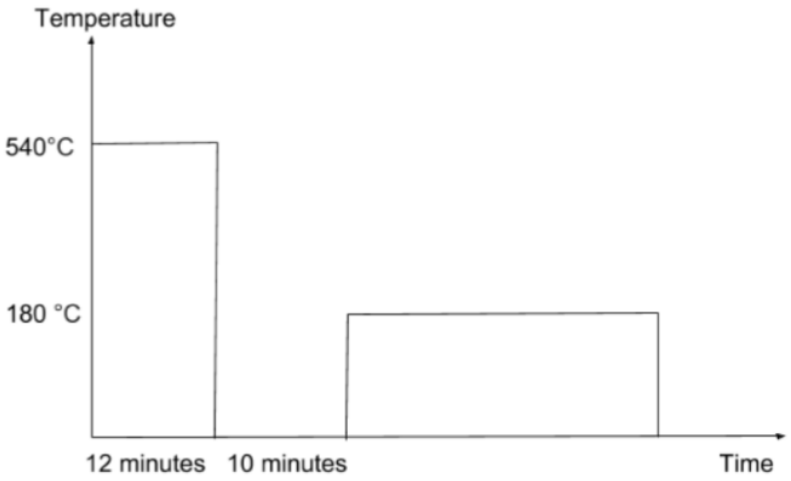

Figure 3.2: Heat treatment procedure for aging at 180°C

The aging times varied between 20 minutes and 1 month for the room temperature tests. For the elevated temperature tests it varied between 1 hour and 1 week. The aging times and number of parallels included are presented in Table 3.2

3.1.3 Tensile test

Tensile tests at room temperature were performed in fall 2018 for the author's project work. The experimental work for this Master's thesis is the tensile tests at 100°C and 150°C. Which aging times were tested at room temperature and elevated temperature, including the number of parallel tests, is given in Table 3.2. The reason for the reduced number of tests at 150°C was insufficient amounts of material.

Table 3.2: Aging times and number of parallels for tensile tests at room temperature, 100°C and 150°C.

	Room temperature			100°C			150°C		
	S	C	M	S	C	M	S	C	M
20 minutes	3	3	3	-	-	-	-	-	-
1 hour	3	3	3	3	3	3	3	3	1
3 hours	3	3	3	3	3	3	3	3	3
5 hours	3	3	3	-	-	-	-	-	-
12 hours	3	3	3	-	-	3	-	-	-
24 hours	3	3	3	3	3	3	3	3	1
3 days	-	3	-	-	-	-	-	-	-
1 week	3	3	3	3	3	3	3	3	3
2 weeks	3	3	3	-	-	-	-	-	-
1 month	3	3	3	-	-	-	-	-	-
24 hours at 250°C	3	-	-	-	-	-	-	-	-

Both room temperature and elevated temperature tests were performed in a Walter + Bai multipurpose Servo hydraulic universal testing machine Series LFV 100KN with a constant tool speed of 0.56mm/min. A XIMEA CB200MG-CM digital camera with a Canon EF 100mm f/2.8L Macro IS USM lens was used to capture images of the specimen during the test. The acquisition frequency was two images per second, with synchronized logging of force data registered by the tensile test machine. The image acquisition was always started before any force was applied. To ensure clear contrast between the specimen and the background, the specimen was painted white and light absorbing black paper was used as background. The paint used was Rust-oleum Hard hat, high performance top coat colour 2190, matt white.

Set up for room temperature tests

The specimen was placed in the grips of the tensile test machine, and the camera was placed as close to the specimen as possible, while keeping the entire gauge length in the image. One light source was placed on the left side of the camera, and one was placed on the right side. An image of the set up is shown in Figure 3.3.

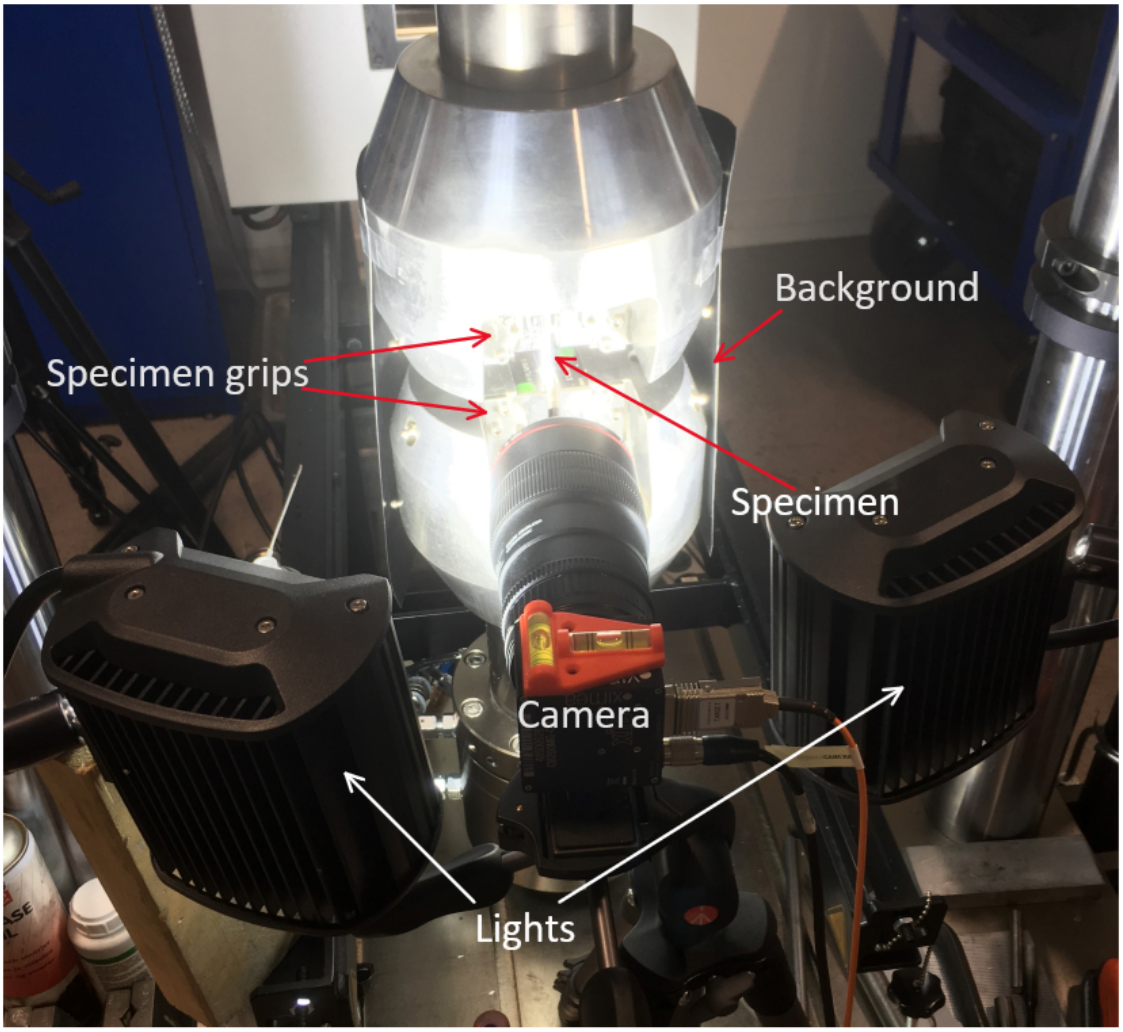

Figure 3.3: Set up for room temperature tensile tests

Set up for elevated temperature set

Tensile tests at elevated temperatures were performed in a heat chamber accessory to the tensile test machine. The chamber was heated for 2 hours before the 100°C tests and for 2.5 hours before the 150°C tests. This was to ensure sufficient heating of the steel grips which hold the specimen. The camera was placed outside the chamber window. An additional Kenko Teleplus PRO 300 DGX 2x AF Teleconverter lens was added to compensate for the increased distance between the camera and specimen. The lighting system consisted of two light inside the heat chamber and two Godox LEDM150 LED Smartphone Lights with light diffusing screens. Inside the chamber there was one light on each side of the specimen. The Godox lights were fastened to the chamber window with tape, one above and one below the camera. After gripping the specimen in the tensile test machine, it was heated for ten minutes before the test started. The setup for elevated temperature tensile tests is illustrated in Figure 3.4

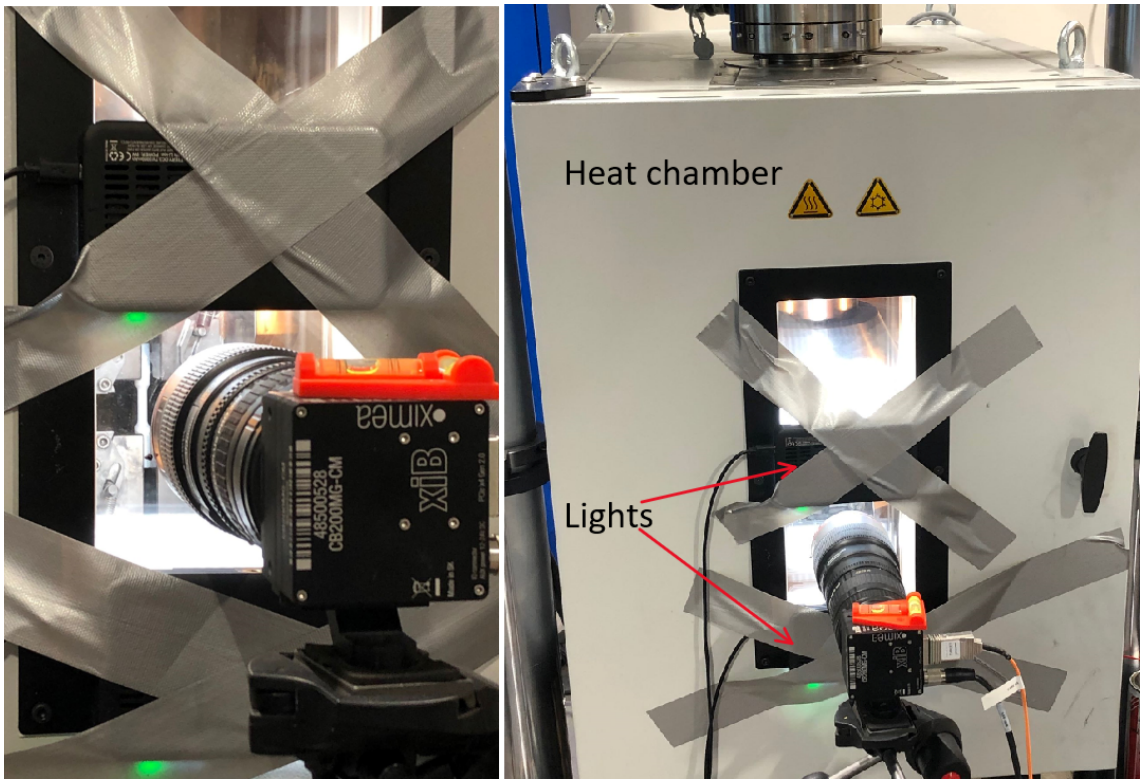

Figure 3.4: Set up for room elevated temperature tensile test

3.2 Commercial pure aluminium

Commercial pure aluminum with 0.15% silicon and 0.15% iron was tested as a reference. Specimens with geometry given in Figure 3.5 were machined from an as-cast aluminium block. The specimens were homogenized in a Nabertherm N17/HR oven for 6 hours at 550°C, with a heating rate of 100°C/hour, followed by air cooling.

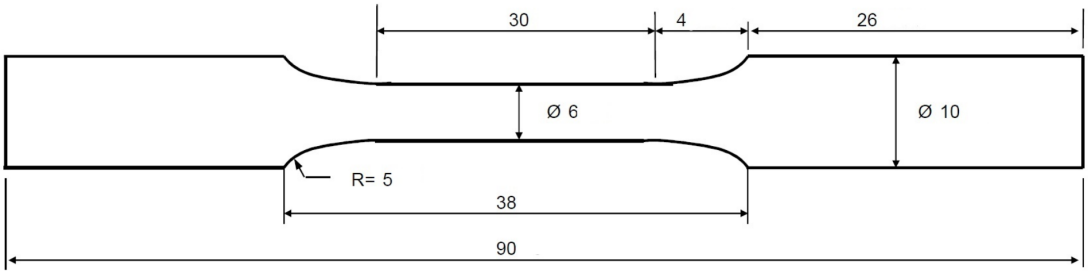

Figure 3.5: Geometry of pure aluminium specimens

Commercial pure aluminum tensile test were conducted with a similar setup as described in Section 3.1.3, but with the heat chamber turned off. To avoid unevenness on the specimen surface due to severe deformation before

fracture, the test was paused after a displacement of approximately 9 mm. This was known to be prior to necking from an earlier, failed test. The paint was removed by acetone and the specimen was polished with silicon carbide grinding paper. It was then repainted, and the test continued until fracture.

3.3 Analysis

3.3.1 Outline of Python script

The images acquired in the tensile tests were processed using a python script created by PhD candidate Feng Lu. In the script, the contour of the specimen is tracked and used to find the minimum diameter and radius of curvature in the neck. The minimum diameter is used for finding the strain and the minimum area. In this section, the outline of the program is described, as well as the further processing of the data.

The images were cropped to include only the necking region and short sections of the uniform length. This was done by manually specifying a pixel range. A typical width of the cropped image was 1500 pixels for the room temperature tests and 1000 pixels for the elevated temperature tests. After a cropping range was specified, the cropping was applied to ten preview images. Examples of three of the preview images for one of the specimens of alloy M, aging time 3 hours. tensile test at 100°C are shown in Figure 3.6. This figure has been cropped to exclude parts of the background.

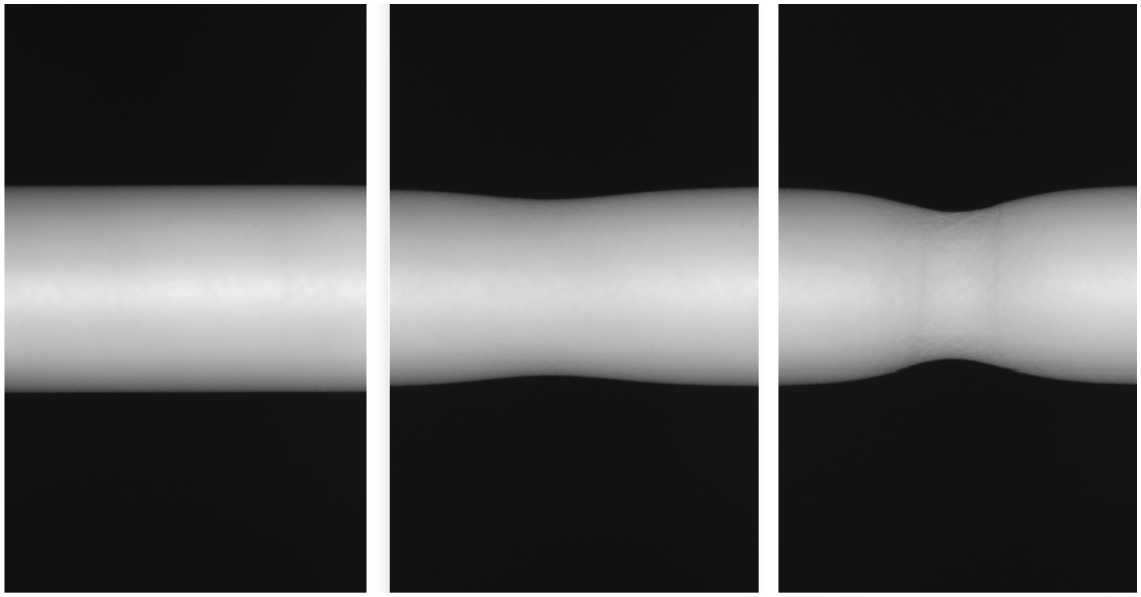

Figure 3.6: Three of the ten preview images

Based on the preview images, the interval could be adjusted until only the desired parts were included. The example in Figure 3.6 is well adjusted, for two main reasons:

- Every image from the onset of necking to the fracture point must include the necking region. As the specimen length increases, the position of the neck will not be the same in all the images. This can be seen in the second and third image in Figure 3.6.
- The third image is the point with associated with the highest registered force, and is according to Section 2.6.5 the last point with uniform deformation. The contours in this image is assumed to be two straight lines, and a rotation angle is found based on the slope of the lines. This angle is used to rotate all the images. If the specimen head is included in the cropped version of this image, this will affect the rotation angle. In addition to the preview images, the straight line approximation and rotation angle are given as output. An example of a bad fit due to a small section of the head to the left in the image is shown in Figure 3.7. The black points are the individual points of the tracked surface, and the blue line is the fitted line. It is clear that the blue line is not a good fit for the points on the gauge length.

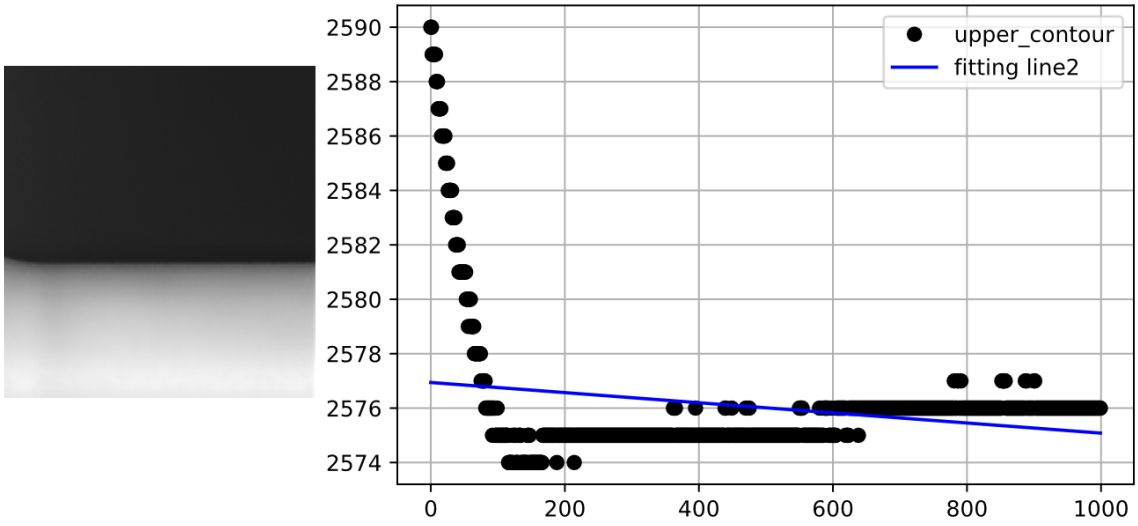

Figure 3.7: The consequence of the specimen head in the cropped image

After cropping, the grey scale distribution along each vertical line of the images were used to track the contour of the specimen. An example of a grey scale distribution is illustrated in Figure 3.8. The x-axis describes the vertical position of the image in pixels. The y-axis describes the scale of grey for the pixel on a scale from 0-255, where 0 is black and 255 is white.

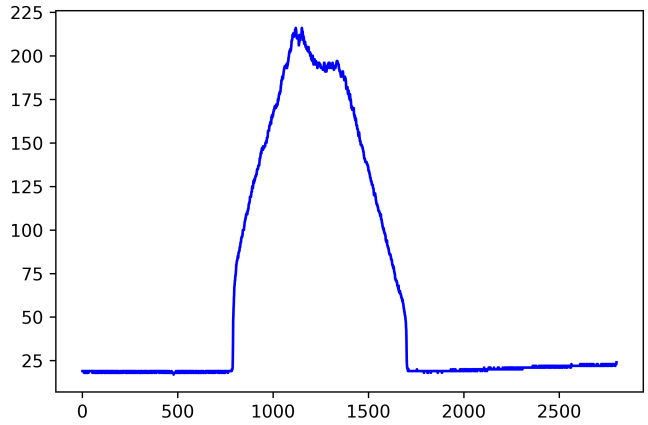

Figure 3.8: Grey scale distribution along a vertical line, used to track contour of specimen

Along each line, the point with the maximum brightness was found. The first estimate of the contour point was set at the point there the brightness value was 0.5 times the maximum brightness value.

The pixel length was found from the first image, which was taken before any force was applied. It was found from the number of pixels between the tracked contours and the diameter of the specimen, which was measured in advance. The rotation angle was, as mentioned, found from the image where the maximum force was registered, by approximating the contours as straight lines. The slopes were found by least square fitting, and the rotation angle was the angle between the fitted line and a horizontal line. An exaggerated illustration is shown in Figure 3.9.

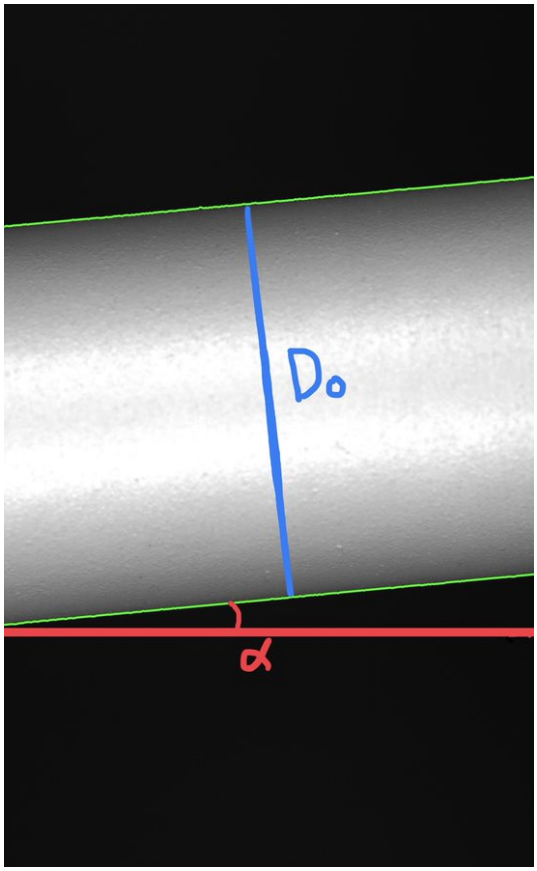

Figure 3.9: Misalignment angle α and initial diameter marked on the first image acquired in an experiment. Rotation angle is exaggerated for clarity in this illustration

The other images were rotated by the same angle α, and their contours were tracked using the grey scale distribution. The contour points were fitted to a Chebyshev polynomial of order 2 before necking and order up to 15 after necking. This was used to estimate the diameter of the minimum area of the specimen and the radius of curvature of the neck. The fitted curve for one image with the radius of curvature and the position of the minimum diameter marked, is illustrated in Figure 3.10.

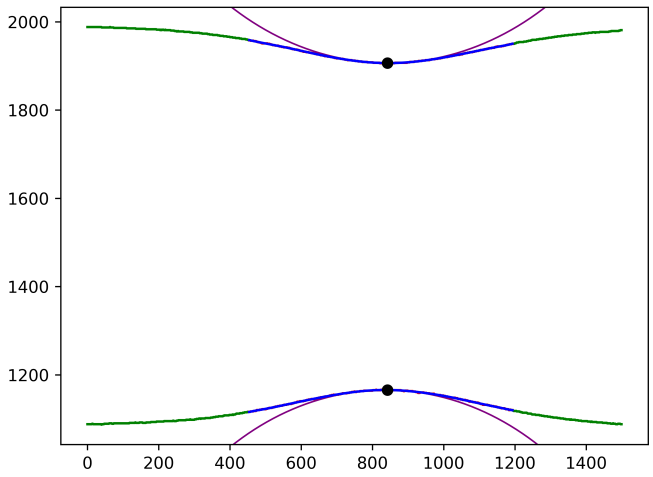

Figure 3.10: Polynomial fitted to specimen contour, with the radius of curvature. The minimum diameter is the distance between the two black dots.

For each image, the strain was found from the measured diameter with Equation 2.34. The force and minimum area were used to find the stress by applying Equation 2.1.

3.3.2 Correction of stress-strain curves

The onset point for necking was found by the maximum force. The point of fracture was determined from the uncorrected stress-strain curves, as the point where the stress dropped rapidly.

Measured $\delta = \frac{a}{R}$ from necking to fracture was smoothed by least square fitting to Equation 3.1.

$$\frac{a}{R} = k_1 \left(\epsilon - \epsilon_u\right) - k_2 \left(1 - exp\left(-\frac{k_1}{k_2}\left(\epsilon - \epsilon_u\right)\right)\right) \tag{3.1}$$

Equation 3.1 is an extension of Equation 2.46 presented by Leroy. It is the sum of an exponential term which dominates at low strains, and a linear part which dominates at high strains. One set of parameters was found for each alloy and aging time, based on both specimen contours of all the parallels. Additionally, finite element analysis of the development of $\frac{a}{R}$ was performed by postdoctoral fellow Tomás Mánik for alloy S, aging time 20 minutes and 3 hours at 180°C and 24 hours at 250°C.

After necking, the stress was corrected by the Gromada correction factor, presented in Equation 2.45. The smoothed $\frac{a}{R}$ was used as δ.

3.3.3 Strength and ductility measurement

The method for estimating the yield strength is illustrated in Figure 3.11. The plastic component of the strain, found using Equation 2.38 was plotted against the stress. If the zero-strain point was shifted, a vertical line was positioned by eye in the center of the noise of the elastic part. This is the red line illustrated in Figure 3.11. Another vertical line with a plastic strain of 0.002 higher than the red line was added. This is the green line shown in Figure 3.11. The intersection between this line and the plastic strain-stress curve was chosen as the yield strength.

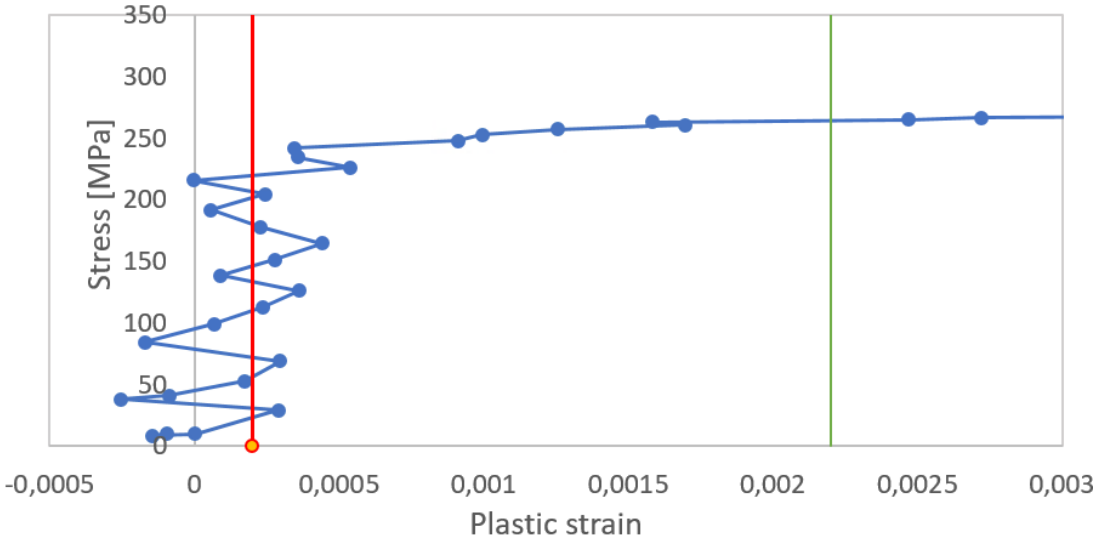

Figure 3.11: Method used for estimation of the yield strength.

Determining the position of the lines can be challenging due to noise in the elastic region. The potential error in reading of the values was determined by Equation 3.2

$$\Delta\sigma_y = \Delta\epsilon_{zz}^{pl} \frac{d\sigma}{d\epsilon_{zz}^{pl}} \tag{3.2}$$

where $\Delta\epsilon_{zz}^{pl}$ is the difference between the largest and smallest plastic strain in the elastic region and $\frac{d\sigma}{d\epsilon_{zz}^{pl}}$ is the slope of the stress- plastic strain curve around the yield point.

True uniform strength was calculated by Equation 2.42. Area reduction at fracture was found from the original diameter and the diameter from the fracture point, with Equation 2.47

3.3.4 Work hardening rates

Work hardening rates, θ, were determined from the derivative of the corrected stress-strain curves. Determining the derivative required smoothing of the stress-strain curves. This was done by using a Python script developed

by PhD candidate Feng Lu with the following procedure. The stress and strain were smoothed separately by using a median filter with window size 5. This means that every point is replaced with the median value for the five points around it. Next, the stress and the strain were fitted to Chebyshev polynomials of order 15, before a second median filter with window size 5 was applied. The smooth stress and strain were recombined to a stress-strain curve, where the derivative was found using Equation 3.3

$$\theta_i = \frac{\sigma_i - \sigma_{i-1}}{\epsilon_i - \epsilon_{i-1}} \tag{3.3}$$

θ_{max} and $\frac{d\theta}{d\sigma}$ were found by the procedure suggested by Cheng *et al.* [28], illustrated in Figure 2.22.

4 Results

In this section, the results from the tensile tests are presented. First, a selection of the stress-strain curves are presented. All stress-strain curves are attached in Appendix A. Unless otherwise specified, aging time refers to aging time at 180°C. Then follows some important values extracted from the stress-strain curves, the yield strength, the true uniform strain, area reduction at fracture and the slope in stage IV of work hardening. The most overaged condtition, alloy S aged for 24 hours at 250°C, has been excluded in the figures in this part of the results due to the aging temperature being different. However, all values can be found in tables at the end of each subsection.

From the work hardening results, a selection of the Kocks-Mecking curves are presented. All curves are attached in Appendix B. The parameters describing the Kocks-Mecking curves, $-\frac{d\theta}{d\sigma}$ and θ_{max} values are also presented.

All the results for pure aluminium is presented in section 4.9

4.1 Stress-strain curves

In this section a selection of the stress-strain curves are presented. The trends in the results presented are representative for the trends in the results excluded from this section. All stress-strain curves are presented in Appendix A.

4.1.1 Temperature dependency

The stress-strain curves for tensile test at room temperature, 100°C and 150°C are presented for aging times 3 hours and 1 week are for all alloys in Figures 4.1 - 4.6. The results show that the increase in temperature is always associated with a strength loss. For some of the results, the ductility increase with temperature.

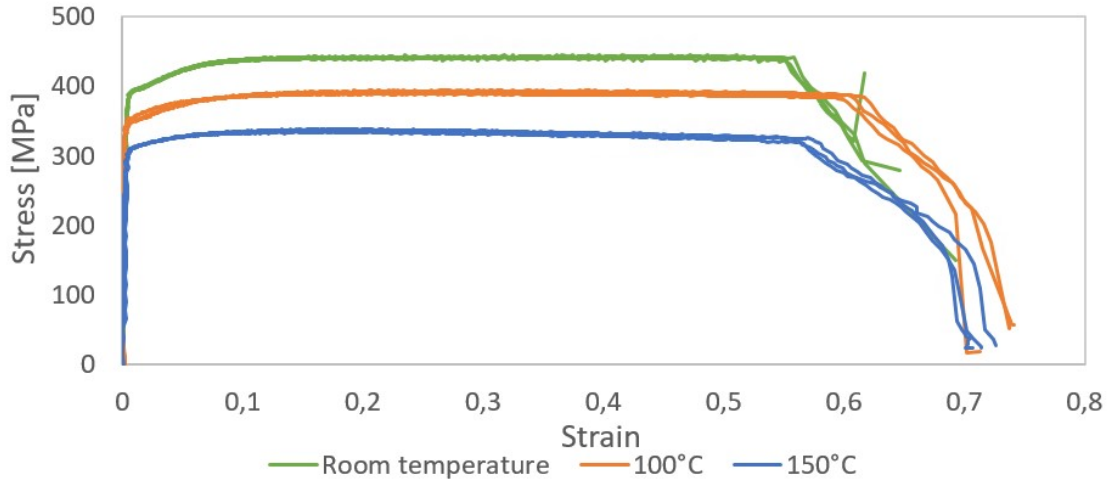

Figure 4.1: Stress-strain curve for alloy S, aging time 3 hour

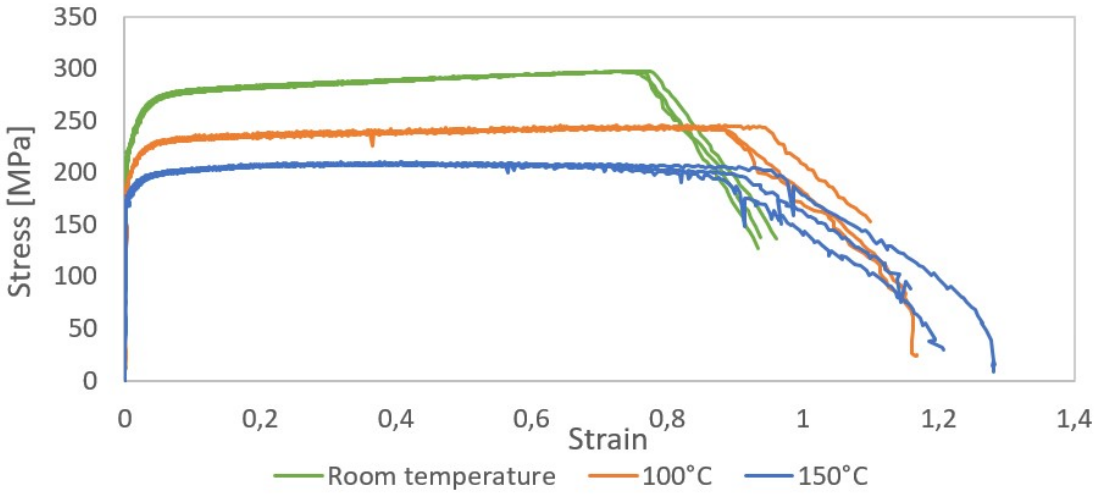

Figure 4.2: Stress-strain curve for alloy S, aging time 1 week

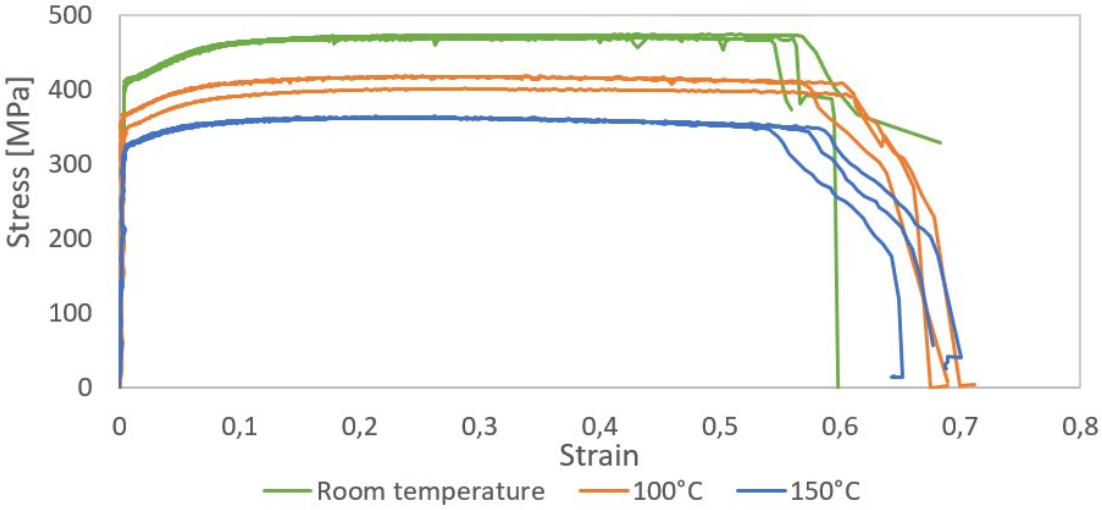

Figure 4.3: Stress-strain curve for alloy C, aging time 3 hour

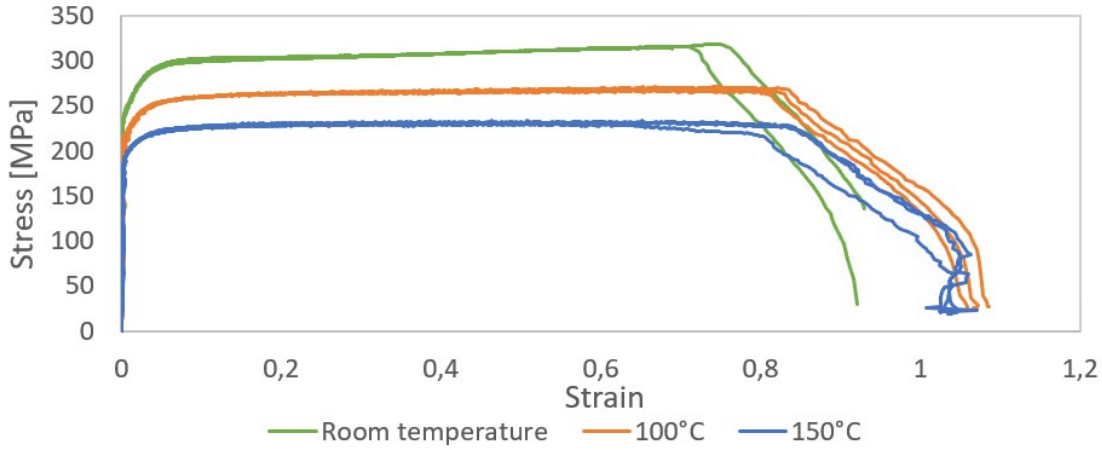

Figure 4.4: Stress-strain curve for alloy C, aging time 1 week

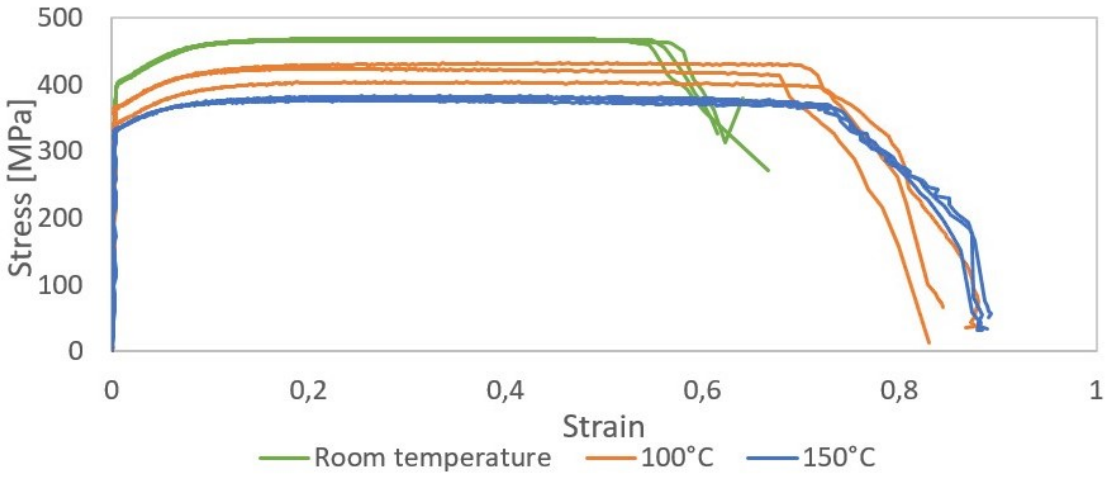

Figure 4.5: Stress-strain curve for alloy S, aging time 3 hour

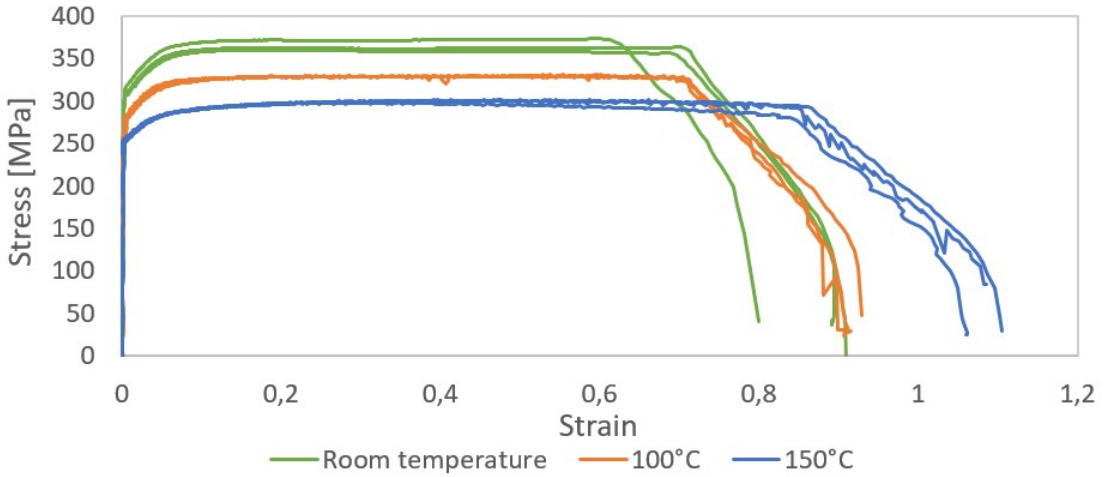

Figure 4.6: Stress-strain curve for alloy M, aging time 1 week

4.1.2 Aging time dependency at room temperature

In this section, one parallel from each aging time at room temperature is presented for alloy S in Figure 4.7, alloy C in Figure 4.8 and alloy M in Figure 4.9. A zoom window has been added due to small variations between the strongest curves.

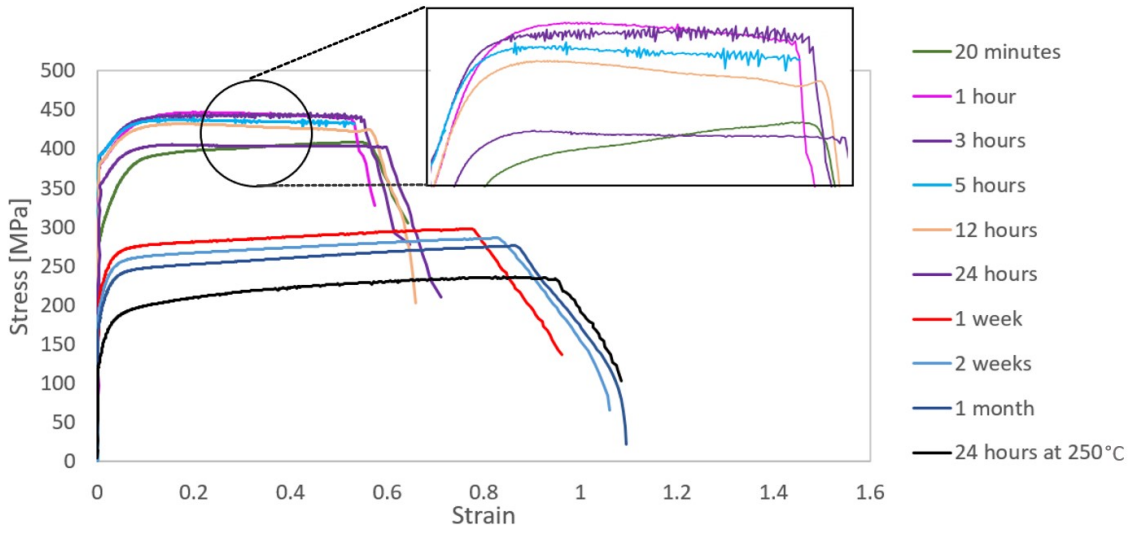

Figure 4.7: Stress-strain curves for tensile tests at room temperature for all aging conditions for alloy S

The results in Figure 4.7 show that alloy S is strongest after aging times 1 hour and 3 hours. Longer aging times give decreasing strength.

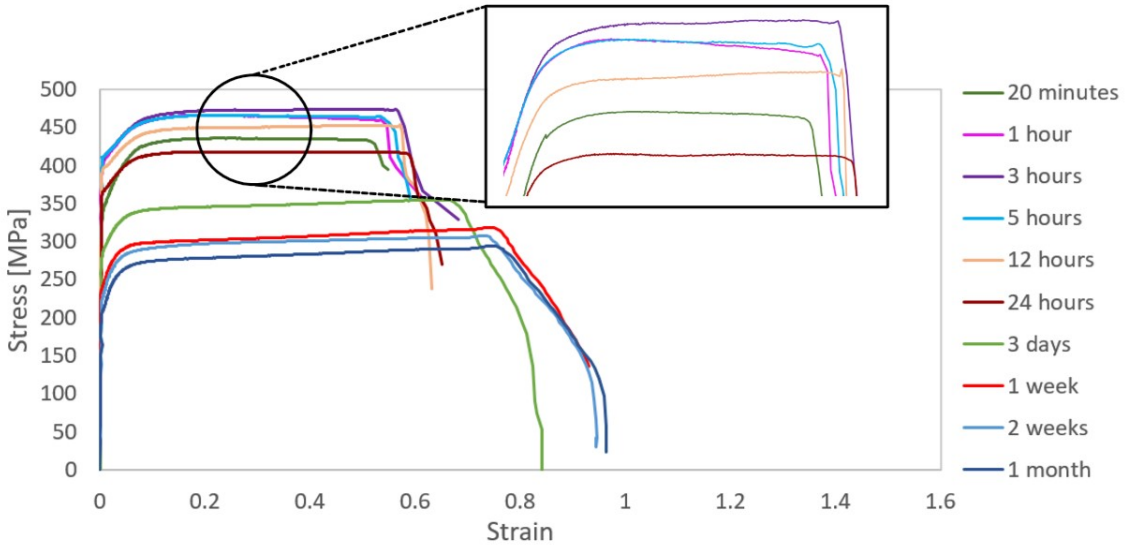

Figure 4.8: Stress-strain curves for tensile tests at room temperature for all aging conditions for alloy C

The results in Figure 4.8 show that alloy C is strongest for aging time 3 hours. Longer and shorter aging times give decreasing strength.

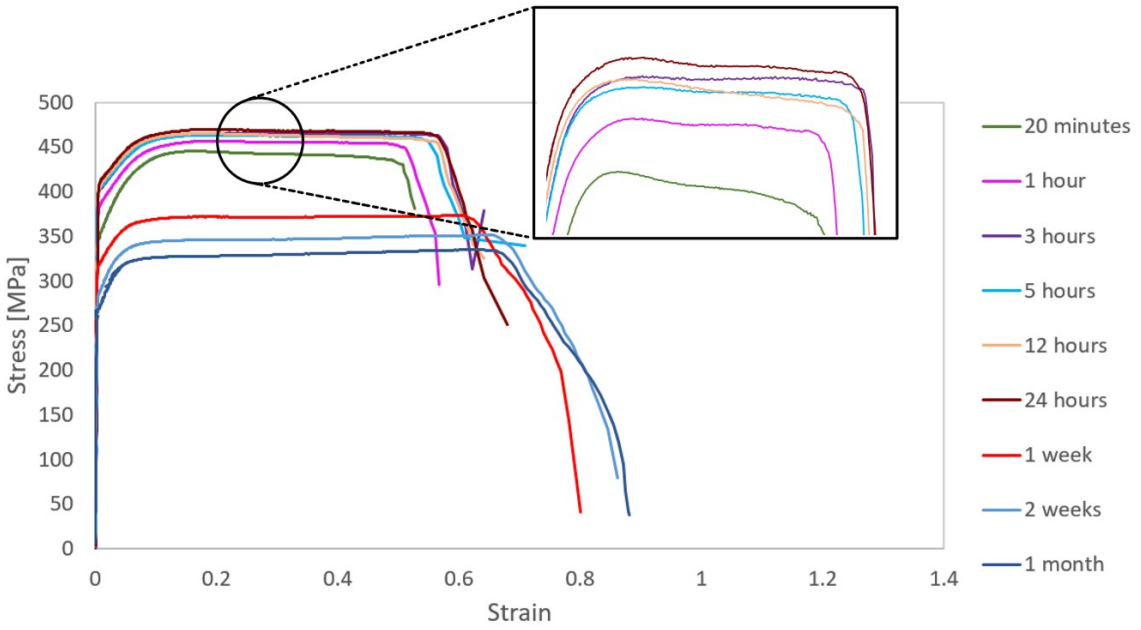

Figure 4.9: Stress-strain curves for tensile tests at room temperature for all aging conditions for alloy M

The results in Figure 4.9 show that alloy M is strongest after 24 hours, followed closely by aging times 3 - 12 hours. Longer and shorter aging times give decreasing strength.

4.1.3 Aging time dependency at 100°C

The stress-strain curves for all the parallels for alloy S, C and M at tensile test temperature 100°C are presented in Figures 4.10 - 4.12.

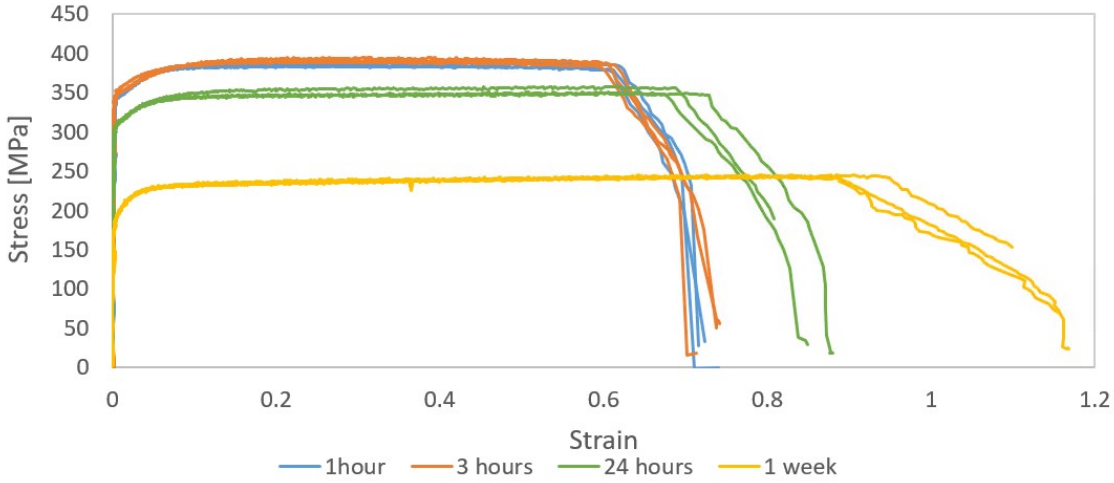

Figure 4.10: Stress-strain curves for tensile tests at 100°C for all aging conditions for alloy S

Figure 4.10 shows that the stress-strain curves for aging times 1 hour and 3 hours are overlapping for alloy S. For aging times 24 hours and 1 week the strength is decreased and the ductility is increased.

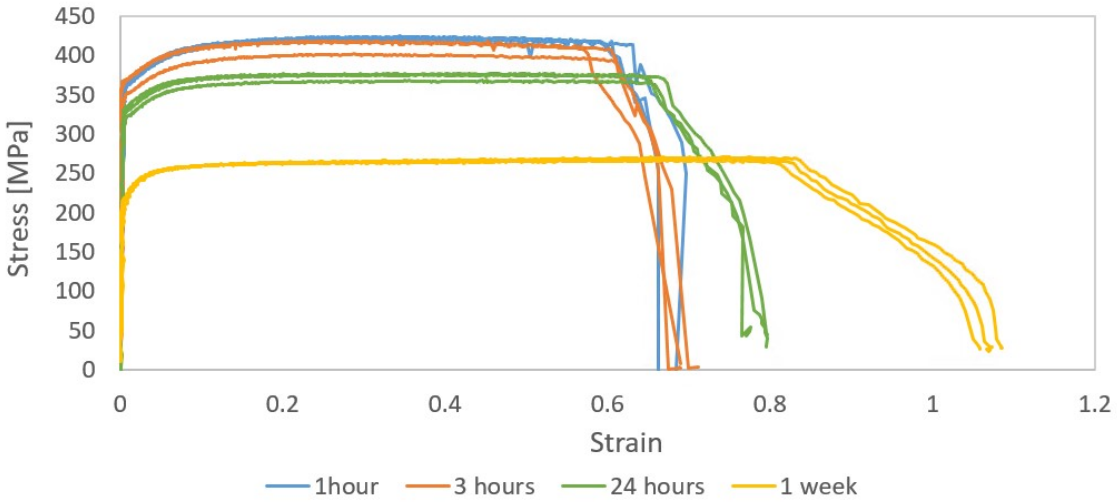

Figure 4.11: Stress-strains for all aging conditions for alloy C, 100°C

Figure 4.11 shows that alloy C behaves similarly as alloy S at 100°C. Aging times 1 hour and 3 hours are overlapping, and aging times 24 hours and 1 week are weaker and more ductile.

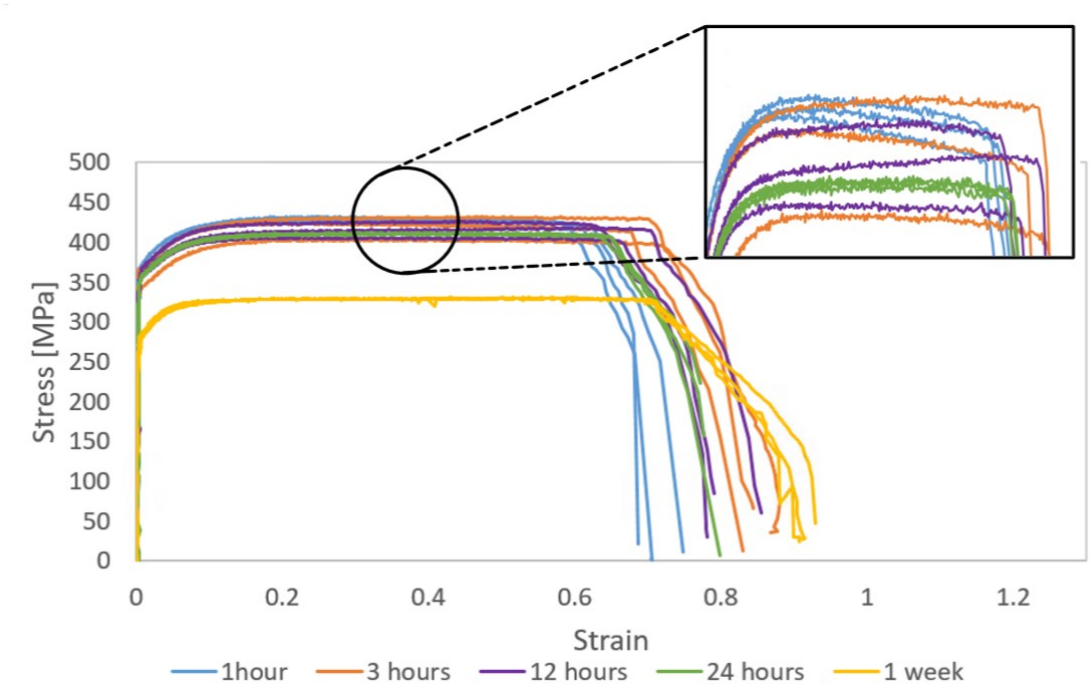

Figure 4.12: Stress-strains for all aging conditions for alloy M, 100°C

Figure 4.12 shows that for alloy M, the stress-strain curves at 100°C are close to overlapping for aging times 1 hour - 24 hours. The zoom window shows a larger spread of the parallels for the 3 hours and 12 hours results. Aging time 1 week is weaker, but not noticeably more ductile.

4.1.4 Aging time dependency at 150°C

The stress-strain curves for all the parallels for alloy S, C and M at tensile test temperature 150°C are presented in Figures 4.13 - 4.15.

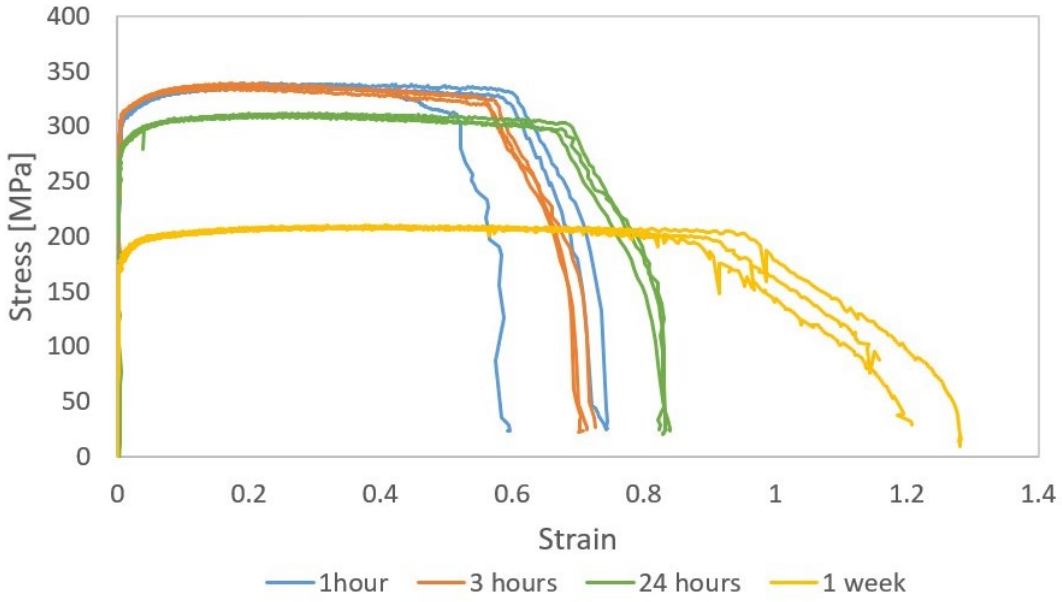

Figure 4.13: Stress-strains for all aging conditions for alloy S, 150°C

The results in Figure 4.13 show that the stress-strain curves for aging time 1 hour and 3 hours are overlapping for alloy S at 150°C, and that aging times 24 hours and 1 week are weaker and more ductile. One of the parallels at aging time 1 hour shows much lower ductility than the other two.

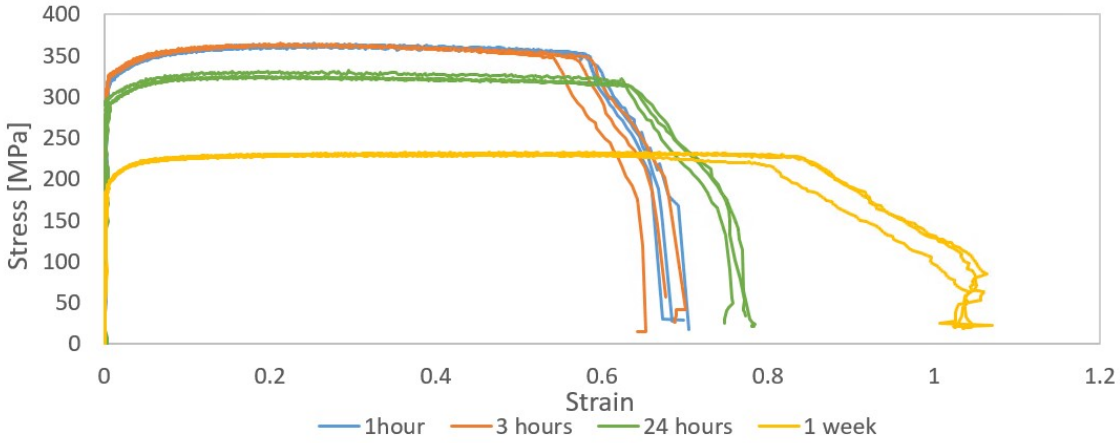

Figure 4.14: Stress-strains for all aging conditions for alloy C, 150°C

Figure 4.14 show that for alloy C at tensile test temperature 150°C, the stress-strain curves for aging times 1 hour and 3 hours are overlapping. Aging times 24 hours and 1 week are weaker and more ductile.

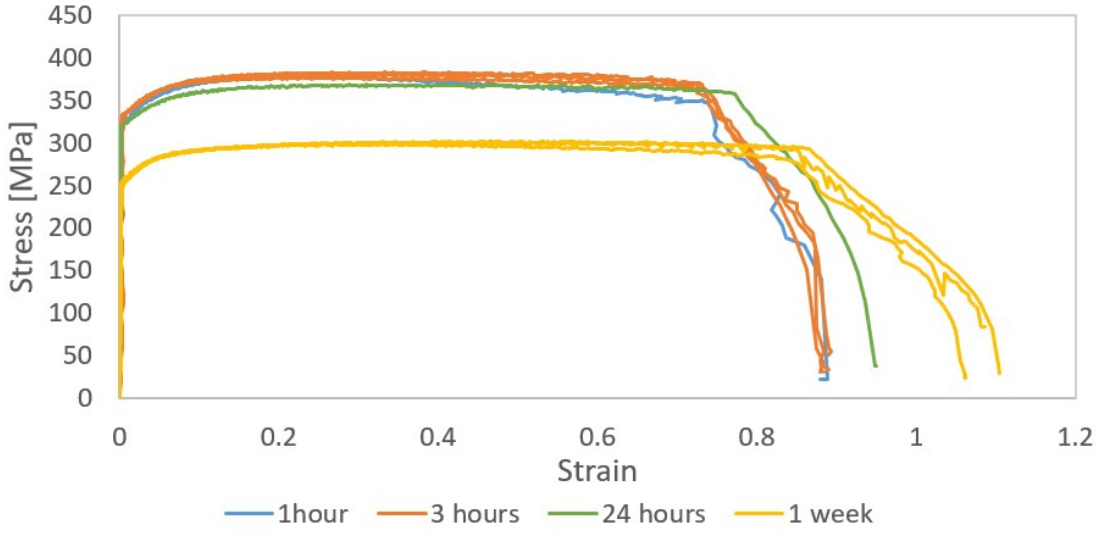

Figure 4.15: Stress-strains for all aging conditions for alloy M, 150°C

The results for tensile test of alloy M at150°C show that aging times 1 hour to 24 hours has similar strength. Aging time 1 week is weaker and more ductile.

4.2 Yield strength

The development of yield strength for the three alloys with aging time is given in Figures 4.16, 4.17 and 4.18 for tensile tests at room temperature, 100°C and 150°C respectively. The values are determined by the method

illustrated in Figure 3.11. The yield strength of each test is marked with a point, while the solid lines drawn between mark the average values for the parallels. All values, including $\Delta\sigma_y$ is given in Table 4.1

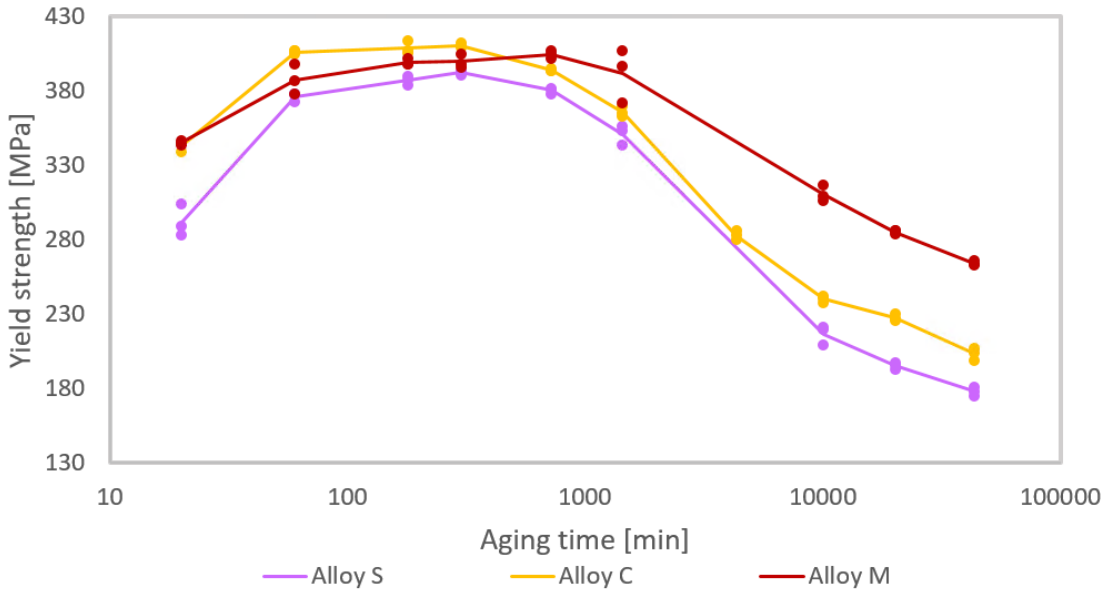

Figure 4.16: Yield strength for alloy S, C and M at room temperature

The results in Figure 4.16 show that around the peak yield strength the three alloys have a similar strength. The aging times for peak strength is 5 hours for alloy S and alloy C and 12 hours for alloy M. Around the peak strength there is a plateau where the reduction in yield strength is less than 5%. This plateau is for aging times from 1 to 12 hours for alloy S and alloy C and from 1 to 24 hours for alloy M. After the plateau, there is a yield strength loss for all three alloys. The yield strength loss from peak strength to strength after one month aging is 55% for alloy S, 50% for alloy C and 35% for alloy M.

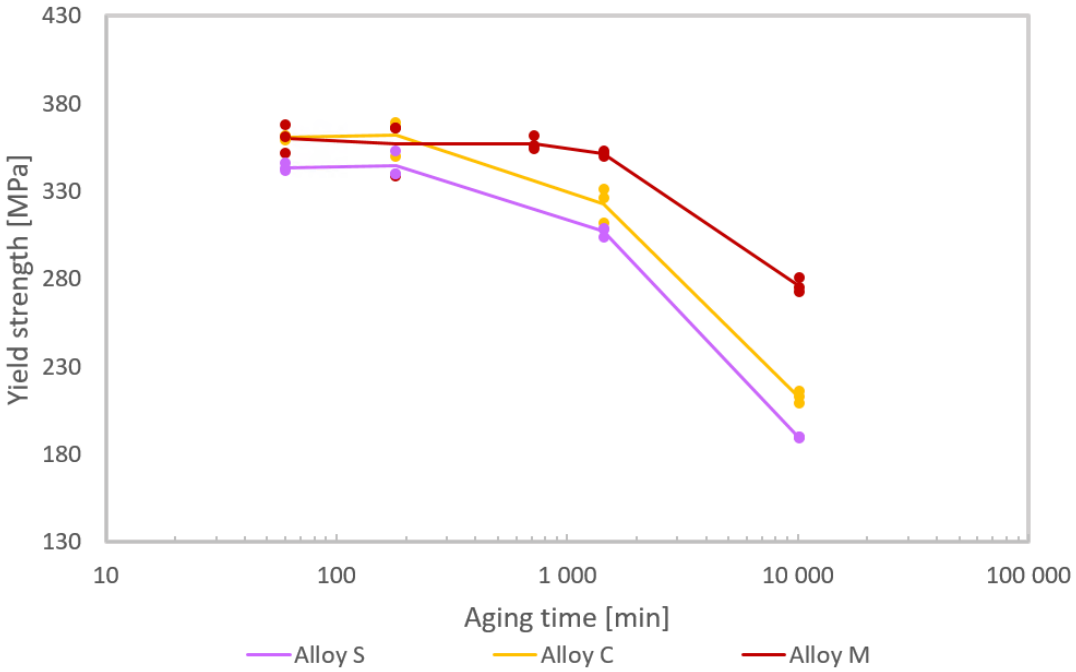

Figure 4.17: Yield strength for alloy S, C and M at 100°C

The results in Figure 4.17 show that alloy C and M has approximately the same strength for aging times 1 hour and 3 hours at 100°C. For longer aging times, alloy M is the strongest. for all aging times except 3 hours, The development with aging time for alloy S and alloy C follow the same trend, where alloy C consistently is approximately 20 MPa stronger than alloy S. The development for alloy M is different, where the yield stress is approximately constant up to aging time 24 hours.

The results for 150°C in Figure 4.18 show a similar behaviour as for 100°C. For the 150°C tests, alloy M is strongest and alloy S is the weakest for all aging times.

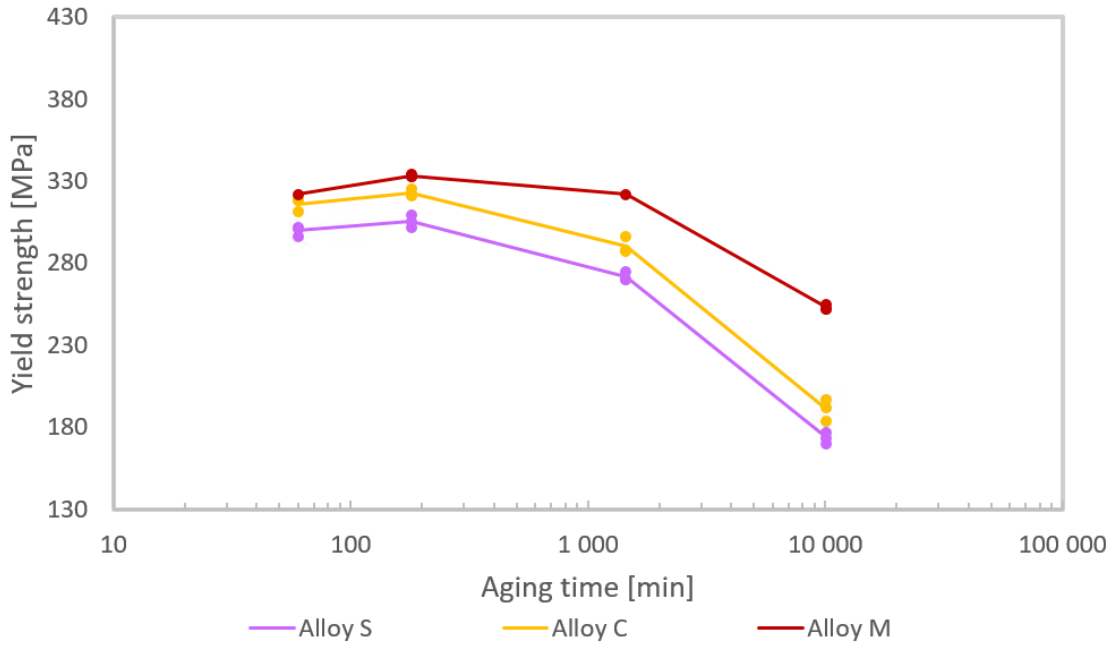

Figure 4.18: Yield strength for alloy S, C and M at 150°C

The yield strength for each alloy at the three different temperatures is given in Figure 4.19 for alloy S, Figure 4.20 for alloy C and Figure 4.21 for alloy M.

The results in Figure 4.19 - 4.21 shows that the strength decreases with increasing temperature. A temperature increase from room temperature to 100°C caused the yield strength to decrease with 11% for all the alloys for aging time 3 hours, and a temperature increase from room temperature to 150°C caused a decrease of 27% for alloy S, 21% for alloy C and 17% for alloy M.

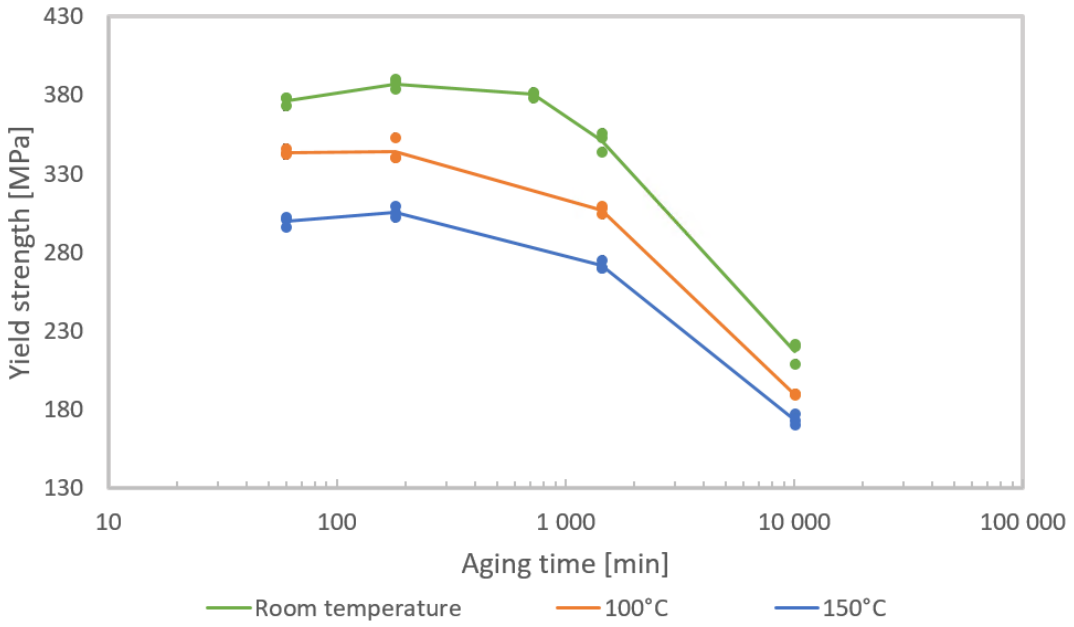

Figure 4.19: Yield strength for alloy S at room temperature, 100°C and 150°C

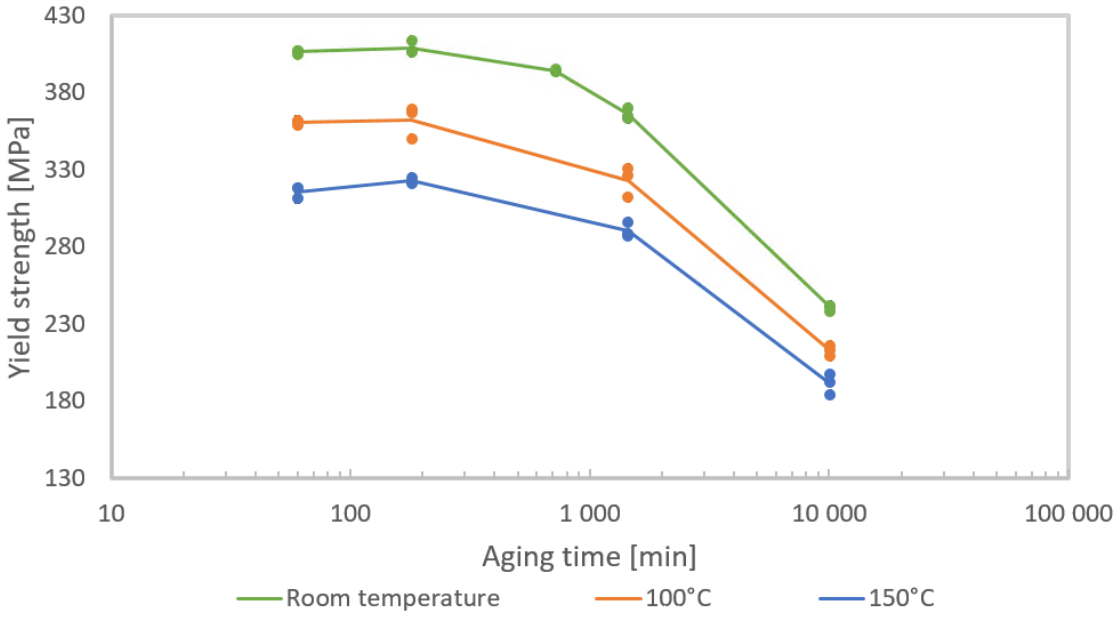

Figure 4.20: Yield strength for alloy C at room temperature, 100°C and 150°C

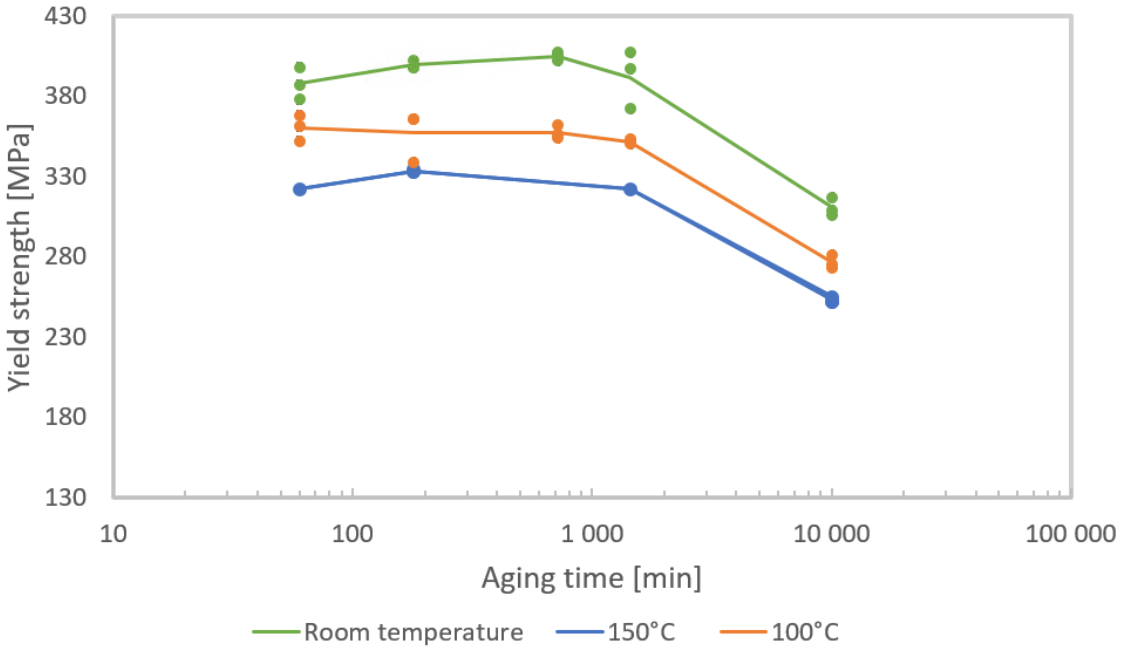

Figure 4.21: Yield strength for alloy M at room temperature, 100°C and 150°C

Table 4.1: Yield strength in MPa. $\Delta\sigma_y$ in parentheses

Aging time	Room temperature			100°C			150°C		
	S	C	M	S	C	M	S	C	M
20 minutes	283 (3) 289 (10) 304 (7)	339 (6) 345 (4) 345 (4)	345 (7) 344 (2) 347 (4)	-	-	-	-	-	-
1 hour	373 (23) 378 (5) 378 (5)	405 (1) 407 (4) 407 (1)	398 (6) 387 (4) 378 (3)	343 (9) 346 (2) 352 (3)	361 (6) 362 (3) 359(13)	361 (6) 368 (5) 352 (10)	301 (7) 302 (6) 296 (13)	318 (4) 311 (7) 318 (12)	322 (4)
3 hours	390 (7) 384 (5) 388 (2)	414 (1) 406 (3) 407 (2)	398 (3) 398 (3) 402 (3)	340 (12) 353(2) 340 (13)	367 (2) 369 (9) 350(13)	366 (4) 339 (4) 366 (6)	305 (7) 302 (18) 309 (6)	325 (10) 322 (8) 321 (6)	333 (9) 334 (10) 333 (3)
5 hours	391 (4) 392 (1) 394 (2)	412 (1) 409 (9) 410 (4)	398 (5) 398 (1) 410 (2)	-	-	-	-	-	-
12 hours	382 (3) 381 (2) 378 (5)	394 (2) 394 (3) 395 (3)	407 (5) 405 (3) 402 (3)	-	-	362 (8) 356 (7) 354 (5)	-	-	-
24 hours	353 (5) 356 (5) 344 (9)	365 (6) 363 (3) 370 (5)	407 (3) 372(11) 397 (2)	308 (3) 309 (4) 304 (5)	312 (20) 326 (4) 331 (5)	353 (6) 352 (10) 350 (10)	270 (9) 270 (23) 275 (10)	288 (8) 287 (19) 296 (5)	322 (2)
3 days	-	283 (8) 280 (16) 286 (6)	-	-	-	-	-	-	-
1 week	209 (7) 221 (3) 220 (3)	242 (6) 238 (2) 241 (2)	317 (4) 309 (2) 306 (3)	190 (3) 190 (10) 189 (10)	216 (6) 209(10) 213 (7)	275 (4) 273(10) 281 (5)	177 (3) 173 (4) 170 (4)	197 (8) 192 (6) 184 (9)	255 (6) 252 (2) 252 (4)
2 weeks	196 (3) 197 (4) 193 (3)	227 (4) 226 (2) 230 (10)	284 (4) 286 (8) 286 (2)	-	-	-	-	-	-
1 month	178 (3) 181 (2) 175 (3)	204 (9) 207 (7) 199 (15)	266 (7) 264 (4) 263 (5)	-	-	-	-	-	-
24 hours at 250°C	124 (4) 124 (3) 123 (6)	-	-	-	-	-	-	-	-

4.3 True uniform strength

The development of true uniform strength for the three alloys with aging time is given in figures 4.16, 4.17 and 4.18 for tensile tests at room temperature, 100°C and 150°C respectively. The true uniform strength of each test is marked with a point, while the solid lines drawn between are the average values for the parallels. All values are given in Table 4.2.

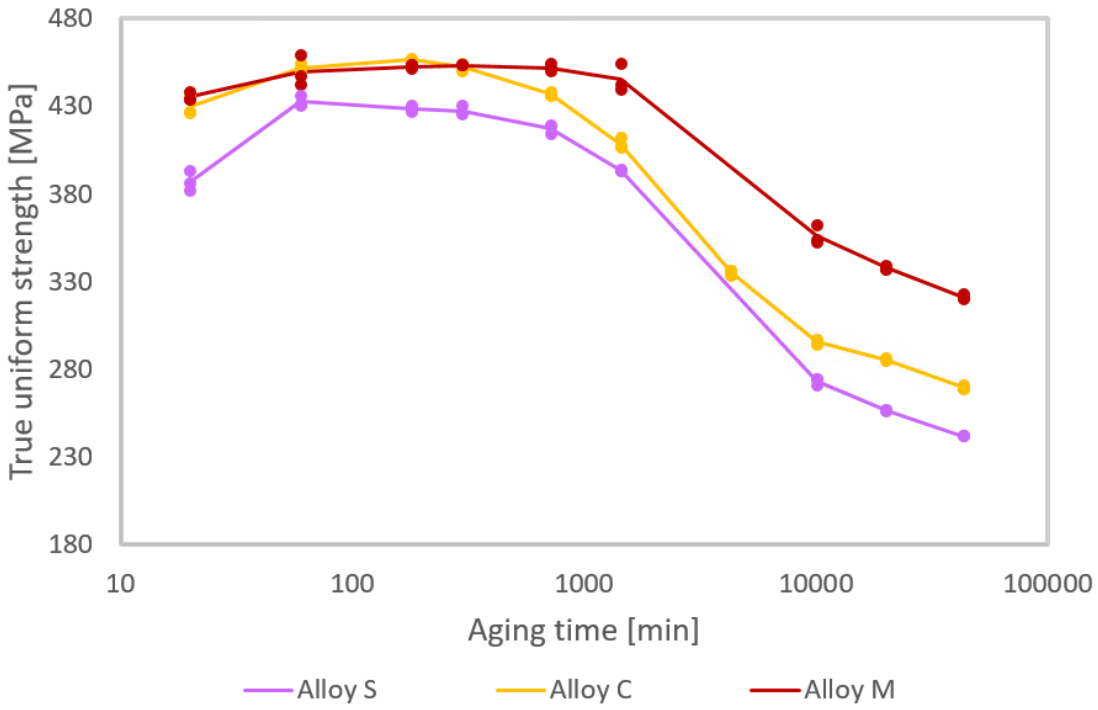

Figure 4.22: True uniform strength for alloy S, C and M at room temperature

As shown in Figure 4.22, the strength of alloy C and alloy M are similar for aging times up to 12 hours. Alloy M is the strongest for longer aging times. Alloy S is the weakest for all aging times. The aging time for peak true uniform strength is 1 hour for alloy S, 3 hours for alloy C and 5 hours or alloy M, but as for yield strength, these peaks are part of a plateau. The aging times included in the plateau where the average strength loss is less than 5% compared to the max average value are 1 to 24 hours for alloy S and alloy C, and 20 minutes to 24 hours for alloy M. The true uniform strength plateau is broader than for the yield strength for all the alloys. The true uniform strength loss from peak to 1 month is 44% for alloy S, 41% for alloy C and 29% for alloy M. The loss is lower than the yield strength loss for all the alloys.

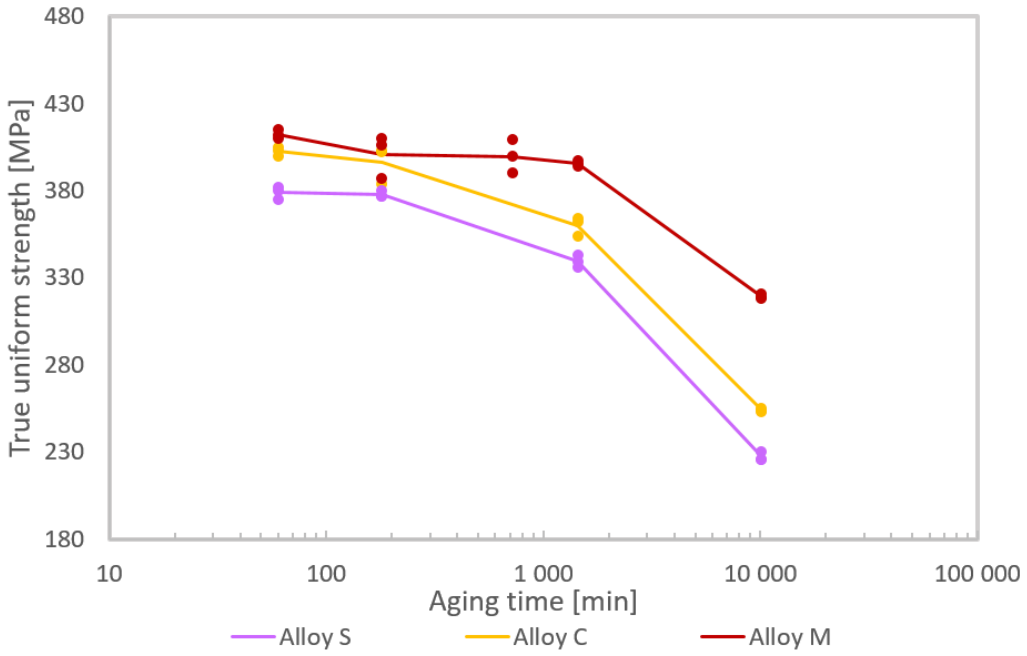

Figure 4.23: True uniform strength for alloy S, C and M at 100°C

Figures 4.23 and 4.24 show that alloy C and M has a similar strenght for aging times 1 hour and 3 hours, and that alloy M is stronger for longer aging times. At 150°C, alloy M is the strongest for all aging times. Alloy S is the weakest for all aging times for both 100°C and 150 °C. The true uniform strength development for alloy S and C is similar.

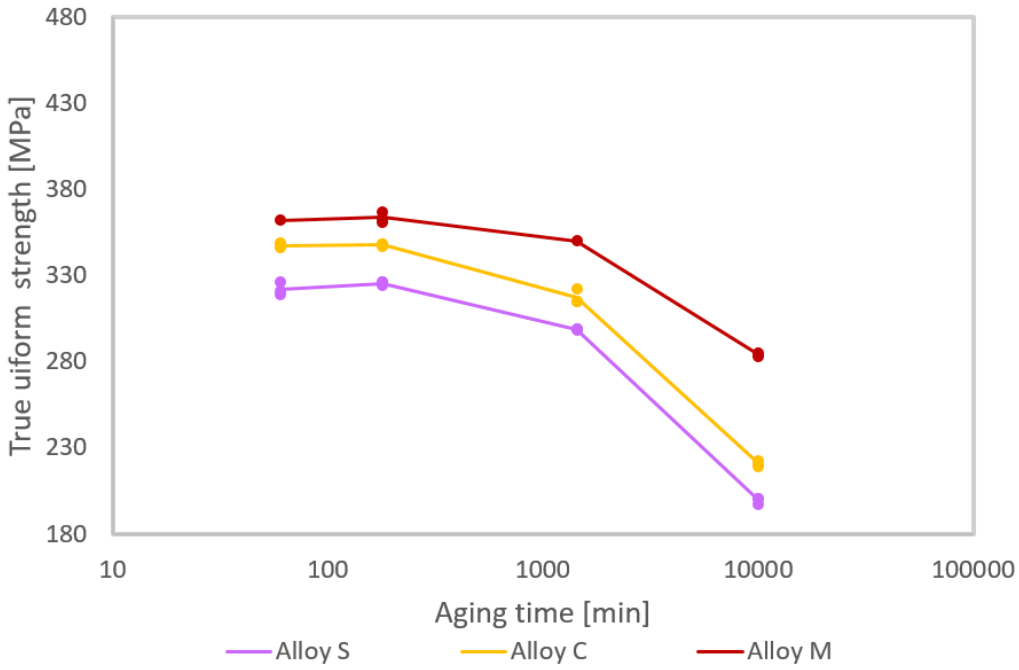

Figure 4.24: True uniform strength for alloy S, C and M at 150°C

The true uniform strength for each alloy at the three different temperatures is given in Figure 4.25 for alloy S, Figure 4.26 for alloy C and Figure 4.27 for alloy M. The strength is decreases with increased temperature. For temperature increase from room temperature to 100°C the strength loss is 12% for alloy S, 13% for alloy C and 11% for alloy M for aging time 3 hours. For a temperature increase from room temperature to 150°C the strength loss is 24% for both alloy S and alloy C and 20% for alloy M.

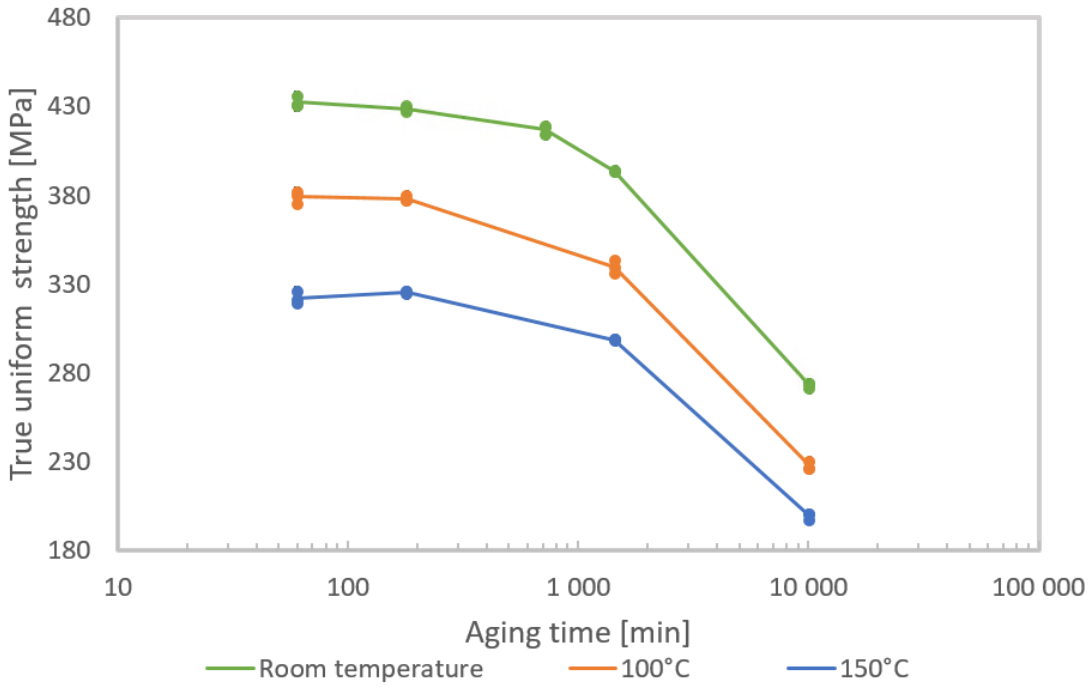

Figure 4.25: True uniform strength for alloy S at room temperature, 100°C and 150°C

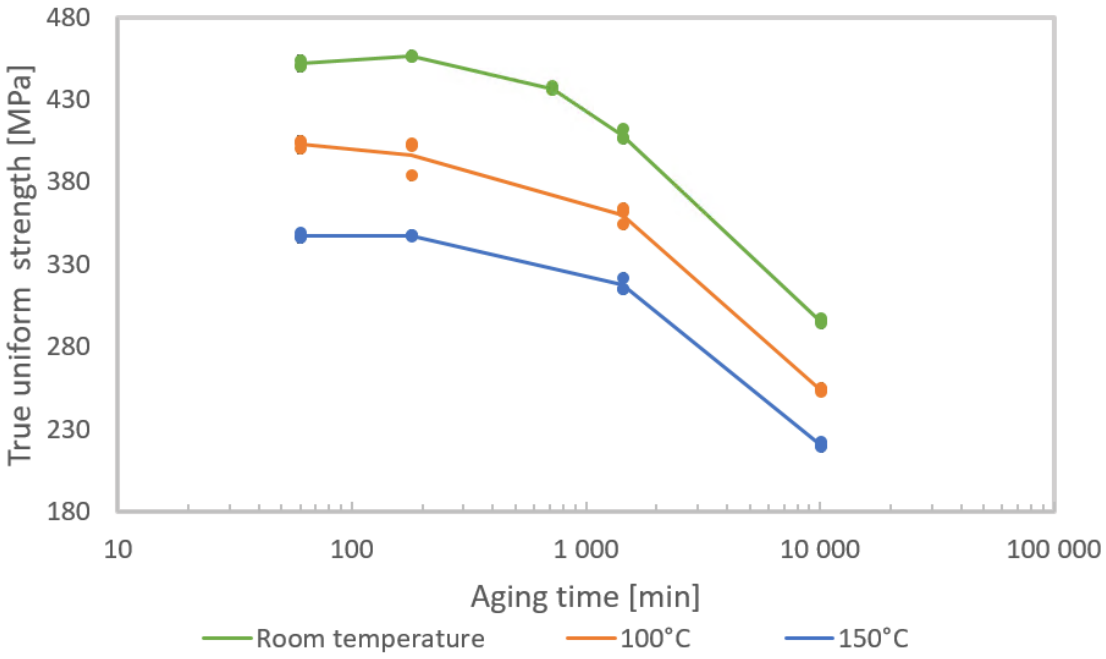

Figure 4.26: True uniform strength for alloy C at room temperature, 100°C and 150°C

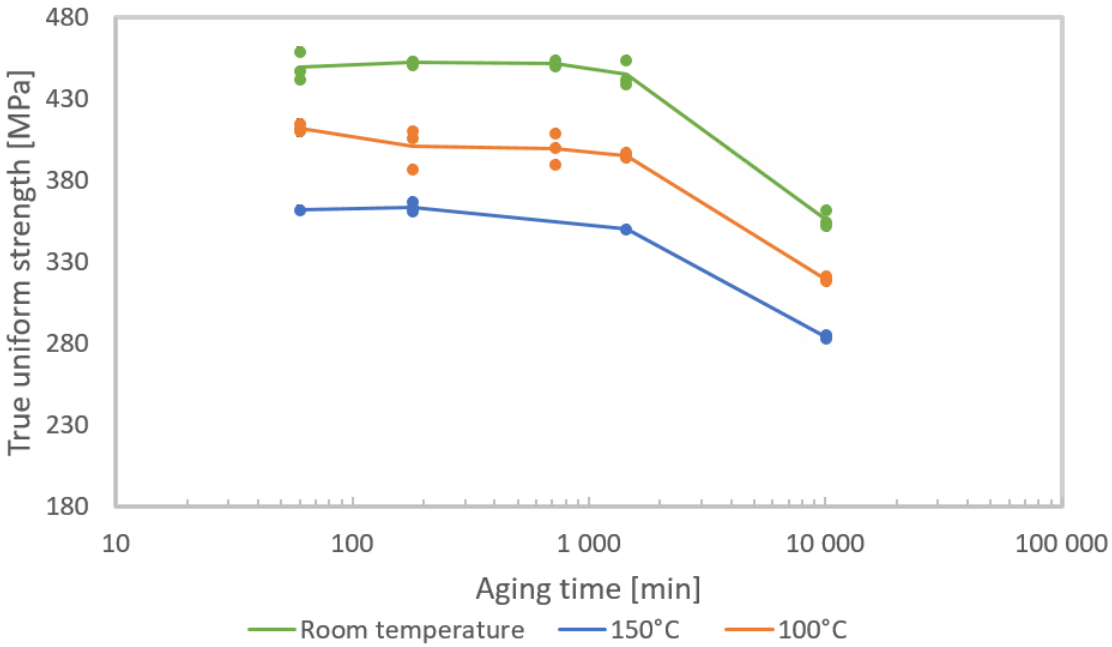

Figure 4.27: True uniform strength for alloy M at room temperature, 100°C and 150°C

Table 4.2: True uniform strength in MPa

Aging time	Room temperature			100°C			150°C		
	S	C	M	S	C	M	S	C	M
20 minutes	386 382 393	426 427 436	434 434 438	-	-	-	-	-	-
1 hour	436 431 430	451 450 454	459 447 442	380 382 375	405 403 400	415 410 412	321 326 319	346 347 349	362
3 hours	430 429 427	456 457 456	451 453 453	380 377 377	402 403 384	406 387 410	326 324 326	348 348 347	367 361 363
5 hours	426 425 430	450 454 452	453 453 453	-	-	-	-	-	-
12 hours	418 419 414	436 436 438	451 450 454	-	-	409 400 390	-	-	-
24 hours	393 393 394	407 406 412	454 442 439	343 336 339	354 362 364	397 395 394	298 299 299	315 315 322	350
3 days	-	336 333 336	-	-	-	-	-	-	-
1 week	271 274 274	297 294 296	362 354 352	226 230 226	255 253 254	321 319 318	200 200 197	219 220 222	285 284 283
2 weeks	257 257 256	285 285 286	337 339 337	-	-	-	-	-	-
1 month	242 242 242	269 269 271	320 323 321	-	-	-	-	-	-
24 hours at 250°C	196 194 194	-	-	-	-	-	-	-	-

4.4 Area reduction at fracture

The development of the ductility, measured as the area reduction at fracture is given for tensile tests at room temperature in Figure 4.28, at 100°C in Figure 4.29 and at 150°C in Figure 4.30. The area reduction for each test is marked with a point, while the solid lines drawn between are the average values for the parallels. All the values are given in Table 4.3. For some specimens the data acquisition was stopped prematurely, and the fracture point is unknown.

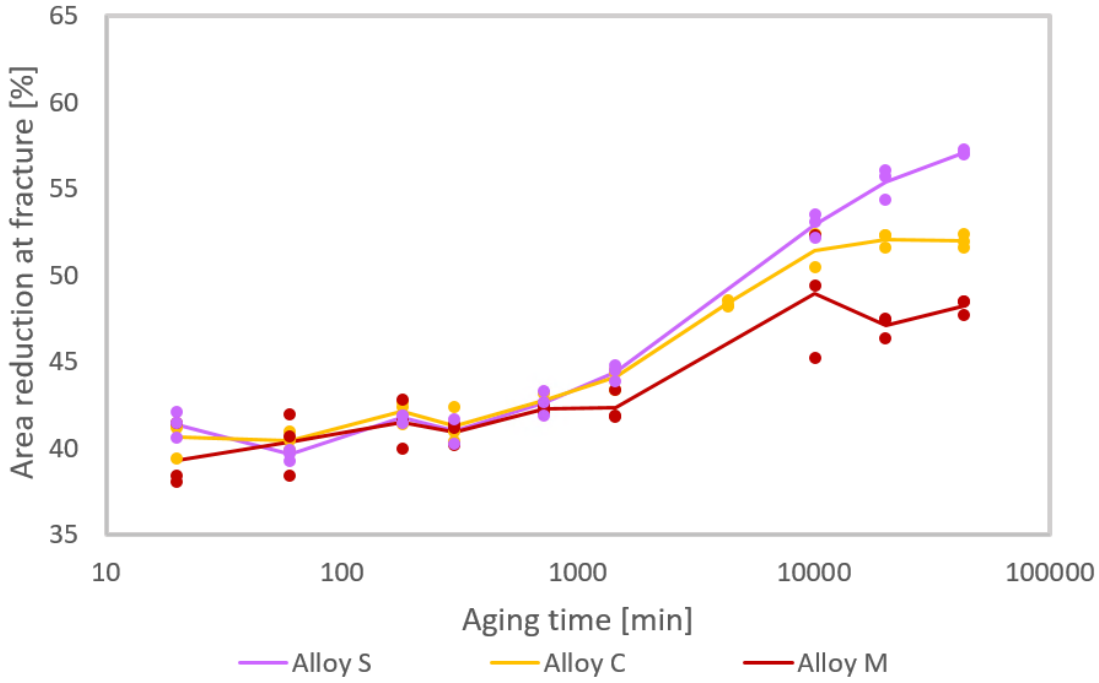

Figure 4.28: Area reduction at fracture for alloy S, C and M at room temperature

Figure 4.28 shows that ductility increases with aging time. Around the peak strength the area reduction is similar for all the alloys. For overaging, the ductility is highest for alloy S. The lowest ductilities were measured at 1 hour for alloy S and C, and at 20 minutes for alloy M. The ductility increase from aging time 1 hour to 1 month is 44% for alloy S, 29% for alloy C and 19% for alloy M. Alloy M has a peak at aging time 1 week, which could possibly be explained by a large spread in the measurements for the three parallels.

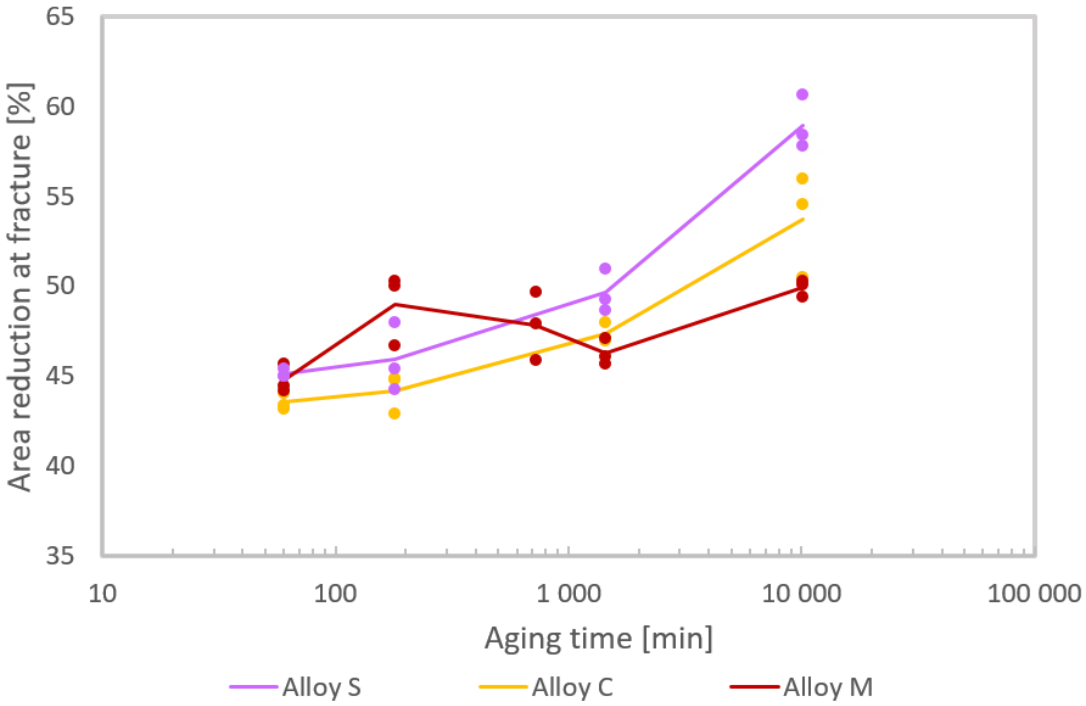

Figure 4.29: Area reduction at fracture for alloy S, C and M at 100°C

Figure 4.29 and 4.30 show that alloy S and alloy C follow the same trend at elevated temperatures as for room temperature, while alloy M stands out. At 100°C, alloy M has a peak ductility for aging time 3 hours, where the average value is slightly higher than for aging time 1 week. The ductility of alloy M at 150°C is less dependent on aging time than alloy S and C.

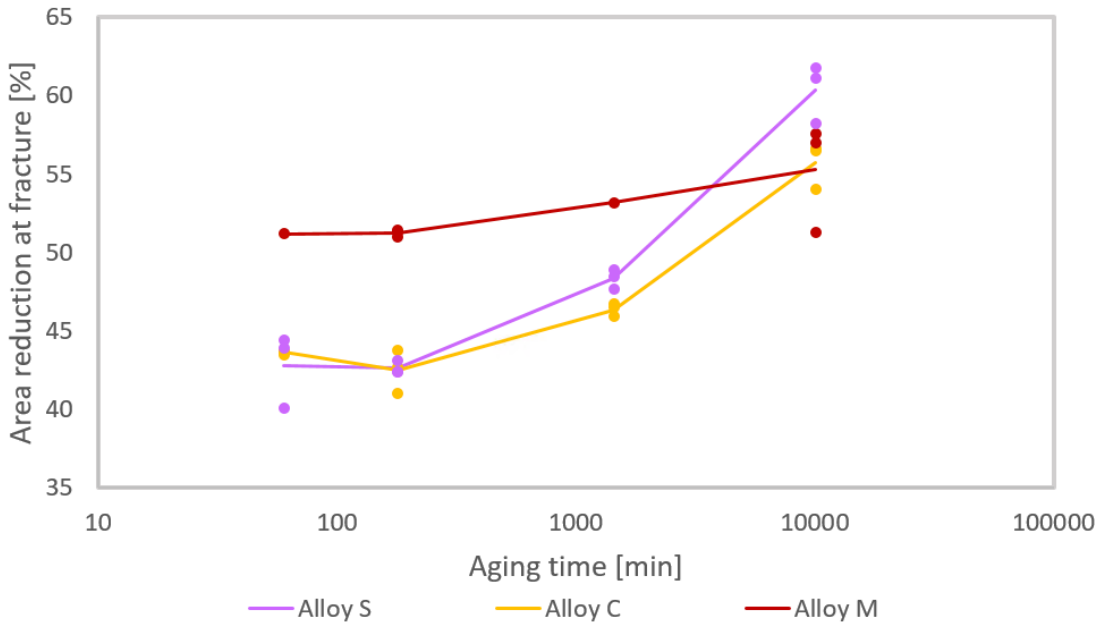

Figure 4.30: Area reduction at fracture for alloy S, C and M at 150°C

The results in Figure 4.31 and 4.32 show a similar temperature dependence for alloy S and alloy C. For short aging times, the ductility for room temperature and 150°C are similar, while for longer aging times, it is similar for 100°C and 150°C. The ductility increase from room temperature to elevated temperature is larger for alloy S than for alloy C at longer aging times.

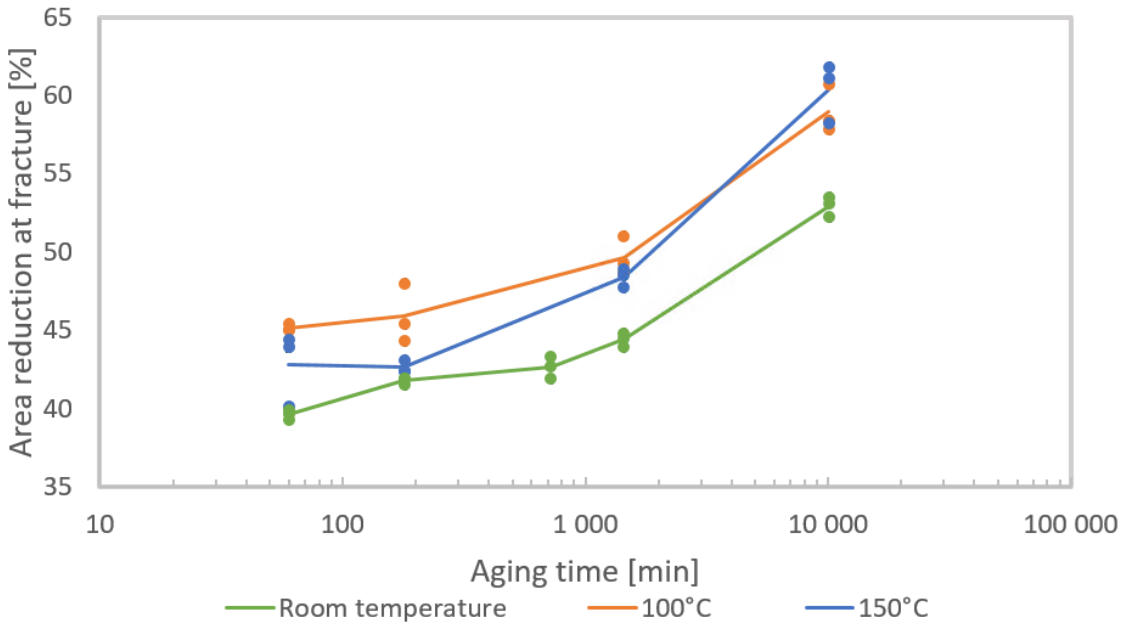

Figure 4.31: Area reduction at fracture for alloy S at room temperature, 100°C and 150°C

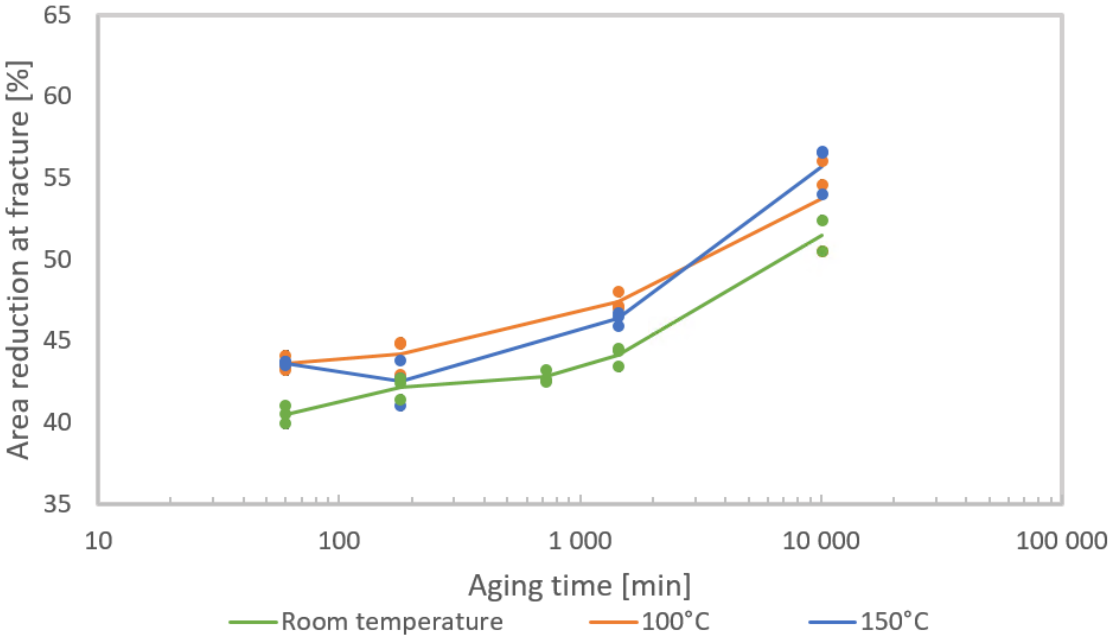

Figure 4.32: Area reduction at fracture for alloy C at room temperature, 100°C and 150°C

The results in Figure 4.33 show that for alloy M. the ductility was highest for 150°C for all aging times, and lowest

was at room temperature.

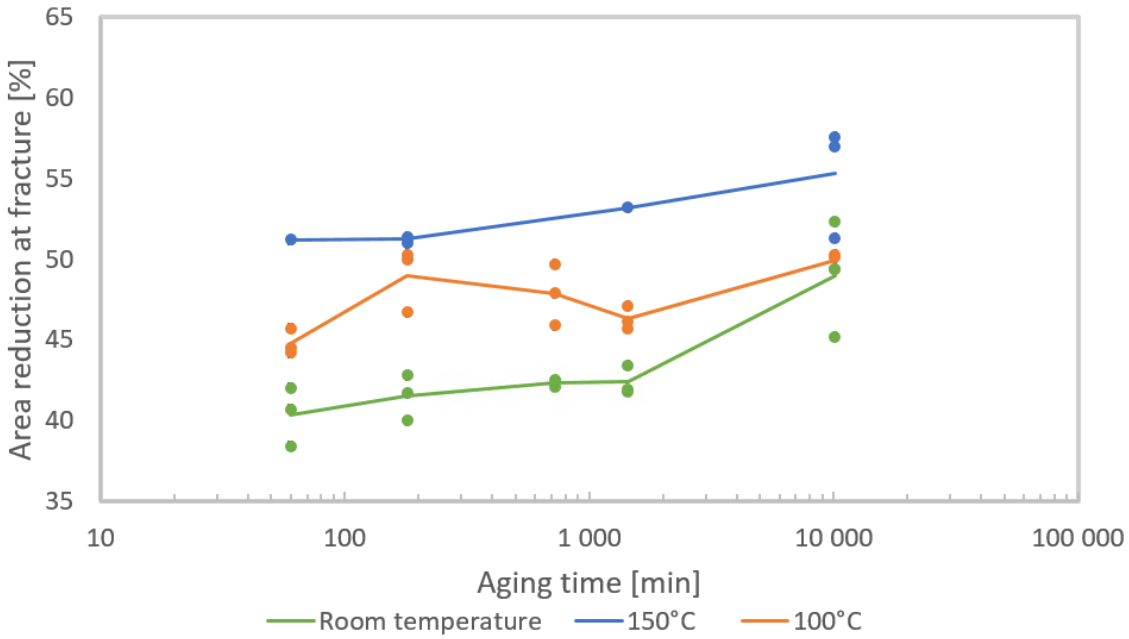

Figure 4.33: Area reduction at fracture for alloy M at room temperature, 100°C and 150°C

Table 4.3: Area reduction at fracture in %

Aging time	Room temperature			100°C			150°C		
	S	C	M	S	C	M	S	C	M
20 minutes	42.1 40.6 41.5	39.4 41.2 41.3	38.4 38.1 41.5	-	-	-	-	-	-
1 hour	39.7 39.9 39.3	39.9 41.0 40.5	42.0 40.7 38.4	45.0 45.4 45.0	44.1 43.3 43.2	44.5 44.2 45.7	43.9 40.1 44.4	43.5 43.7 43.7	51.2
3 hours	41.5 41.9 41.9	41.4 42.7 42.4	42.8 41.7 40.0	48.0 44.3 45.4	42.9 44.8 44.9	46.7 50.3 50.0	43.1 42.4 42.4	41.0 42.7 43.8	51.3 51.4 51.0
5 hours	- 40.3 41.7	41.0 42.3 40.4	41.2 41.4 40.2	-	-	-	-	-	-
12 hours	42.7 43.3 41.9	43.2 42.6 42.5	42.3 42.1 42.5	-	-	45.9 49.7 47.9	-	-	-
24 hours	44.5 44.8 43.9	43.4 44.5 44.4	41.8 41.9 43.4	49.2 51.0 48.7	47.1 48.0 47.0	46.1 47.1 45.7	48.9 48.5 47.7	46.5 46.7 45.9	53.2
3 days	-	48.2 48.6 48.3	-	-	-	-	-	-	-
1 week	53.5 52.2 53.1	- 52.4 50.5	45.2 52.3 49.4	60.7 58.4 57.8	56.0 50.5 54.6	50.1 49.4 50.3	58.2 61.1 62.8	56.6 54 56.5	51.3 57.6 57.0
2 weeks	55.7 54.4 56.1	51.6 52.3 52.3	47.5 46.4 47.4	-	-	-	-	-	-
1 month	57.1 57.0 57.3	52.4 51.6 52.0	47.7 48.5 48.5	-	-	-	-	-	-
24 hours at 250°C	61.0 61.2 59.7	-	-	-	-	-	-	-	-

4.5 Slope for stage IV of work hardening

All the stress-strain curves presented in Appendix A, have a linear work hardening rate for a broad range of strains. In this section, the slope of this work hardening is presented. The development of the slope is given for tensile tests at room temperature in Figure 4.34, at 100°C in Figure 4.35 and at 150°C in Figure 4.36. The slope for each test is marked with a point, while the solid lines drawn between are the average values for the parallels. All the values are given in Table 4.4.

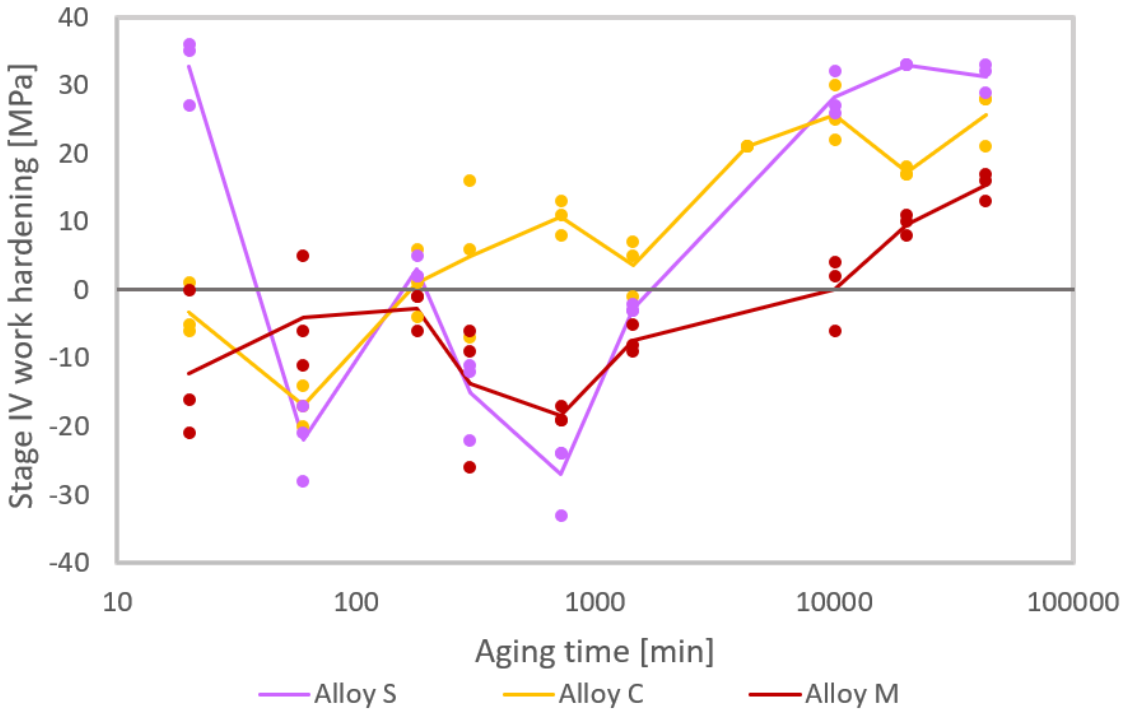

Figure 4.34: Slope for stage IV work hardening for alloy S, C and M at room temperature

The slopes for room temperature tests presented in figure 4.34 show that at for shorter aging times, the slopes were negative or close to zero. The exception is the underaged 20 minutes condition for alloy S. There is no obvious trend for how the slope develops with aging time in this range, but for larger aging times, all alloys have trend of increasing slopes with aging time.

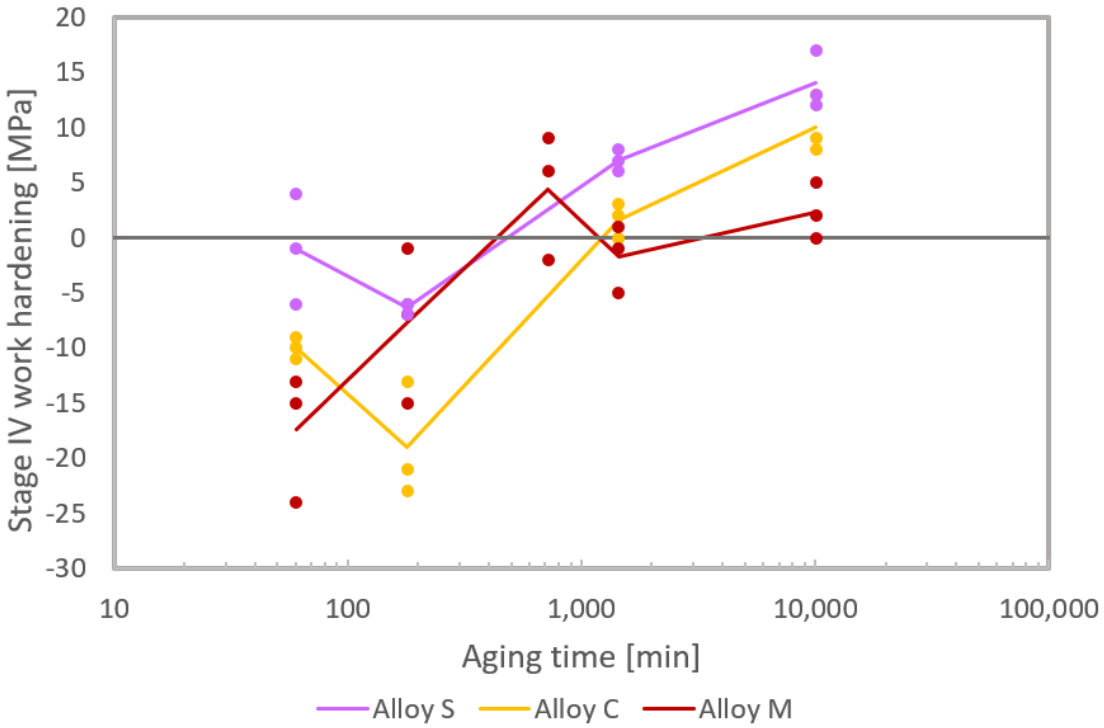

Figure 4.35: Slope for stage IV work hardening for alloy S, C and M at 100°C

Figure 4.35 show that there is an trend of increasing slope with aging time after aging time 3 hours for alloy S and C, while the slope for alloy M is scattered around zero or aging times 12 hours to 1 week.

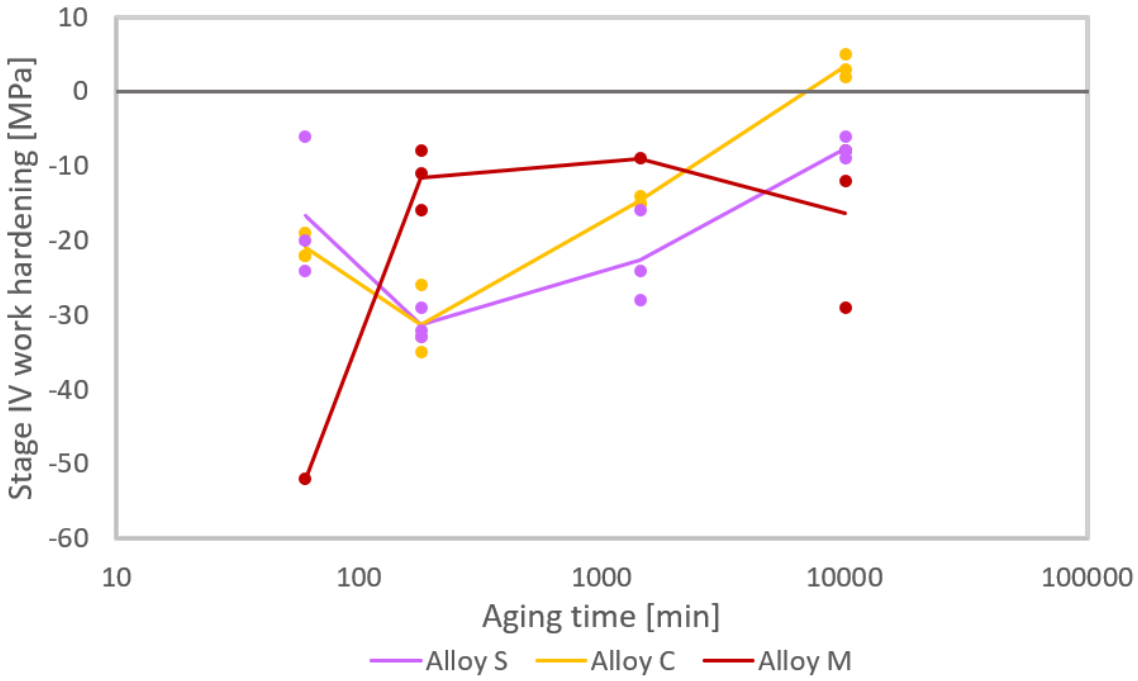

Figure 4.36: Slope for stage IV work hardening for alloy S, C and M at 150°C

The results from 150°C show that the slope is negative for all the curves, except for aging time 1 week alloy C which is slightly positive. The development of the slopes for alloy S and C behaves similarly, with slopes increasing with aging time. Alloy M stands out, with large negative slope for aging time 1 hour, and a slope for longer aging times which is constant within scatter.

The temperature dependency curves for the slopes presented in Figures 4.37 - 4.39 show that 150°C results have a tendency to have the lowers slopes. For alloy S and M, the highest slope alternates between room temperature and 100°C.

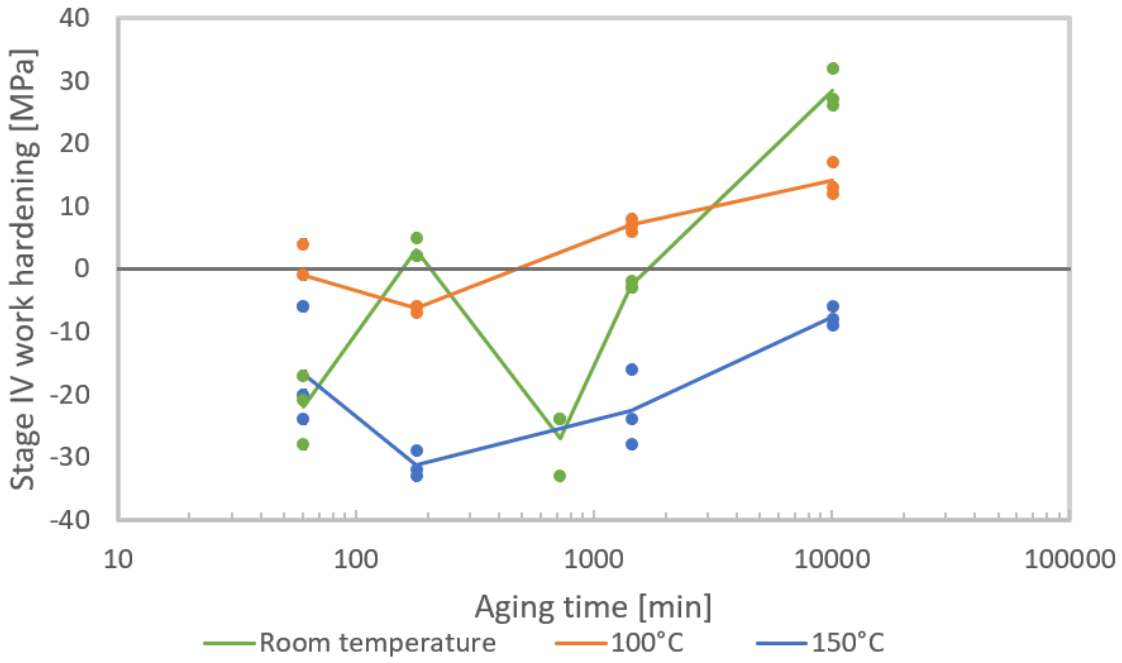

Figure 4.37: Slope for stage IV work hardening for alloy S at room temperature, 100°C and 150°C

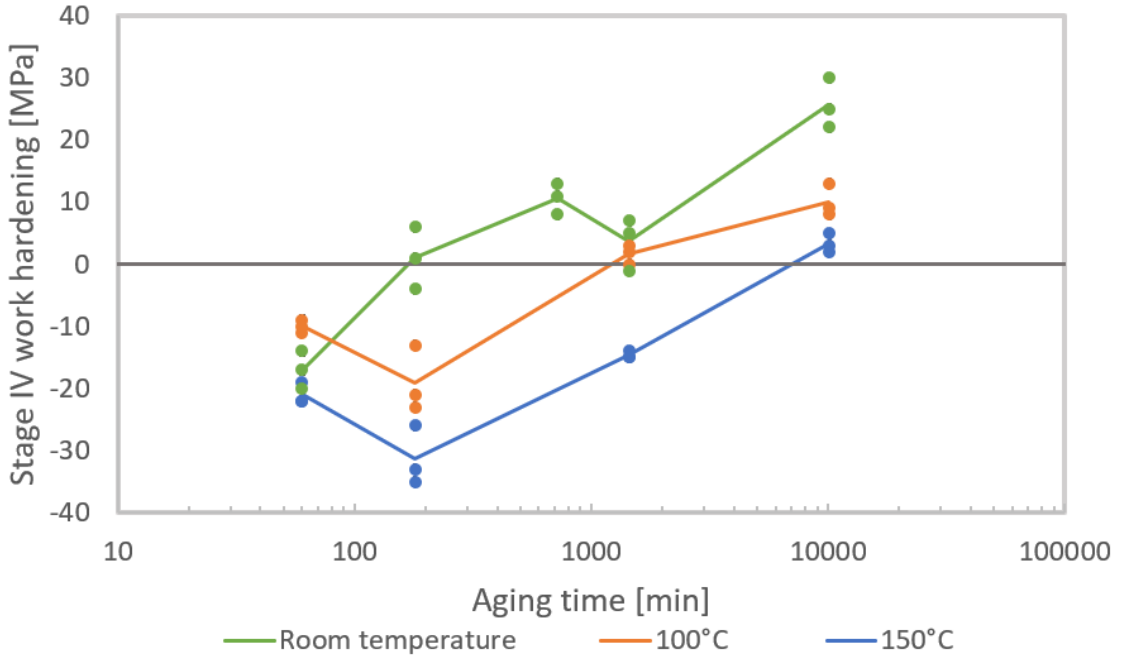

Figure 4.38: Slope for stage IV work hardening for alloy C at room temperature, 100°C and 150°C

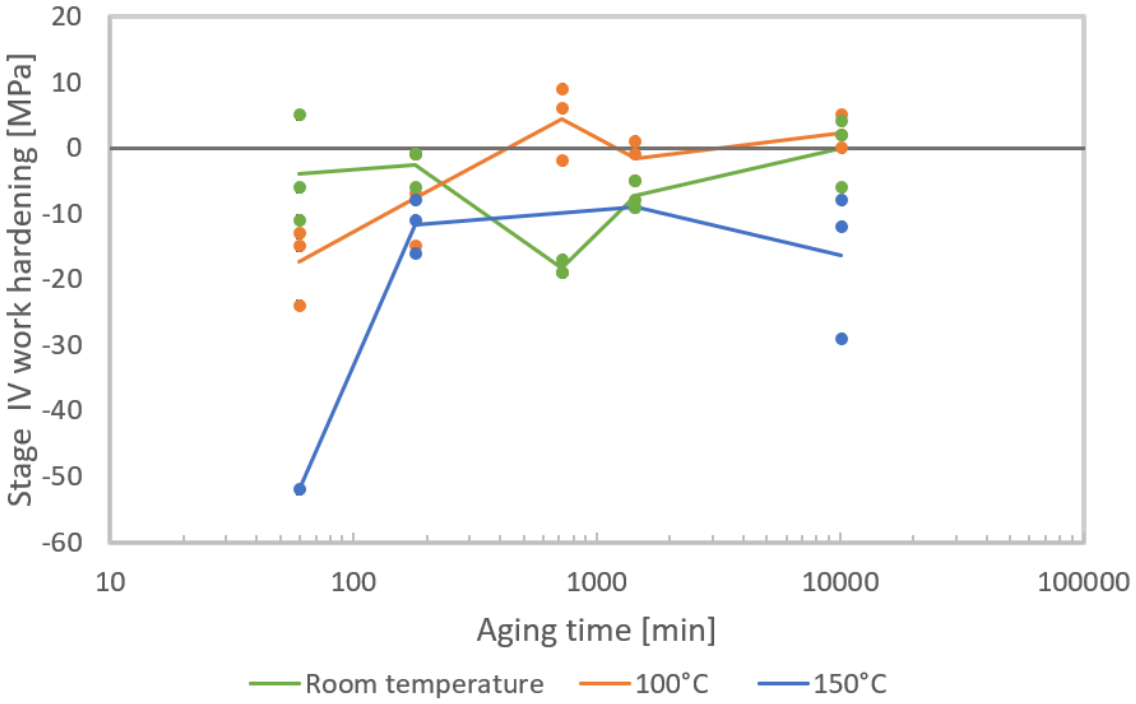

Figure 4.39: Slope for stage IV work hardening for alloy M at room temperature, 100°C and 150°C

Table 4.4: Slope for stage IV work hardening in MPa

Aging time	Room temperature			100°C			150°C		
	S	C	M	S	C	M	S	C	M
20 minutes	36 35 27	-5 -6 1	-21 -16 0	-	-	-	-	-	-
1 hour	-28 -21 -17	-20 -17 -14	5 -11 -6	-6 -4 -1	-11 -9 -10	-15 -24 -13	-20 -24 -6	-22 -19 -22	-52
3 hours	2 5 2	-4 -6 1	-1 -1 -6	-6 -6 -7	-23 -21 -13	-15 -7 -1	-32 -33 -29	-35 -33 -26	-8 -16 -11
5 hours	-12 -22 -11	-7 6 16	-6 -9 -26	-	-	-	-	-	-
12 hours	-24 -24 -33	11 8 13	-17 -19 -19	-	-	6 9 -2	-	-	-
24 hours	-3 -3 -2	-1 5 7	-8 -9 -5	8 6 7	2 0 3	-5 1 -1	-16 -28 -24	-14 -15 -15	-9
3 days	-	21 21 21	-	-	-	-	-	-	-
1 week	32 27 26	22 30 25	4 2 -6	17 12 13	13 8 9	2 5 0	-8 -6 -9	2 3 5	-29 -8 -12
2 weeks	33 33 33	17 17 18	11 8 10	-	-	-	-	-	-
1 month	39 37 38	28 21 28	17 16 13	-	-	-	-	-	-
24 hours at 250°C	32 29 33	-	-	-	-	-	-	-	-

4.6 Development of a/R with strain

The parameters for best fit to equation 3.1 for all the aging conditions are given in Table 4.5 for room temperature, Table 4.6 for 100°C and Table 4.7 for 150°C tensile tests.

Table 4.5: Parameters for best fit to equation 3.1 for tensile tests at room temperature

	S		C		M	
	k_1	k_2	k_1	k_2	k_1	k_2
20 minutes	1.10	0.0068	1.27	0.048	1.18	0.020
1 hour	1.31	0.092	1.22	0.071	1.06	0.019
3 hours	1.11	0.035	1.12	0.044	1.10	0.029
5 hours	1.21	0.053	1.19	0.066	1.17	0.037
12 hours	1.43	0.11	1.08	0.036	1.26	0.05
24 hours	1.29	0.073	1.18	0.057	1.18	0.057
3 days	-	-	1.09	0.041	-	-
1 week	1.05	0.059	1.02	0.035	1.19	0.057
2 weeks	1.06	0.063	1.24	0.13	1.12	0.041
1 month	1.00	0.039	1.08	0.033	1.08	0.025
24 hours at 250°C	1.07	0.15				

Table 4.6: Parameters for best fit to equation 3.1 for tensile tests at 100°C

	S		C		M	
	k_1	k_2	k_1	k_2	k_1	k_2
1 hour	1.12	0.095	1.23	0.16	1.17	0.081
3 hours	1.11	0.075	1.28	0.17	1.12	0.085
12 hours	-	-	-	-	1.06	0.052
24 hours	1.05	0.061	1.11	0.086	1.11	0.08
1 week	1.05	0.089	1.06	0.092	1.13	0.073

Table 4.7: Parameters for best fit to equation 3.1 for tensile tests at 150°C

	S		C		M	
	k_1	k_2	k_1	k_2	k_1	k_2
1 hour	0.99	0.081	1.14	0.11	1.79	0.35
3 hours	1.14	0.10	1.33	0.20	1.04	0.069
24 hours	1.22	0.18	1.08	0.074	1.18	0.14
1 week	1.31	0.25	1.07	0.12	1.24	0.20

There is no clear correlation between k_1 and k_2 with aging time, alloy or temperature. k_1 is in the range from 0.99 to 1.79, both extremes are from the 150°C results. The average value for k_1 is 1.16 and the median value is 1.12. k_2 is in the range from 0.0068 to 0.25. The average value is 0.086 and the median value is 0.072. The experimental values, the best fit and the values predicted by the finite element model are shown in Figure 4.40 for aging time 20 minutes, 4.41 for aging time 3 hours and 4.42 for aging time 24 hours at 250°C, all for alloy S.

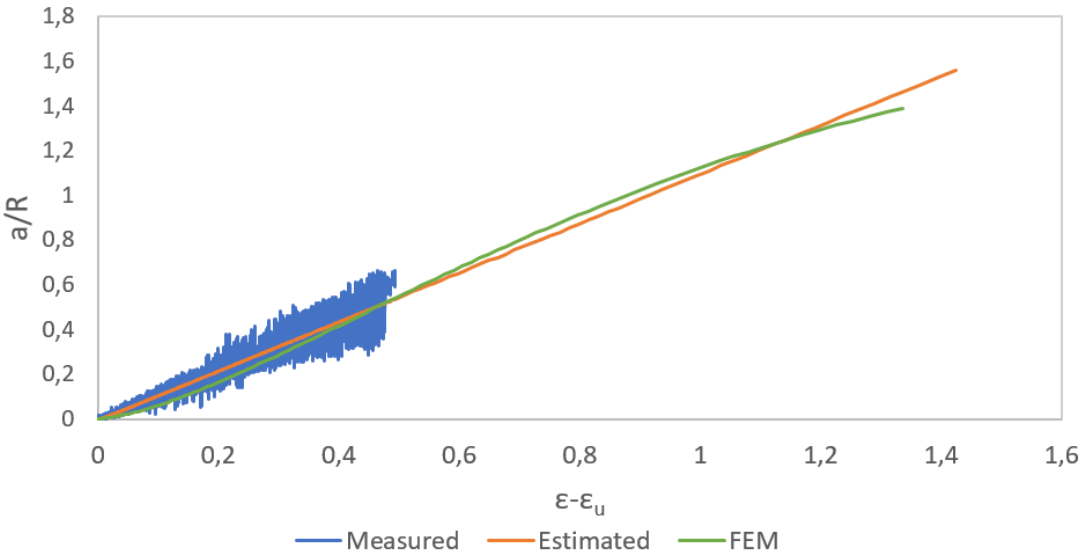

Figure 4.40: Development of a/R with strain after uniform strain for alloy S aging time 20 minutes

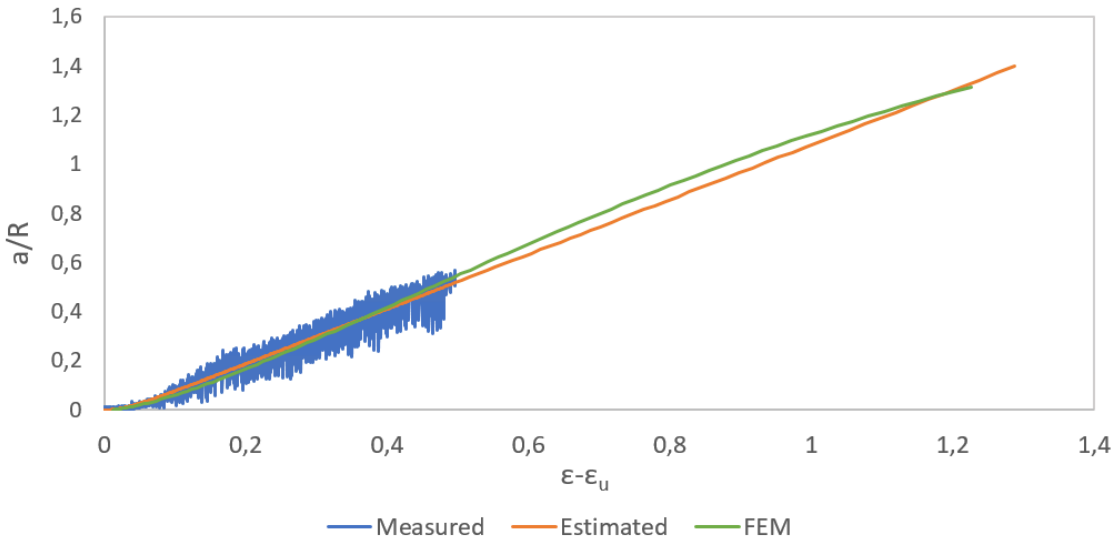

Figure 4.41: Development of a/R with strain after uniform strain for alloy S aging time 3 hours

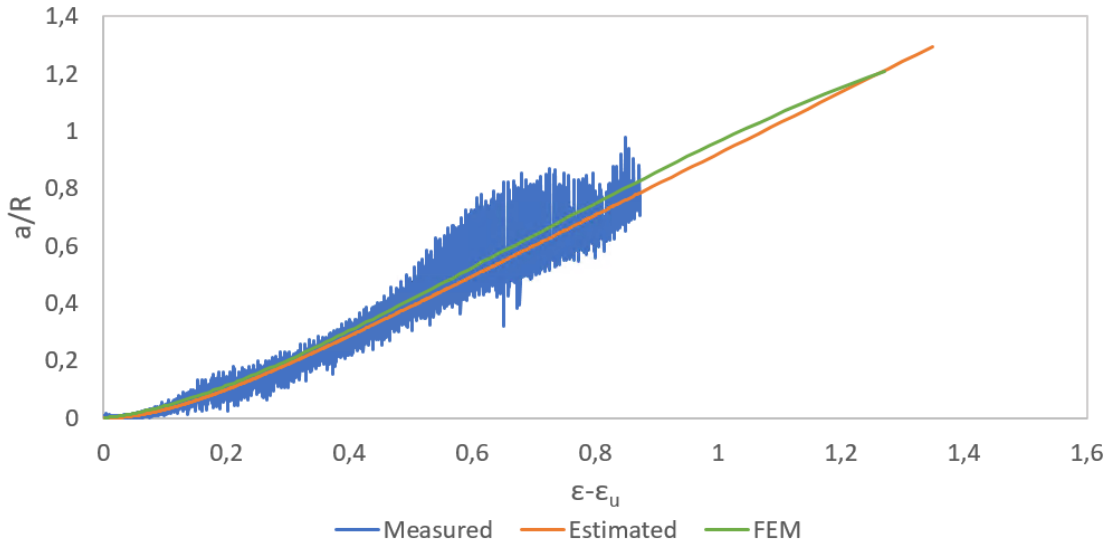

Figure 4.42: Development of a/R with strain after uniform strain for alloy S aging time 24 hours at 250°C

Figures 4.40 - 4.42 show that the FEM results are similar to the best fit, and both fit the experimental data well. For large strains, the best fit model predicts a linear relationship between $\frac{a}{R}$ and strain, while the FEM analysis predicts a decreasing slope.

4.7 Kocks-Mecking curves

In this section, a selection of the Kocks-Mecking curves are presented. The curves from parallel tests can be shifted on the x-axis due to their measured yield strength being different. This makes it difficult to interpret the results from looking at the curves directly. For this reason, a limited number of curves is presented in this section. All curves are presented in Appendix B and the parameters describing the curves are presented in Section 4.8.

The Kocks-Mecking curves for all the parallels for alloy M, aging time three hours for tensile test at room temperature, 100°C and 150°C are presented in Figure 4.43. The results show that for a given stress after the yield strength, the slope usually decreases with tensile test temperature, which is a trend in a majority of the Kocks-Mecking curves presented in Appendix B.

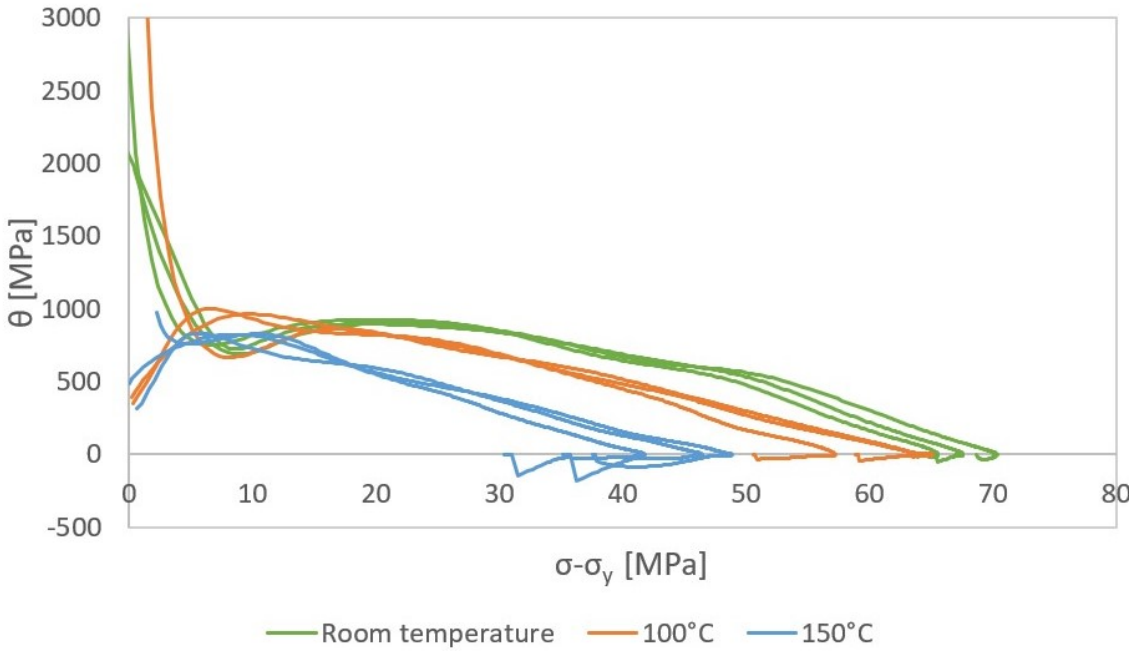

Figure 4.43: Kocks-Mecking plot for alloy M aging time 3 hour

The aging time dependency of the Kocks-Mecking curve for alloy M at room temperature is presented in Figure 4.44. The curves for aging times 1 hour - 24 hours are similar when it comes to both values and in shapes. The curve for aging time 20 minutes has a similar shape but a larger value. The curves for aging times 2 weeks and 1 month are similar to each other.

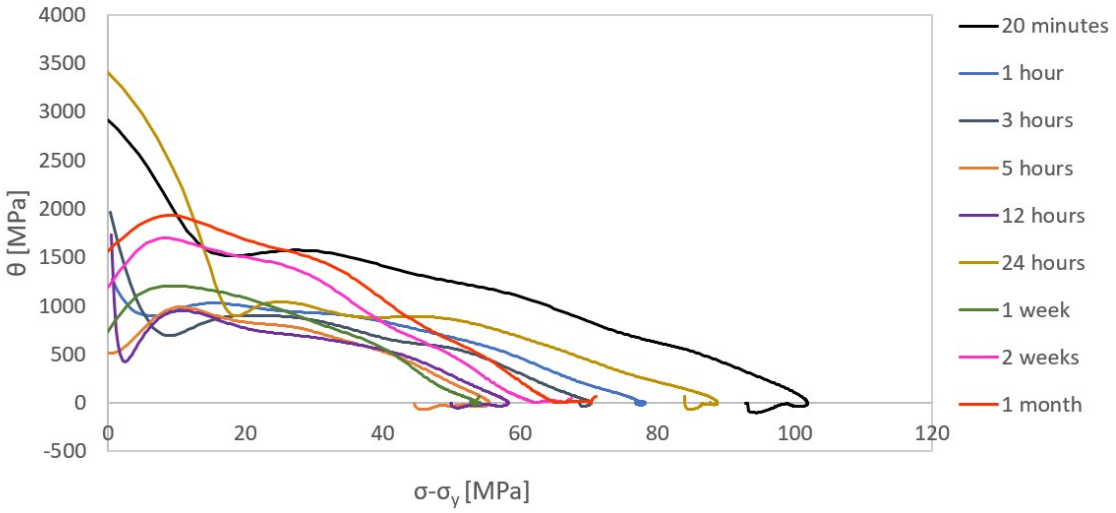

Figure 4.44: Kocks-Mecking plot for all aging times for alloy M for tensile test at room temperature

4.8 $-\frac{d\theta}{d\sigma}$ and θ_{max}

4.8.1 Alloy S

$-\frac{d\theta}{d\sigma}$ for alloy S for room temperature, 100°C and 150°C are presented in Figure 4.45. For all temperatures, the value is constant at 25 for short aging times and increasig for longer aging times. At room temperature, there is a slight increase between 24 hours and 1 week, and a larger increase to 2 weeks. The value is then stable at approximately 50. The scatter for 100°C results makes it difficult to determine if the value increases between 3 hours and 24 hours, but there is a clear increase after 24 hours. At 150°C the value also increases after 24 hours for two of the parallel specimens, while one remains at the lower level.

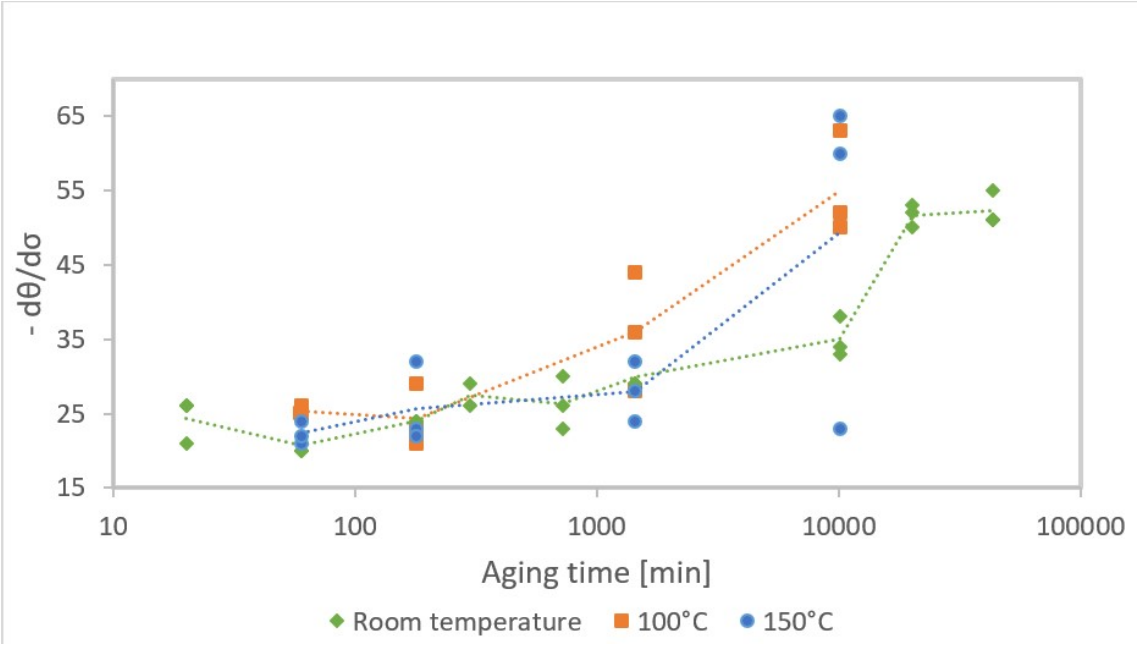

Figure 4.45: $\frac{d\theta}{d\sigma}$ for alloy S

The θ_{max} results for alloy S is shown in Figure 4.46. The room temperature tests are approximately constant aging times between 1 and 24 hours. The value is larger for shorter and longer aging times. The 100°C and 150°C results are approximately constant for all the aging times. There is a trend that θ_{max} decreases slightly with increasing temperature.

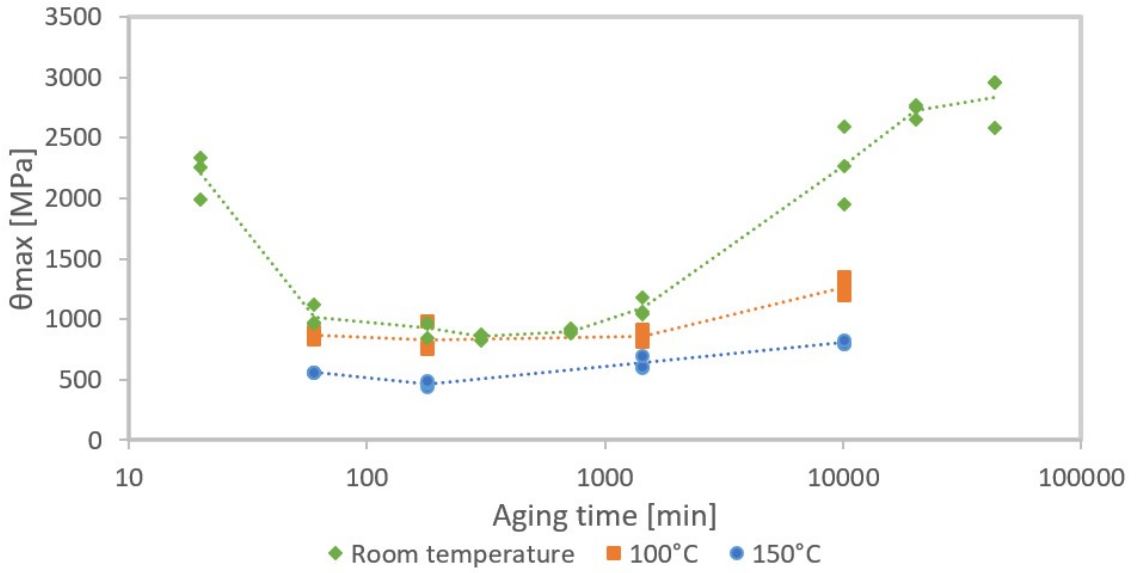

Figure 4.46: θ_{max} for alloy S

4.8.2 Alloy C

$-\frac{d\theta}{d\sigma}$ for alloy C at room temperature, 100°C and 150°C is presented in Figure 4.47. For all the temperatures, the value is constant at approximately 25 up until after aging time 24 hours. For longer aging time the value increases for all temperatures. The room temperature value is stable around 50 for aging times 1 week to 1 month.

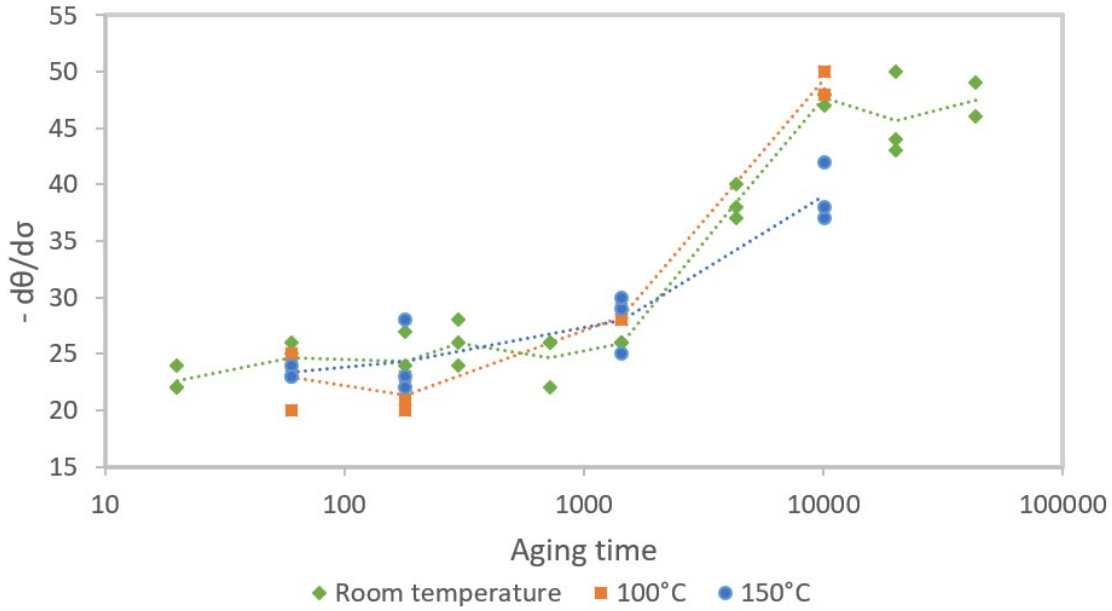

Figure 4.47: $\frac{d\theta}{d\sigma}$ for alloy C

The results for θ_{max} for alloy C at room temperature, 100°C and 150°C are presented in Figure 4.48. The room temperature and 100°C results are constant for aging times 1 hour to 24 hours, and higher values for shorter and longer aging times. For 150°C, the value is approximately constant for all the aging times.

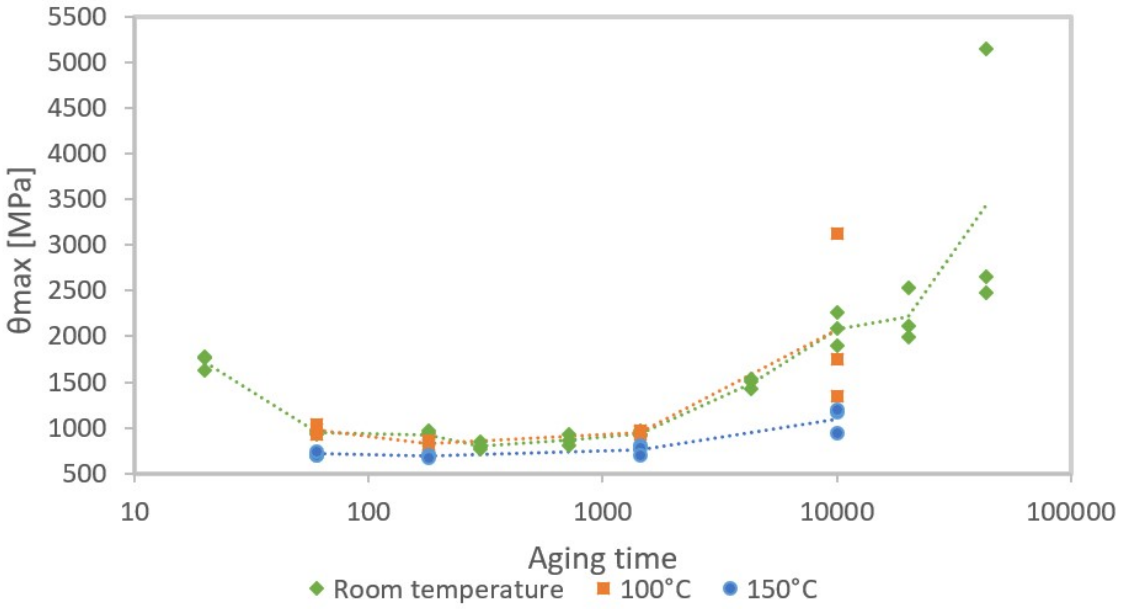

Figure 4.48: θ_{max} for alloy C

4.8.3 Alloy M

$-\frac{d\theta}{d\sigma}$ for alloy M at room temperature, 100°C and 150°C is presented in Figure 4.49. For all the temperatures, the slope is constant at approximately 20 for aging times before 24 hours. At room temperature and 100°C the value increases with aging times. There is no obvious stabilizing for alloy M for the longest aging times. At 150°C $-\frac{d\theta}{d\sigma}$ for two of the parallels remain at the low constant level, while the last one increases.

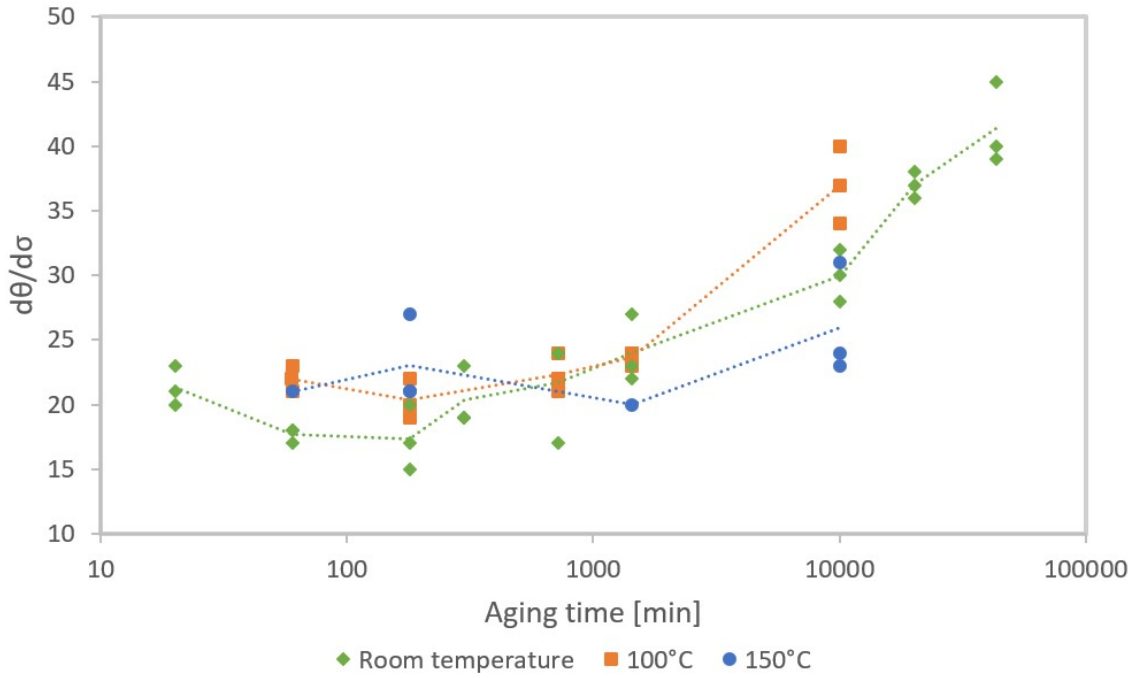

Figure 4.49: $\frac{d\theta}{d\sigma}$ for alloy M

The results for θ_{max} for alloy M are presented in Figure 4.50. For room temperature and 100°C the value is approximately constant for aging times 3-24 hours. For 150°C it is constant for aging times 3 hours-1 week. The value is larger for shorter and longer aging times.

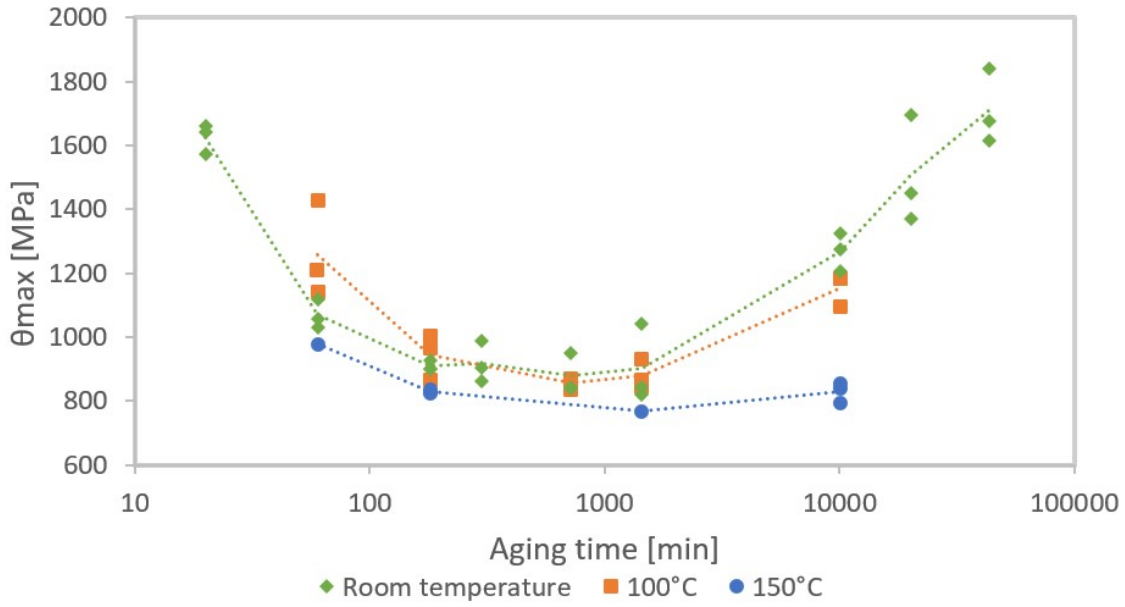

Figure 4.50: θ_{max} for alloy M

4.9 Commercial pure aluminium

The yield strength and true uniform strength for commercial pure aluminium are given in Table 4.8. Area reduction at fracture was not measured because the area changed during repolishing.

Table 4.8: Yield strength and true uniform strength for pure aluminium

Yield strength [MPa]	True uniform strength [MPa]
23	101
22	101
21	107

Development of $\frac{a}{R}$ with strain after uniform stain is shown in Figure 4.51. Fitting of the experimental data to equation 3.1 resulted in much larger values for k_1 and k_2 than what was presented for alloy S, C and M in section 4.6.

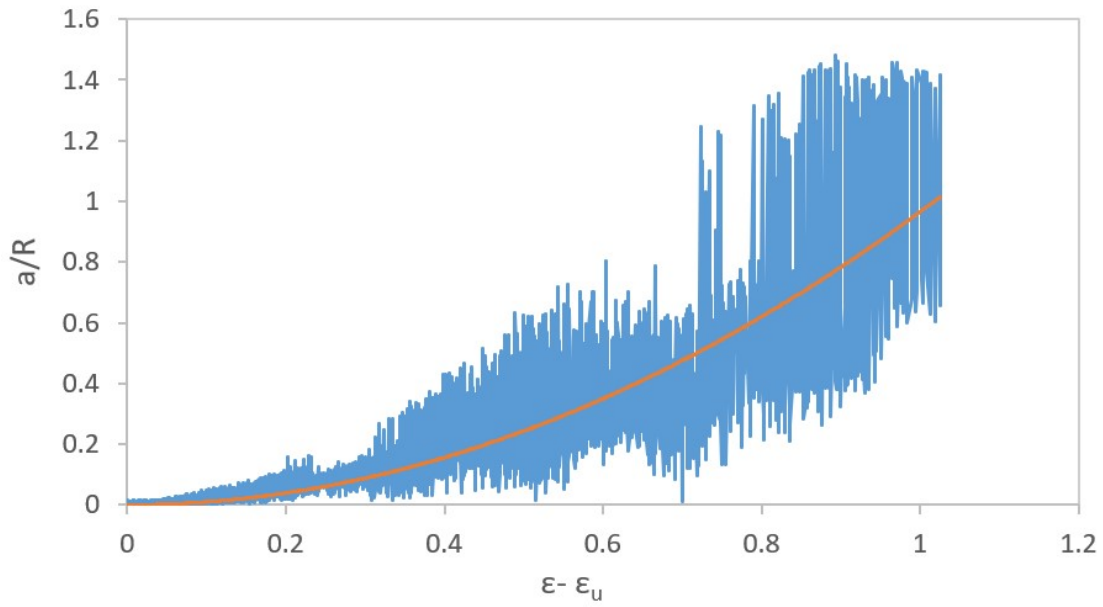

Figure 4.51: Development of $\frac{a}{R}$ with strain after uniform strain for pure aluminium

For the fitted curve in the figure, $k_1 = 43$ and $k_2 = 958$. As mentioned, the expression is the sum of an exponential part and a linear part, where the linear part dominates at large strains. However, for pure aluminium the exponential part dominates for the whole curve, which affects the fit. In Figure 4.52, an additional fit is added, which has parameters more similar to the AlMgSiCu-parameters. This also fits the data well, and as shown in Figure 4.53, these parameters give a more realistic prediction to larger strains.

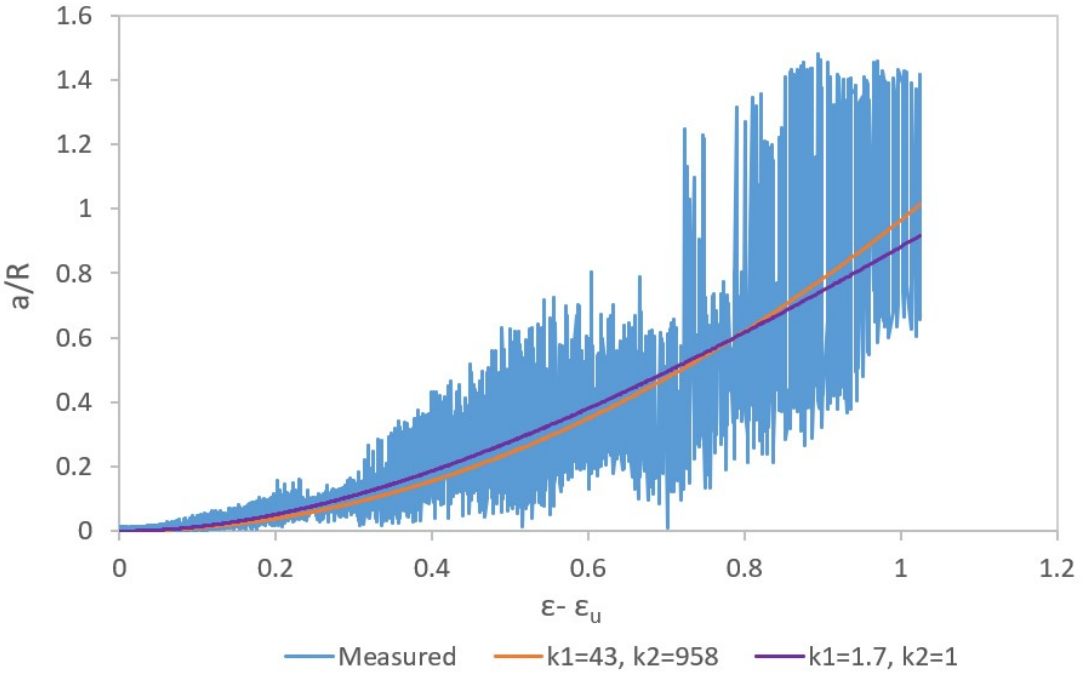

Figure 4.52: Development of $\frac{a}{R}$ with strain after uniform strain for pure aluminium, with two sets of parameters for equation 3.1

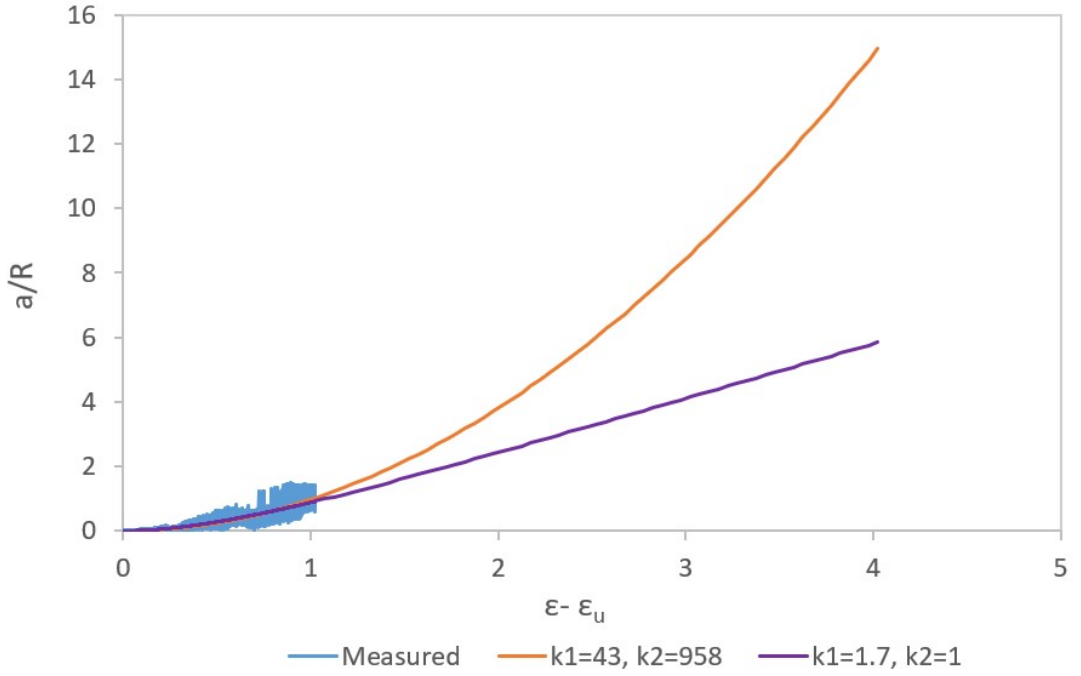

Figure 4.53: Prediction to larger strains for two sets of parameters in equation 3.1

The stress-strain curves for pure aluminium are shown in Figure 4.54

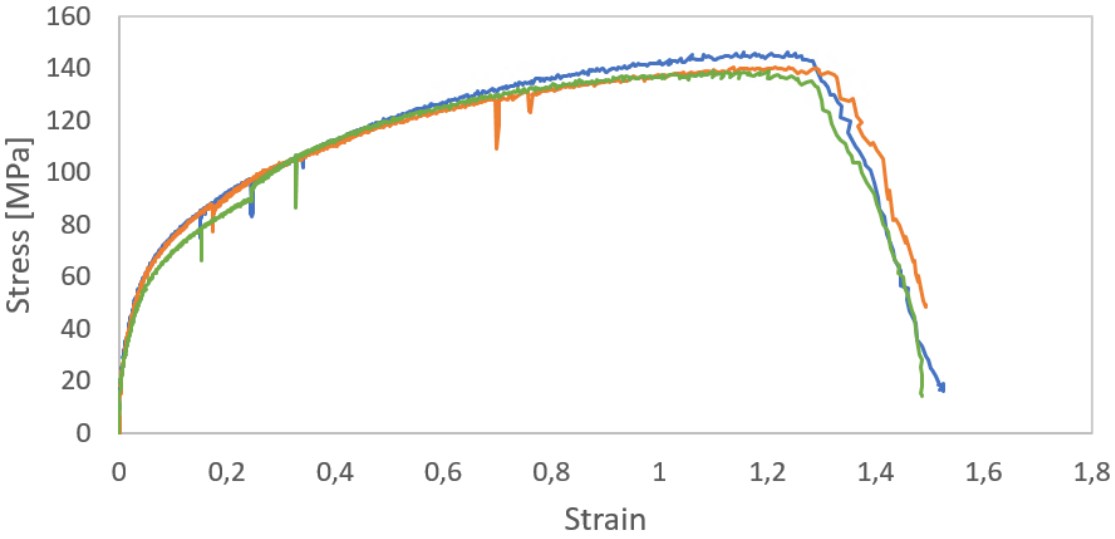

Figure 4.54: Stress-strain curves for pure aluminum

The Kocks-Mecking plot for pure aluminium is shown in Figure 4.55

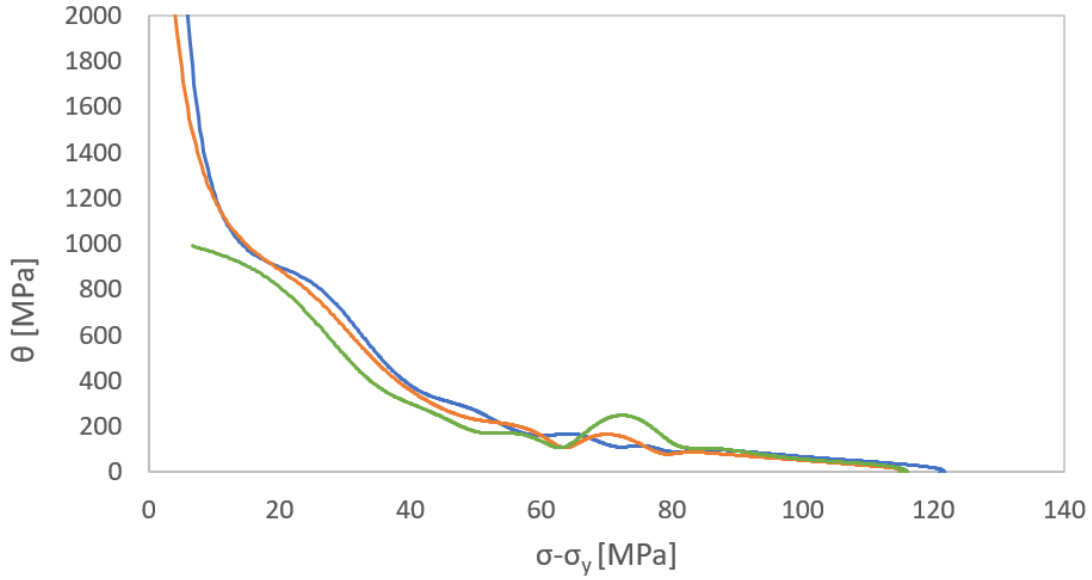

Figure 4.55: Kocks-Mecking plot for pure aluminum

4.10 Effect of exponent n for addition of strength contributions

The strength of a selection of the stress-strain curves has been split into the dislocation contribution σ_d and precipitate contribution σ_p for chosen values of n between 1 and 2. This was done by Equations 2.30 and

2.31. Based on the precipitate statistics from Jonas Sunde [27] from Table 2.1, the contribution from storage of dislocations has also been modeled for small plastic strains. Equation 2.21 describes the storage rate of dislocations when the slip length is L. In the case of small plastic strains, the slip length is determined by the concentration of precipitates, and $L = \frac{C_p}{\sqrt{P}}$, where P is determined by Equation 2.25. This means that the increase in dislocation density with strain for this case is given in Equation 4.1.

$$\frac{d\rho}{d\gamma} = \frac{2\sqrt{P}}{bC_p} \tag{4.1}$$

Equation 4.1 can easily be integrated and combined with Equations 2.21 and 2.10, as presented in Equation 4.2.

$$\sigma_d = M\alpha Gb\sqrt{\rho_0 + \frac{2\sqrt{P}\gamma}{bC_p}} = M\alpha Gb\sqrt{\rho_0 + \frac{2\sqrt{P}M\epsilon}{bC_p}} \tag{4.2}$$

In Equation 4.2, ρ_0 is the initial dislocation density. In this model it is set to $10^{11}m^{-2}$. C_P is set to 30 in the model, assuming that approximately 30% of the precipitates act as pinning points. σ_d calculated here should be the maximum increase in dislocation stress with the present obstacles.

The dislocation stress contribution for various n and the model results for aging time 3 hours and 24 hours for all alloys are presented in Figures 4.56 - 4.61. All experimental results are from room temperature tensile test.

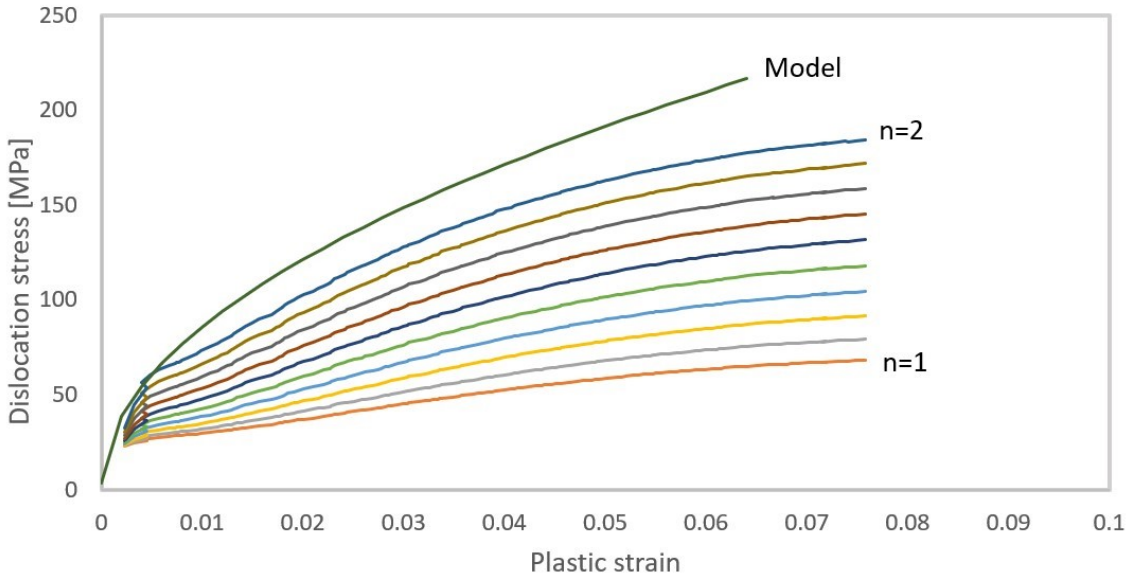

Figure 4.56: Modelling and experimental results for dislocation contribution to the total stress for alloy S aging time 3 hours for various values of n

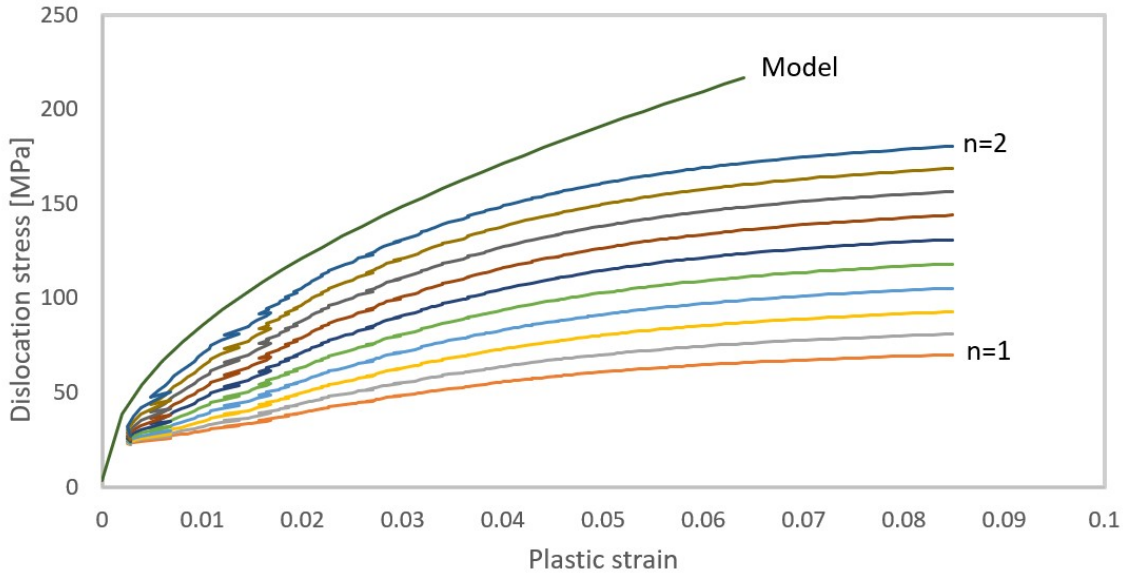

Figure 4.57: Modelling and experimental results for dislocation contribution to the total stress for alloy S aging time 24 hours for various values of n

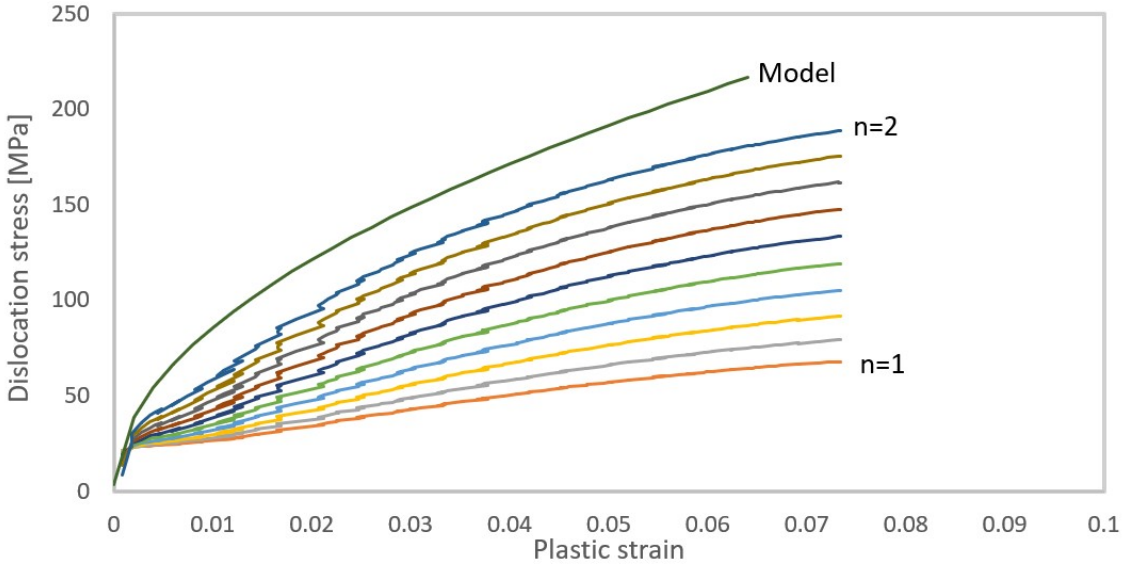

Figure 4.58: Modelling and experimental results for dislocation contribution to the total stress for alloy C aging time 3 hours for various values of n

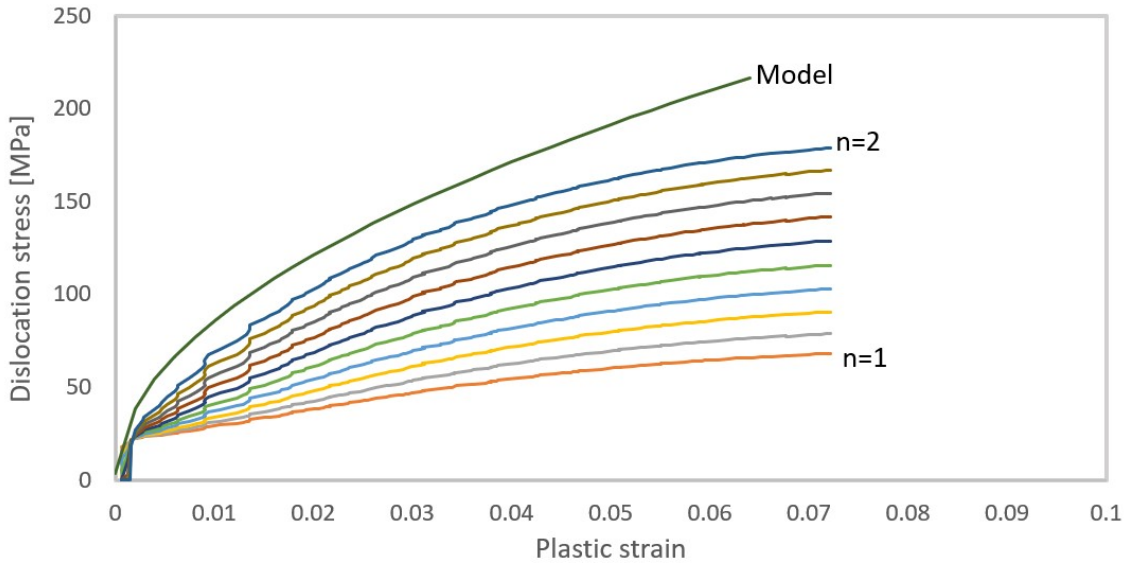

Figure 4.59: Modelling and experimental results for dislocation contribution to the total stress for alloy C aging time 24 hours for various values of n

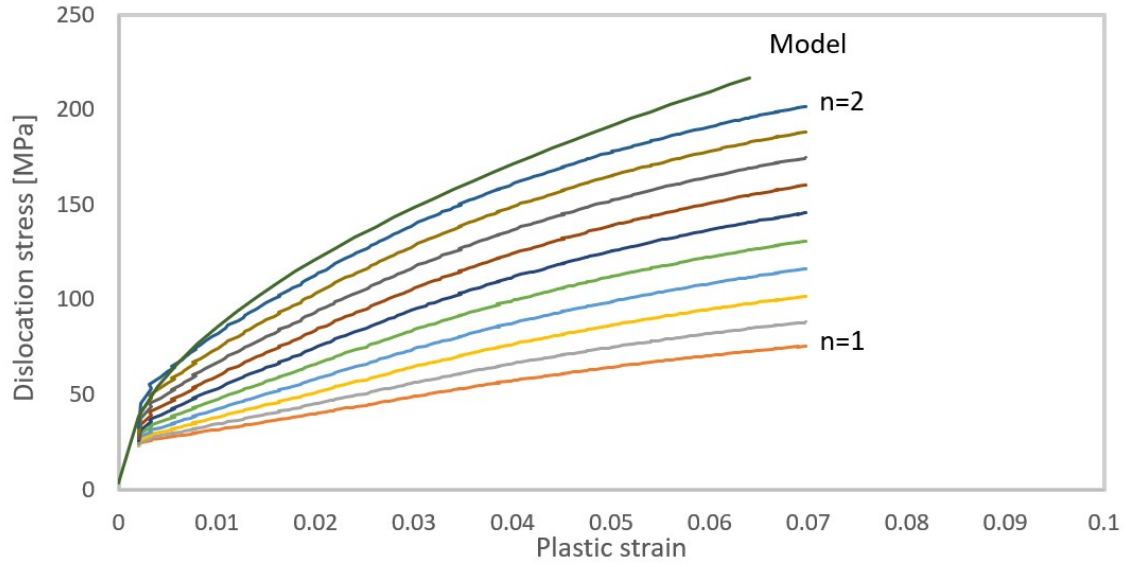

Figure 4.60: Modelling and experimental results for dislocation contribution to the total stress for alloy M aging time 3 hours for various values of n

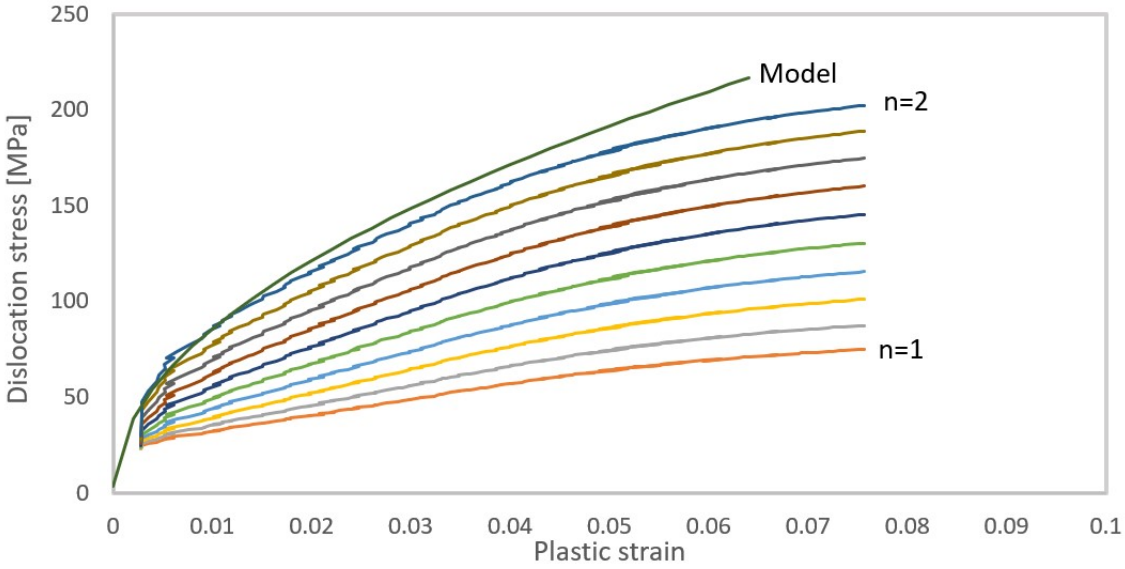

Figure 4.61: Modelling and experimental results for dislocation contribution to the total stress for alloy M aging time 24 hours for various values of n

¨ The results show that the model prediction of the dislocation contribution to the stress is larger than the experimental results for all n.

5 Discussion

5.1 Heat tolerance for mechanical properties of the alloys

The values extracted from the stress-strain curves show that the development of alloys S and C with both aging time and tensile temperature is very similar. The shape of the curves for yield strength and true uniform strength are almost identical, and the strength of alloy C is generally stronger than alloy S. Their development of ductility also follow the same trend, where generally alloy S is more ductile.

The development of the mechanical properties for alloy M stand out compared to alloy S and C. The peak strength plateaus for both yield strength and true uniform strength are broader, and the loss of both yield strength and true uniform strength is less severe than for the other two alloys. This is true at both room temperature and the elevated temperatures. The decrease in strength when the temperature is increased is also slightly lower for alloy M than alloy C and S. Additionally, the higher strength at elevated temperature is not on expense of ductility, especially at 150°C where the measured ductilties were independent of aging time for alloy M.

However, around peak strength, the mechanical properties for alloy C and M are equal within the scatter of the results, except when it comes to ductility at elevated temperatures. The degree of overaging studied in this thesis is not relevant for most industrial applications. If extreme overaging or a high ductility at elevated temperature is required, alloy M is the better choice. If not, alloy C can perform equally well.

5.1.1 Work hardening and saturation of dislocation density

In section 4.1, a large amount of stress-strain curves are presented. For all the curves, a very high flow stress is achieved in stage II, followed by a limited work hardening rate. Work hardening softening and saturation are all observed. Both the slopes at Stage IV work hardening and θ_{max} results indicate a low dislocations storage rate, especially at elevated temperature.

One possibility for the rapid saturation was that the formation of substructures was prevented by the large fraction of precipitates. In this case, the dislocation density should be approximately the same at saturation for all the conditions, and the variations should be due to precipitates. However, only some conditions reached saturation, and also substructure was detected in a deformed T6 Al-Mg-Si alloy by Kelfa *et al.* [36].

5.1.2 Recrystallization of alloy M

The mechanical properties of the alloys indicate that alloy M has the highest heat tolerance. However, an important limitation with alloy M is its sensitivity to recrystallization. Ketill Pedersen and Helen Langeng from SINTEF [37] studied the cross section area from the center to the circumference of the extruded bar before and after heat treatment for alloy S and M. The unpublished images are shown in Figure 5.1, where the scale bar is 1 mm. The

images show that before heat treatment, both alloys has a recrystallized layer, which is thicker for alloy M. After heat treatment to T6, the recrystallized layer did not grow for alloy S, but grew considerably for alloy M.

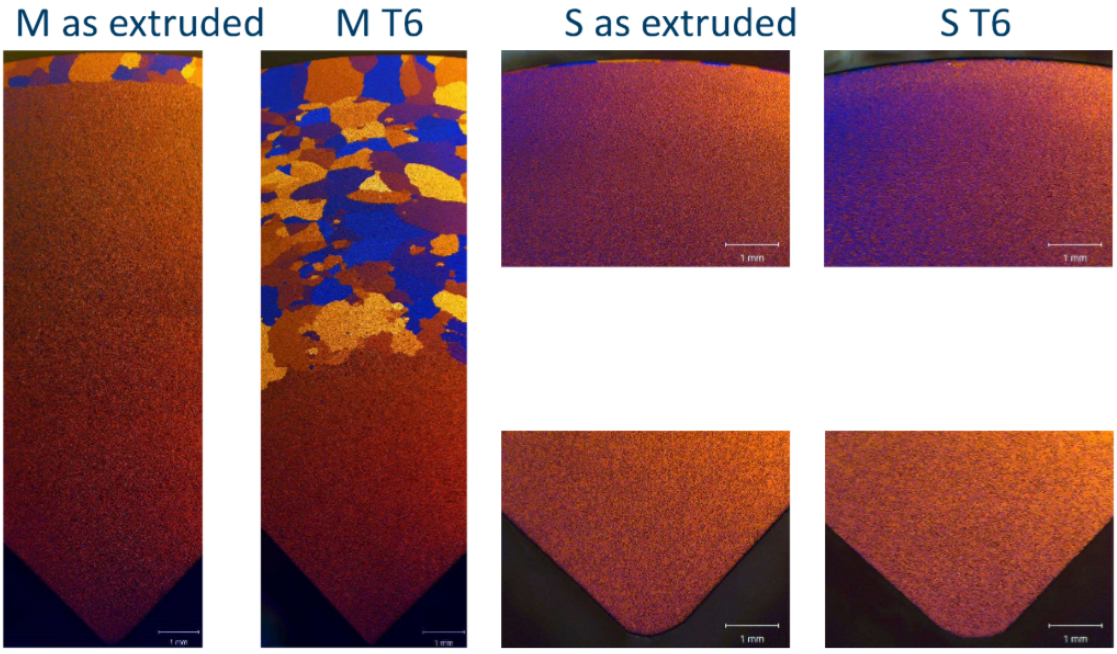

Figure 5.1: Recrystallization of alloy M compared to alloy S. Light optical microscope images from [37]. The scale bar is 1 mm

To avoid recrystallization, specimens were machined from the middle of the extruded bar, and no problems with recrystallization were originally encountered for alloy M. However, tensile tests of specimens from a second batch of M material gave unexpected results. The strength was lower and ductility was higher than expected, and the deformation was not axisymmetric, as can be seen clearly from Figure 5.2.

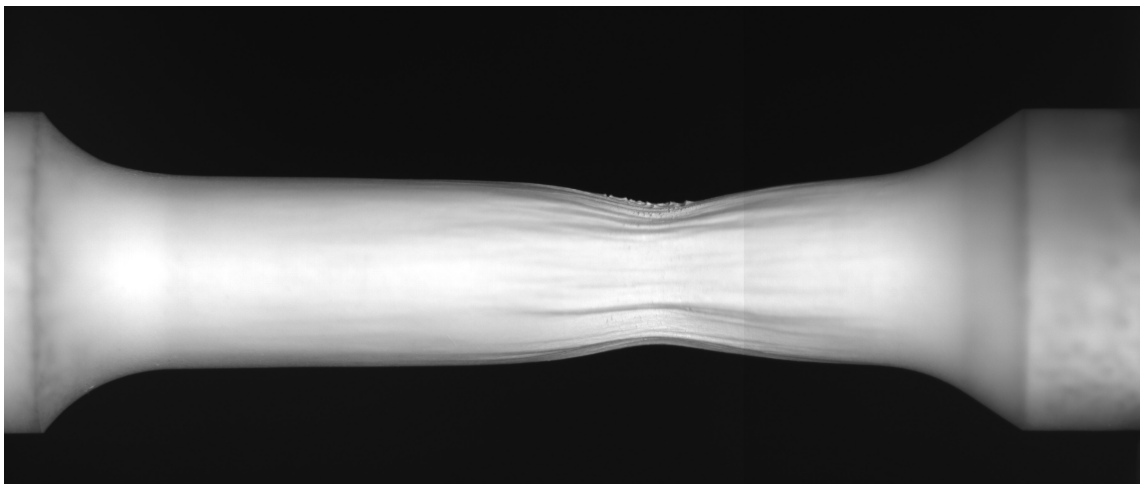

Figure 5.2: Image from tensile test with second batch of alloy M.

This specimen was studied the optical light microscope by the author, and recrytallization was discovered. The grain structure is shown in Figure 5.3, where the scale bar is 100μm.

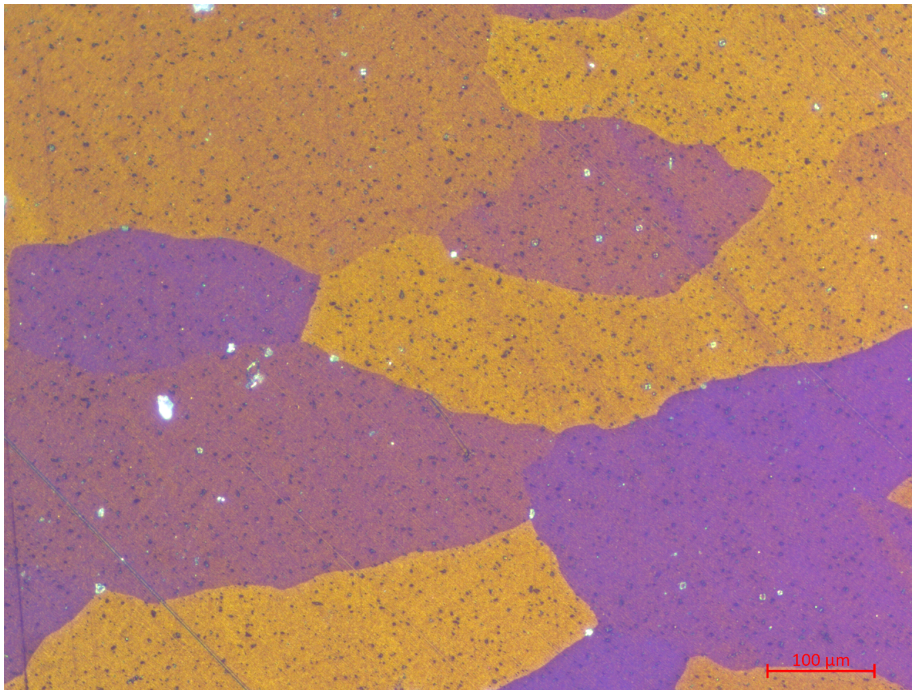

Figure 5.3: Grain structure of specimen in figure 5.2

The reason for the recrystallization has not been investigated due to time restraints, but the two main hypotheses were changes in composition or extrusion parameters.

5.2 Shearable transition

According to Cheng *et al.* [28], the shearable transition is revealed by a sudden increase in the value of $\frac{d\theta}{d\sigma}$ as a function of aging time. The result presented in Section 4.8 indicate that the shearable transition is after 24 hours for all the alloys. The transition point is most clear for alloy C. For alloy S the transition point could also be after aging time 1 week.

In agreement with Cheng *et al.*, the value for alloy S and C stabilizes after the increase, at a value approximately twice as high as before the jump. It is unclear from the result if the value stabilizes or increases slightly for alloy M.

It is interesting that the shearable transition for alloy M seems to be the same point as alloy S and C, as the transition from shearable to non-shearable precipitates often is associated with overaging. If the shearable transition is after 24 hours, this is in agreement with the end of the true uniform strength plateau. The yield strength plateau for yield strength ends right before aging time 24 hours for alloy S and C, while for M it is included in the plateau.

The modelling experiment in Section

5.3 Method and analysis

A discussion of the method is included because the set up and script for analysis has been developed specifically for this project, and certain error sources and special considerations should be commented.

5.3.1 Considerations for elevated temperature tensile tests

The specimen was placed in the heat chamber 10 minutes before the test started. This was necessary to ensure sufficient heating of the specimen, but there may be some unwanted aging in this time. A typical tensile test duration was approximately 10 minutes, which means a total of 20 minutes with elevated temperature exposure. Of course the effect will more significant for shorter aging time and at 150°C.

The importance of heating the chamber for hours before tensile tests was discovered after the first day of tests at elevated temperature. There was a large spread in strength between the parallels of the same alloy and aging condition, and the strength appeared to decrease from morning to afternoon. The stress-strain curves for four parallels from aging time S, aging time 1 week, tensile test temperature 150°C are shown in Figure 5.4. The strength difference between the green and yellow curve is approximately 50 MPa, similar to the strength loss between 100°C and 150°C.

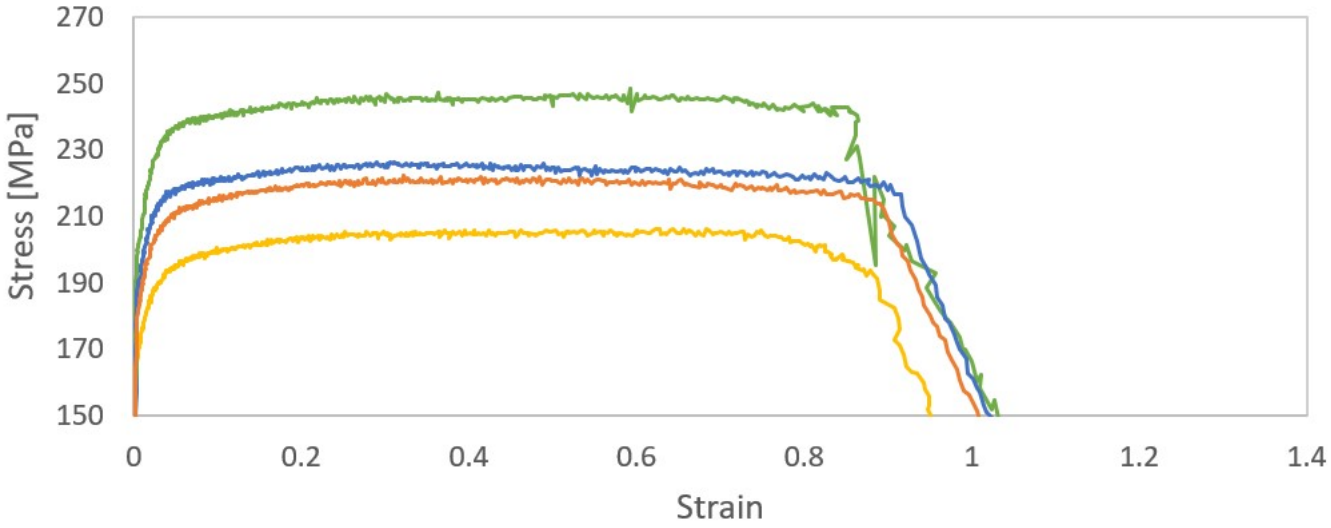

Figure 5.4: Four parallels from alloy S, aging time 1 week, tensile test temperature 150°C, when the heat chamber was not heated

The grip temperature was measured with a thermocouple, and the time before it stabilized was 2 hours for set

temperature 100°C and 2.5 hours for set temperature 150°C. However, the stabilizing temperature measured was lower than the set temperature (approximately 85°C for set temperature 100°C and 140°C for set temperature 150°C). This means that there is a possibility that the temperature increased towards the set temperature. However, the temperature increase would be very slow if that was the case.

An important lesson from the room temperature tensile test was the importance of a well-performing painted layer to avoid paint cracking during deformation. For elevated temperature tests, there was a concern that the solvent in the paint would evaporate faster at elevated temperatures, leaving the paint brittle. To limit the possibility of this, the time between painting of the specimen and the tensile test was as short as possible. The paint cracking was less of an issue than expected. The most ductile specimens experienced some cracking of the paint close to fracture. The specimens with the most severe cracking were rerun.

5.3.2 Light condition

The light condition for the tensile tests has been an important factor influencing the quality of the results. The light condition for the room temperature test varied, which in some cases complicated the analysis. The direct light should not be as strong as it was for some of the tests, so diffusive screens should be used. An alternative set up for the room temperature tests is shown in Figure 5.5.

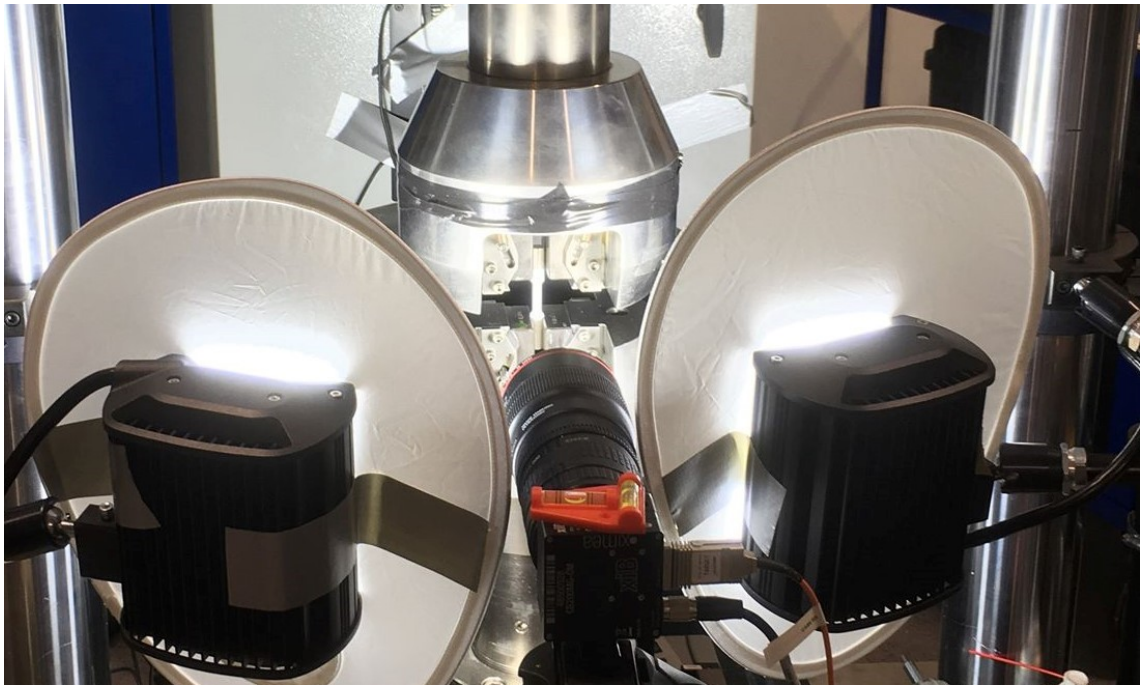

Figure 5.5: Room temperature set up with diffusive screens on the light sources.

For the elevated temperature tests, the light condition was kept approximately constant, and diffusive screens were used, which minimized these problems.

5.3.3 Diameter measurement

Both the stress and strain calculations are based on the diameter measurement, which means this is very important for the quality of the results. The diameter of the specimen was measured with a caliper with accuracy of 0.01 mm before the specimen was painted. The paint layer was measured to 0.02 mm on each side for one specimen. An additional error source in the pixel size which limits the accuracy of the contour tracking. The pixel size was approximately 0.007 mm for room temperature tests and approximately 0.01 mm.

The image rotation introduces an additional error source because the pixel size was measured before rotation. However, the rotation is very small, the largest rotation angle in radians was 0.017. This error source can be eliminated by updating the pixel size after rotation.

6 Conclusion

Based on the tensile test results, it can be concluded that alloy M has the highest tolerance to both overaging and exposure to elevated temperature. Additionally, the ductility at elevated temperatures is unexpectedly large for the strongest aging conditions for alloy M at elevated temperatures. Around the peak strength the mechanical properties of all alloys are similar, so the advantage of alloy M is that its mechanical behavior is less affected by overaging and exposure to elevated temperature.

Kocks-Mecking plots have been constructed. The slope of the linear section of the Kocks-Mecking curves has been used as a basis for suggesting a shearable transition point for the precipitates between 24 hours and 1 week.

An attempt to model the increase in dislocation density has been made, but the current model could not reveal the relative strength of the precipitates and the dislocations.

References

[1] EUROPEAN ALUMINIUM ASSOCIATION. *Automotive and transport*. 2016. URL: https://www.european-aluminium.eu/about-aluminium/aluminium-in-use/automotive-and-transport/ (visited on 06/12/2019).

[2] EUROPEAN ALUMINIUM ASSOCIATION. *Aluminium in Cars: Unlocking the lightweighting potential*. 2013. URL: https://www.european-aluminium.eu/media/1326/aluminium-in-cars-unlocking-the-lightweighting-potential.pdf (visited on 06/12/2019).

[3] C. D. Marioara et al. "The effect of Cu on precipitation in Al–Mg–Si alloys". In: *Philosophical Magazine* 87.23 (2007), pp. 3385–3413. ISSN: 1478-6435.

[4] Ø. Ryen et al. "Precipitation, strength and work hardening of age hardened aluminium alloys". In: vol. 89. 1. Institute of Physics Publishing, 2015.

[5] William F Hosford. *Mechanical behavior of materials*. eng. Cambridge, 2010.

[6] *Stress Tensor*. URL: https://docs.exabyte.io/properties-directory/non-scalar/stress-tensor/ (visited on 06/12/2019).

[7] G.E. Dieter and D. Bacon. *Mechanical Metallurgy*. Materials Science and Engineering Series. McGraw-Hill, 1988. ISBN: 9780070841871. URL: https://books.google.no/books?id=hlabmB3e8XwC.

[8] Structural database. *Intracrystalline Deformation*. URL: https://encyclopedia2.thefreedictionary.com/Dislocations (visited on 06/12/2019).

[9] William D Callister. *Materials science and engineering*. eng. Hoboken, N.J, 2015.

[10] *Orowan mechanism*. URL: https://www.giessereilexikon.com/en/foundry-lexicon/Encyclopedia/show/orowan-mechanism-4697/?cHash=1a4dc06a1dd7a00125efd4483d813126 (visited on 06/12/2019).

[11] U.F. Kocks. "Realistic constitutive relations for metal plasticity". eng. In: *Materials Science Engineering A* 317.1 (2001), pp. 181–187. ISSN: 0921-5093.

[12] Bjørn Holmedal. *Lecture notes TMT4222 Mechanical properties of materials*.

[13] The Great Soviet Encyclopedia. *Dislocations*. 1970-1979. URL: https://encyclopedia2.thefreedictionary.com/Dislocations (visited on 06/12/2019).

[14] "THE STRAIN-HARDENING FUNCTION". In: *JOURNAL OF THE INSTITUTE OF METALS* 87.1 (1958), A91–A91.

[15] Bjørn Holmedal, Erik Nes, and Knut Marthinsen. "Modelling work hardening of aluminium alloys a review of selected approaches". In: (2007).

[16] F. Roters, D. Raabe, and G. Gottstein. "Work hardening in heterogeneous alloys—a microstructural approach based on three internal state variables". eng. In: *Acta Materialia* 48.17 (2000), pp. 4181–4189. ISSN: 1359-6454.

[17] C. D. Marioara et al. “The influence of alloy composition on precipitates of the Al-Mg-Si system”. In: *Metallurgical and Materials Transactions A* 36.3 (2005), pp. 691–702. ISSN: 1543-1940. DOI: 10.1007/s11661-005-0185-1. URL: https://doi.org/10.1007/s11661-005-0185-1.

[18] Ø Ryen et al. *Precipitation strength and work hardening of age hardened aluminium alloys*.

[19] R.R. Ambriz and D. Jaramillo. *Mechanical Behavior of Precipitation Hardened Aluminum Alloys Welds*. 2013. URL: https://www.intechopen.com/books/light-metal-alloys-applications/mechanical-behavior-of-precipitation-hardened-aluminum-alloys-welds (visited on 06/12/2019).

[20] Mark L. Weaver. *Module20 Particle hardening*. 2009. URL: http://weavergroup.ua.edu/uploads/4/8/9/0/48901279/n20.pdf (visited on 06/12/2019).

[21] Bjørn Holmedal. “Strength contributions from precipitates”. eng. In: (2015). ISSN: 0950-0839. URL: http://hdl.handle.net/11250/2458536.

[22] *Aluminium handbook*. Düsseldorf: Aluminium-Verlag, 1999. ISBN: 3870172614.

[23] Matías N. Amado and Fernando Daroqui. “Revision of The Solvus Limit of Al-Mg2Si Pseudo Binary Phase Diagram”. In: *Procedia Materials Science* 8 (2015). International Congress of Science and Technology of Metallurgy and Materials, SAM - CONAMET 2013, pp. 1079 –1088. ISSN: 2211-8128. DOI: https://doi.org/10.1016/j.mspro.2015.04.171. URL: http://www.sciencedirect.com/science/article/pii/S2211812815001728.

[24] M Murayama and K Hono. “Pre-precipitate clusters and precipitation processes in Al–Mg–Si alloys”. In: *Acta Materialia* 47.5 (1999), pp. 1537 –1548. ISSN: 1359-6454. DOI: https://doi.org/10.1016/S1359-6454(99)00033-6. URL: http://www.sciencedirect.com/science/article/pii/S1359645499000336.

[25] Jonas K. Sunde et al. “The evolution of precipitate crystal structures in an Al-Mg-Si(-Cu) alloy studied by a combined HAADF-STEM and SPED approach”. In: 142.C (2018). ISSN: 1044-5803.

[26] M. Murayama et al. “The effect of Cu additions on the precipitation kinetics in an Al-Mg-Si alloy with excess Si”. eng. In: *Metallurgical and Materials Transactions A* 32.2 (2001), pp. 239–246. ISSN: 1073-5623.

[27] Jonas Sunde.

[28] L. Cheng et al. “The influence of precipitation on the work-hardening behavior of the aluminum alloys AA6111 and AA7030”. eng. In: *Metallurgical and Materials Transactions A* 34.11 (2003), pp. 2473–2481. ISSN: 1073-5623.

[29] U.F Kocks. *Thermodynamics and kinetics of slip*. eng. Oxford ; New York, 1975.

[30] F. Lu, T Manik, and B Holmedal. *Work-hardening behaviour of AA6082 with different aging times*. 2018.

[31] *Tensile testing*. eng. Materials Park, Ohio, 2004.

[32] P. W. Bridgman. *Studies in large plastic flow and fracture with special emphasis on the effects on hydrostatic pressure*. Ed. by Robert F. Mehl. McGraw-Hill book company, 1952.

[33] Magdalena Gromada. *Correction Formulae for the Stress Distribution in Round Tensile Specimens at Neck Presence*. eng. Berlin, Heidelberg, 2011.

[34] Tomás Mánic, Feng Lu, and Bjørn Holmedal. "The analytical post-necking correction of stress in axisymmetric tensile specimen with fiber texture". In: 2018.

[35] G. Le Roy et al. "A model of ductile fracture based on the nucleation and growth of voids". In: *Acta Metallurgica* 29.8 (1981), pp. 1509 –1522. ISSN: 0001-6160. DOI: https://doi.org/10.1016/0001-6160(81)90185-1. URL: http://www.sciencedirect.com/science/article/pii/0001616081901851.

[36] T Khelfa et al. "Microstructure and strengthening mechanisms in an Al-Mg-Si alloy processed by equal channel angular pressing (ECAP)". In: *The International Journal of Advanced Manufacturing Technology* (Nov. 2017). DOI: 10.1007/s00170-017-1310-1.

[37] K. Pedersen et al. *Material properties and grain structure in 6082 with different alloying additions*. 2017.

A Stress-strain curves

A.1 Alloy S

All stress-strain curves are presented below. In each figure, all results for one alloy and aging condition are presented.

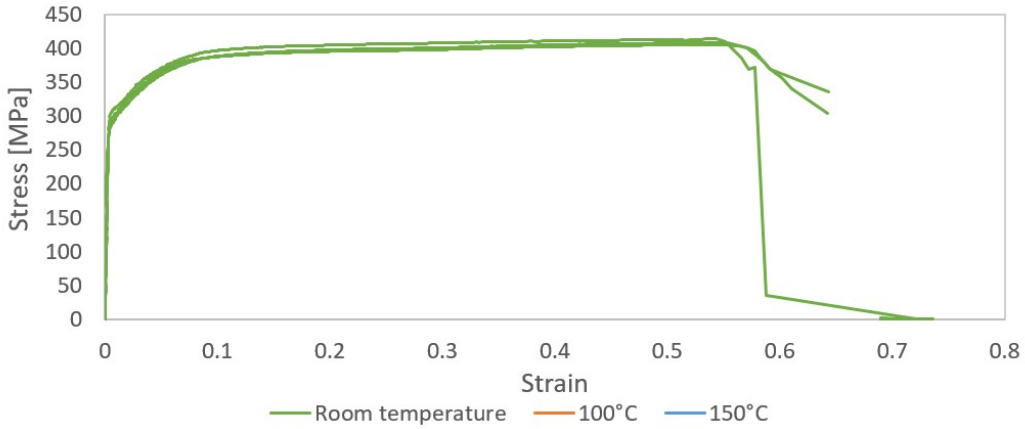

Figure A.1: Stress-strain curves for alloy S, aging time 20 minutes

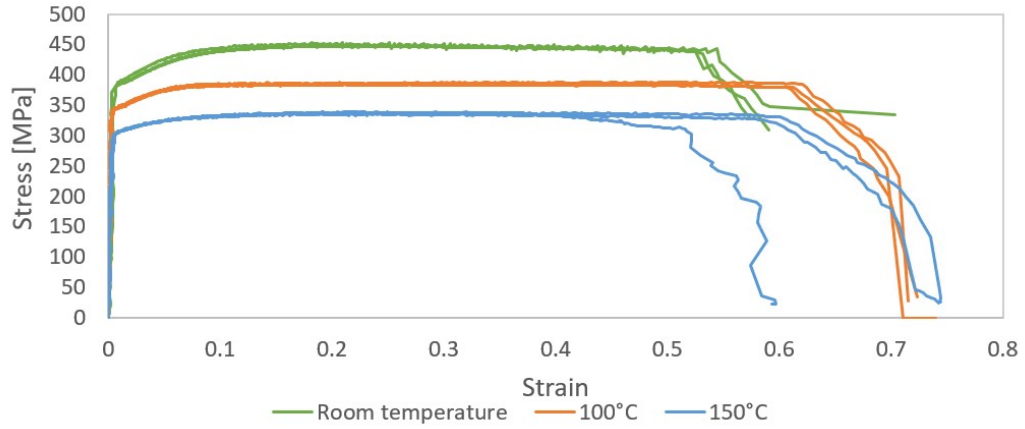

Figure A.2: Stress-strain curves for alloy S, aging time 1 hour

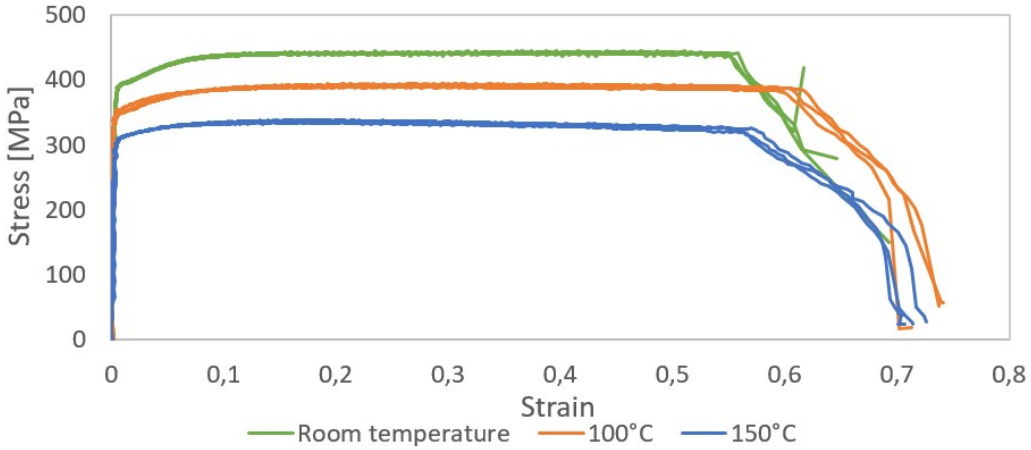

Figure A.3: Stress-strain curves for alloy S, aging time 3 hours

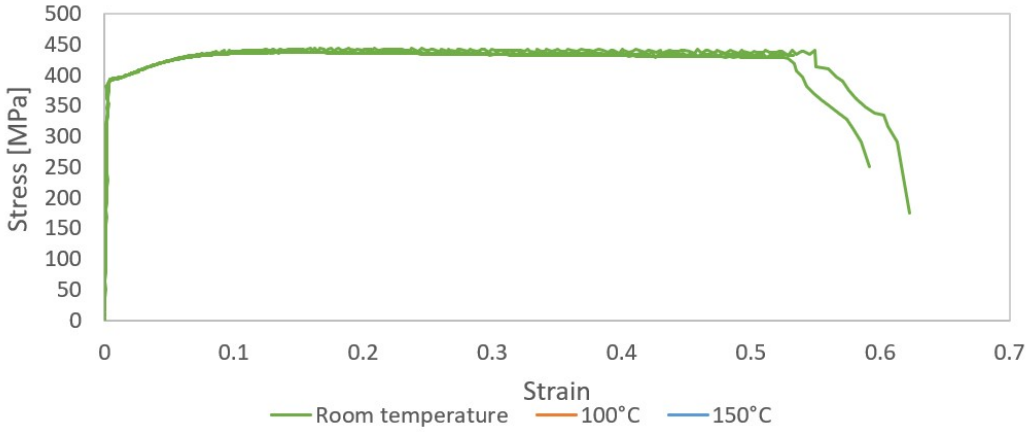

Figure A.4: Stress-strain curves for alloy S, aging time 5 hours

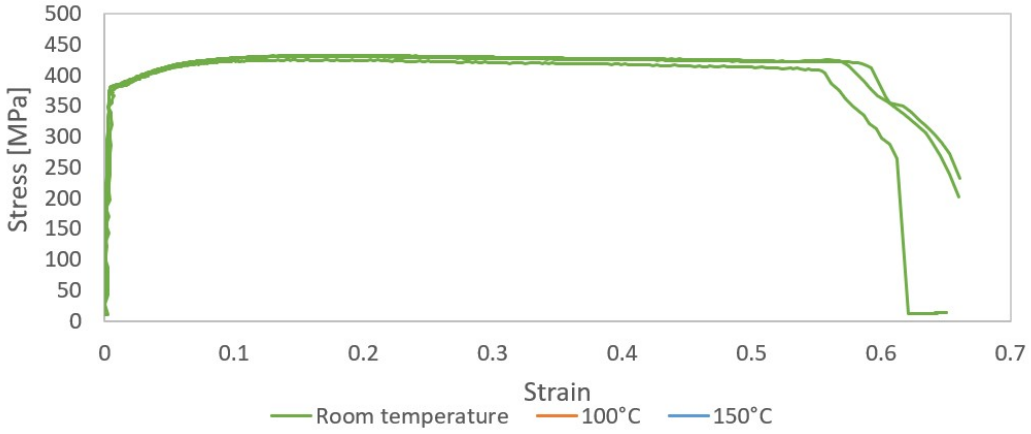

Figure A.5: Stress-strain curves for alloy S, aging time 12 hours

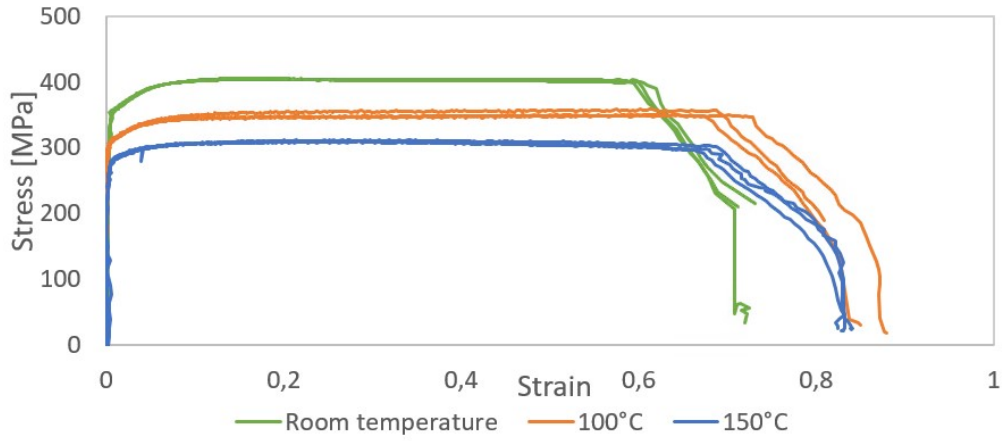

Figure A.6: Stress-strain curves for alloy S, aging time 24 hours

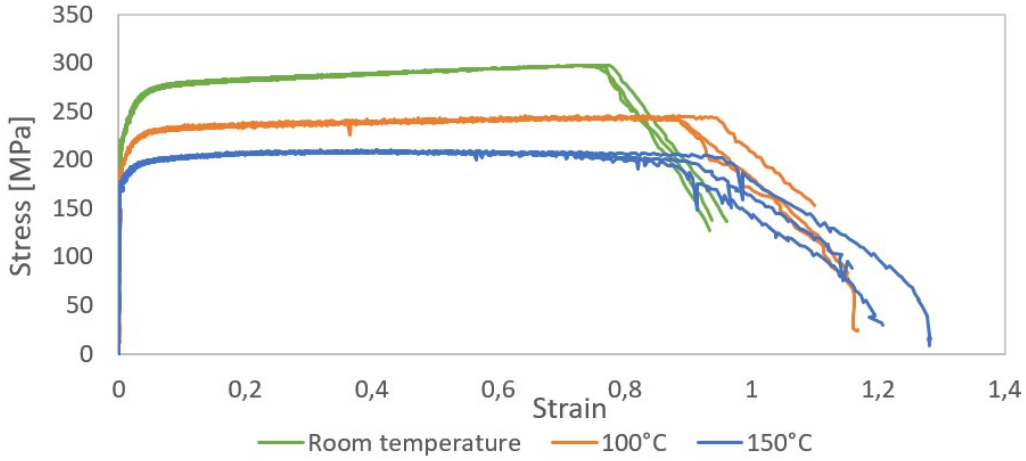

Figure A.7: Stress-strain curves for alloy S, aging time 1 week

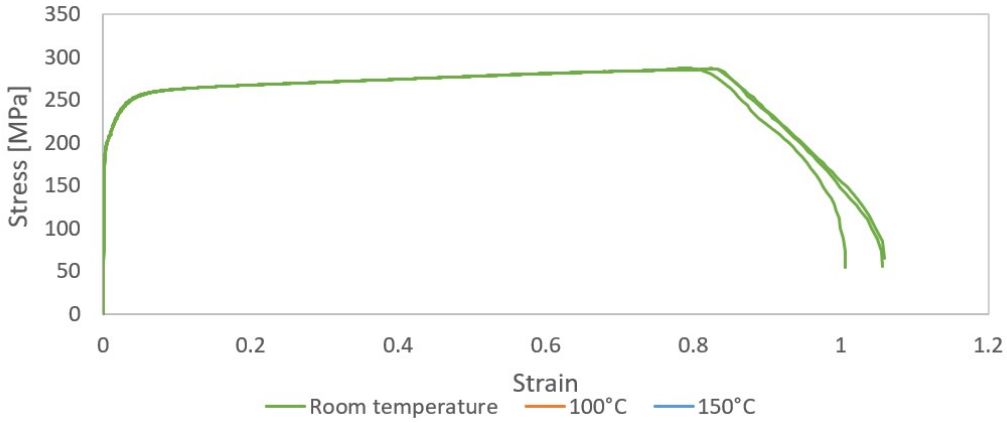

Figure A.8: Stress-strain curves for alloy S, aging time 2 weeks

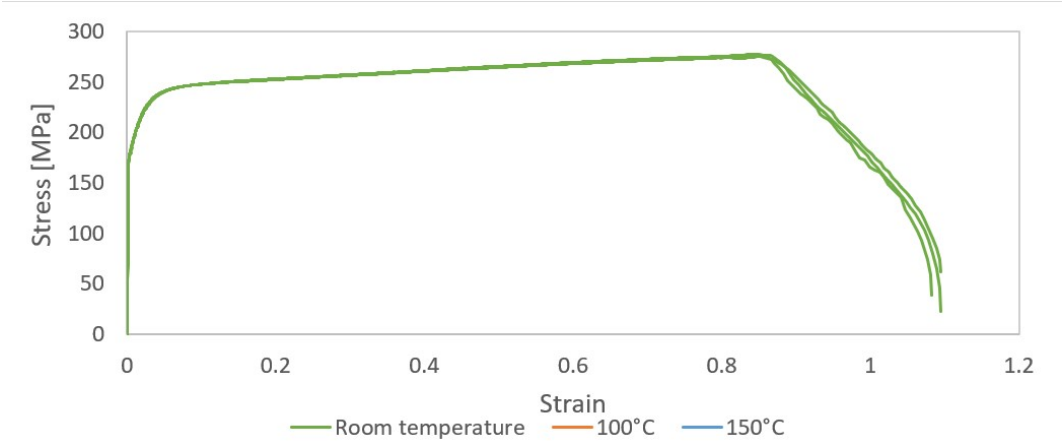

Figure A.9: Stress-strain curves for alloy S, aging time 1 month

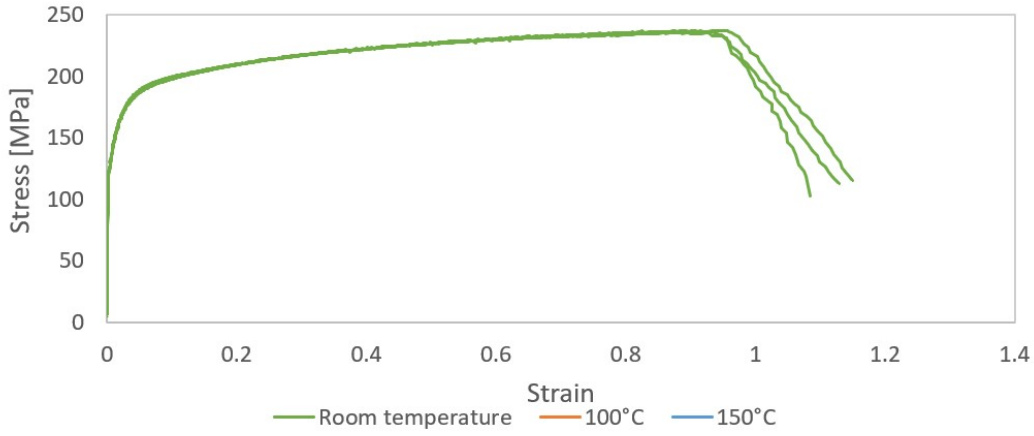

Figure A.10: Stress-strain curves for alloy S, aging time 24 hours at 250°C

A.2 Alloy C

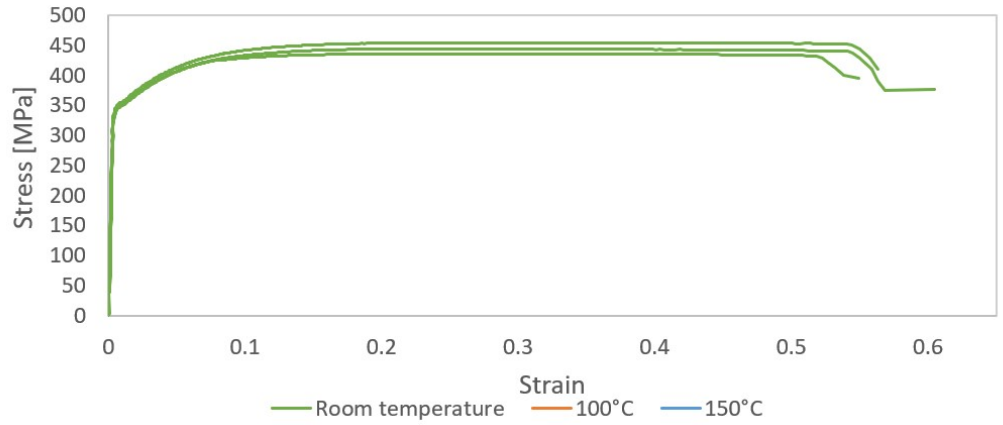

Figure A.11: Stress-strain curves for alloy C, aging time 20 minutes

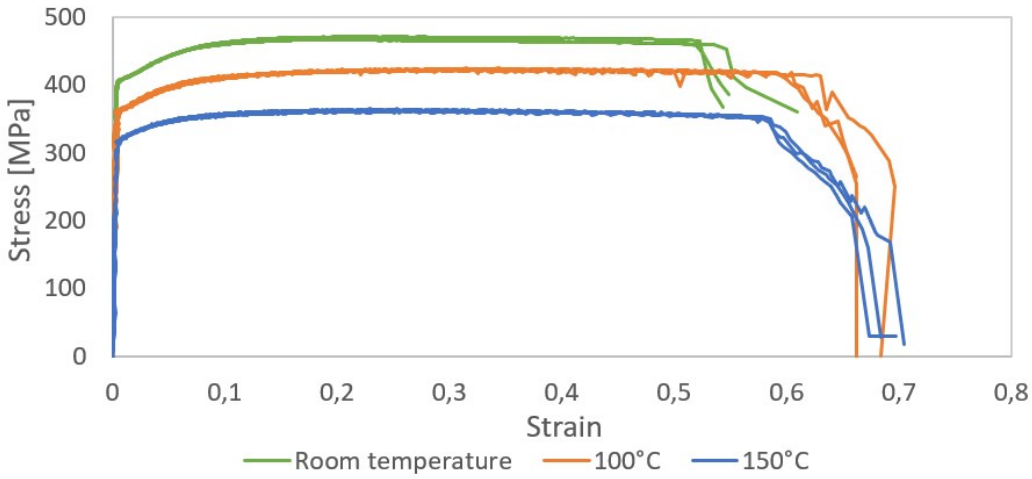

Figure A.12: Stress-strain curves for alloy C, aging time 1 hour

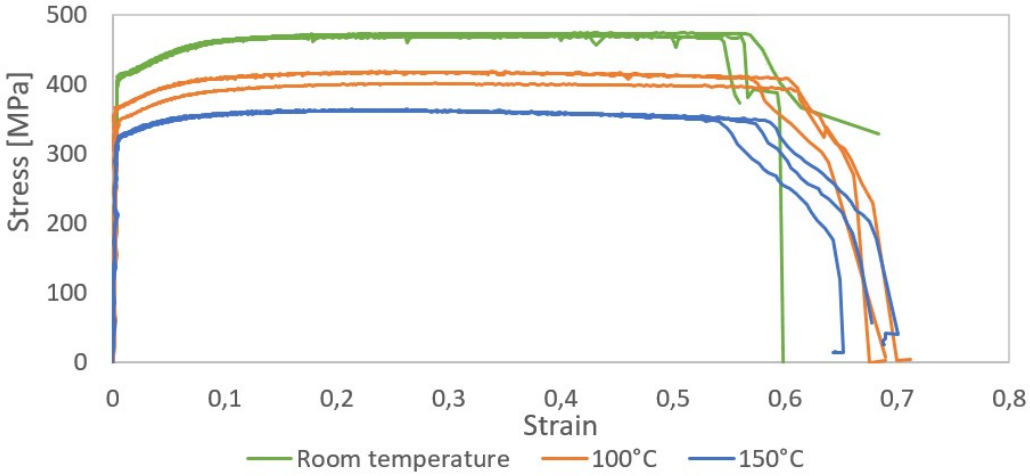

Figure A.13: Stress-strain curves for alloy C, aging time 3 hours

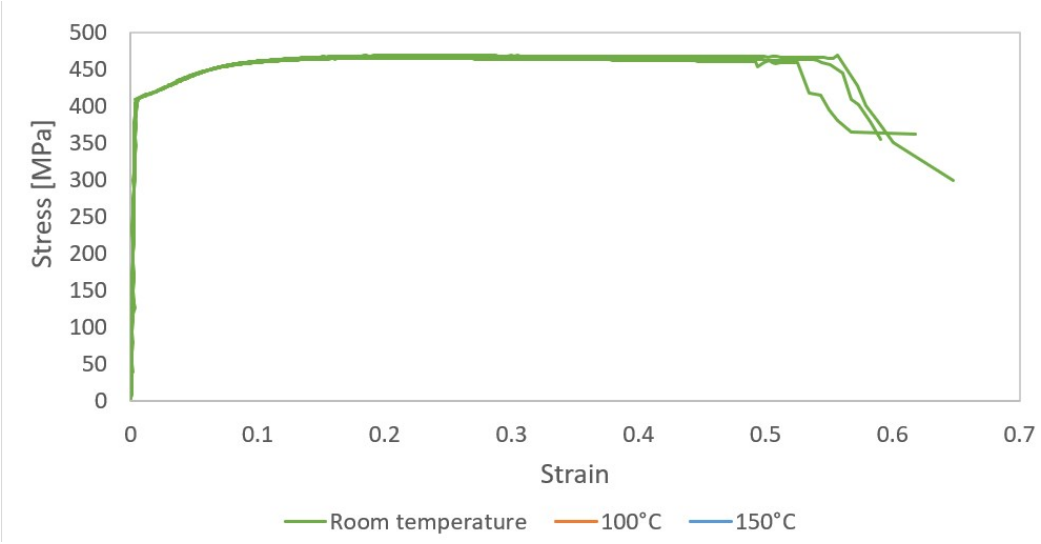

Figure A.14: Stress-strain curves for alloy C, aging time 5 hours

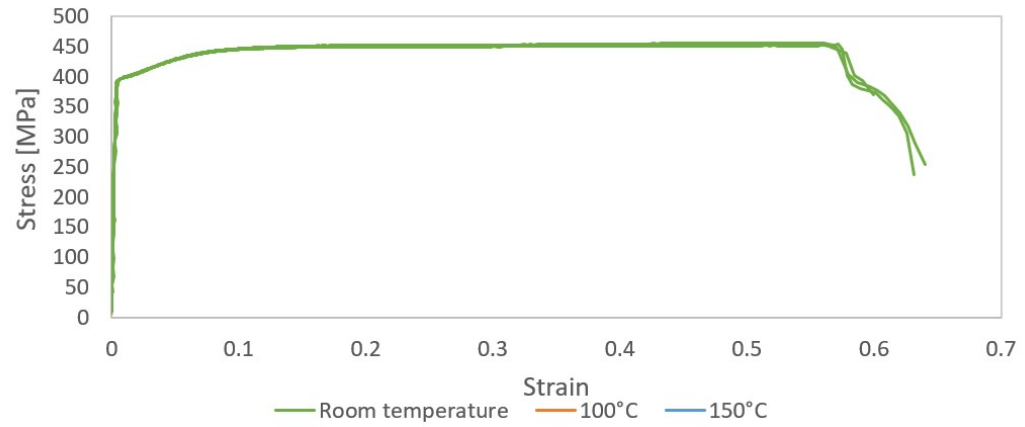

Figure A.15: Stress-strain curves for alloy C, aging time 12 hours

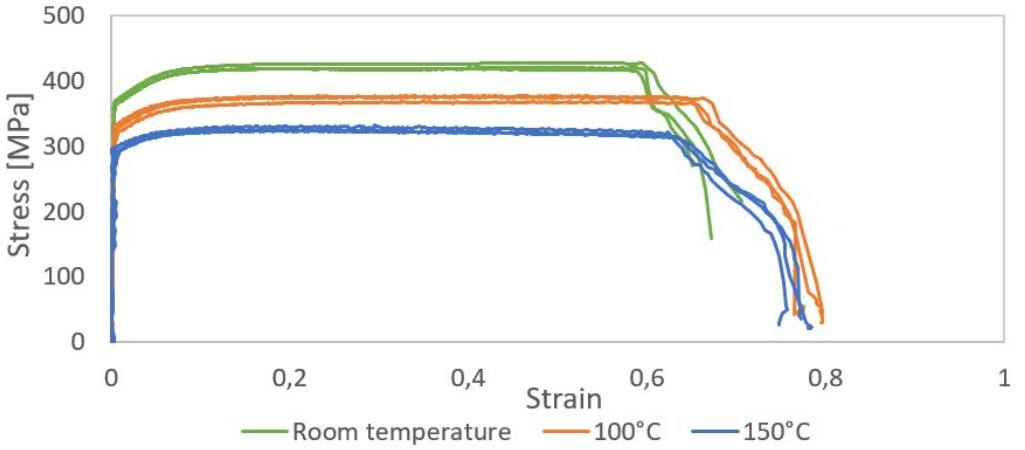

Figure A.16: Stress-strain curves for alloy C, aging time 24 hours

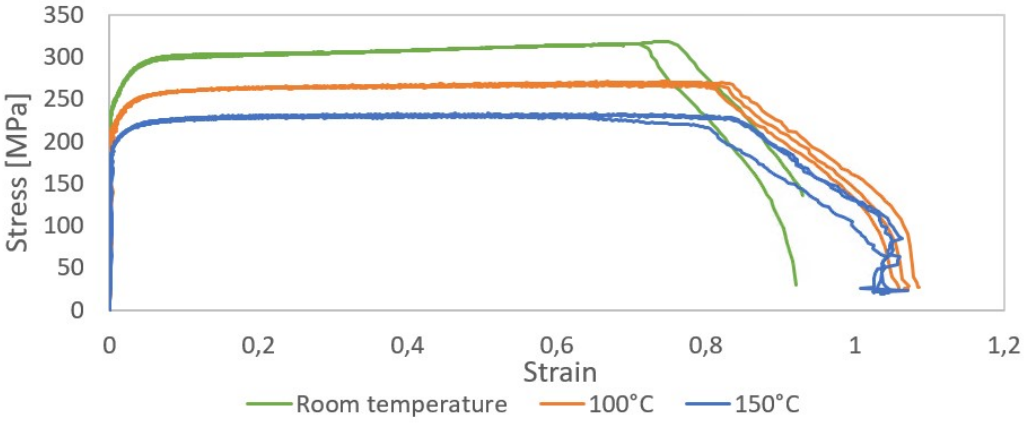

Figure A.17: Stress-strain curves for alloy C, aging time 1 week

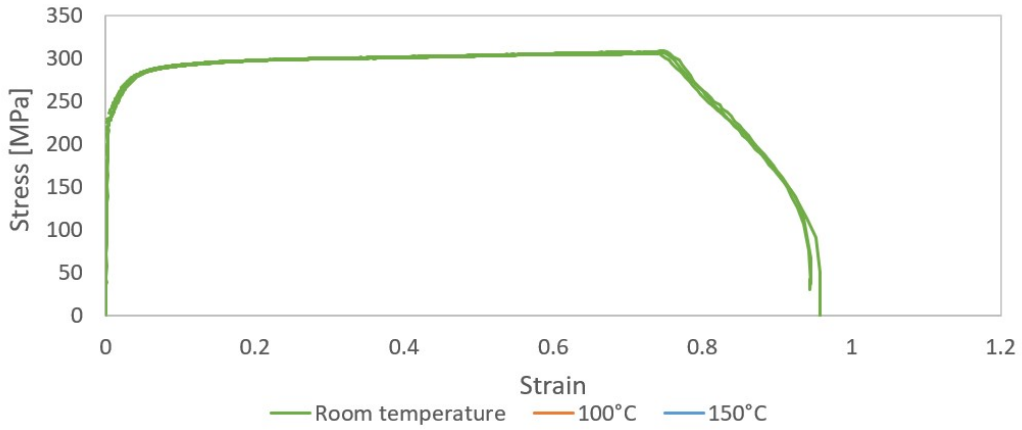

Figure A.18: Stress-strain curves for alloy C, aging time 2 week

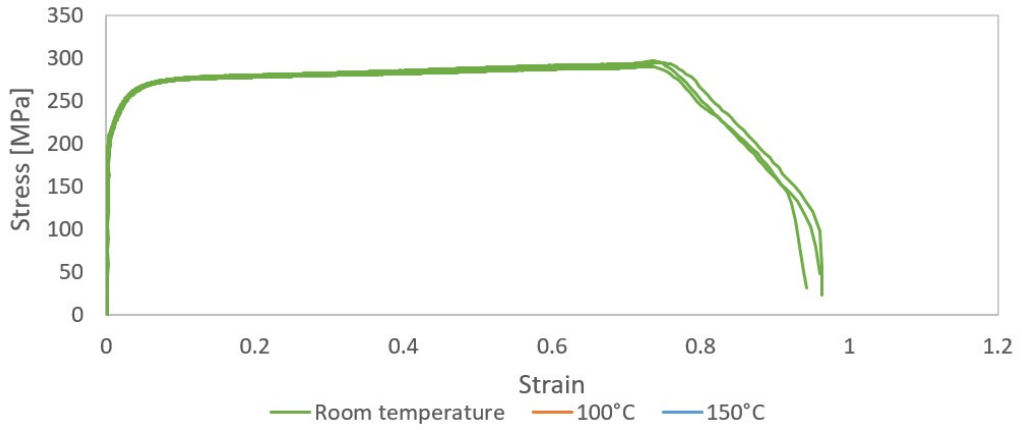

Figure A.19: Stress-strain curves for alloy C, aging time 1 month

A.3 Alloy M

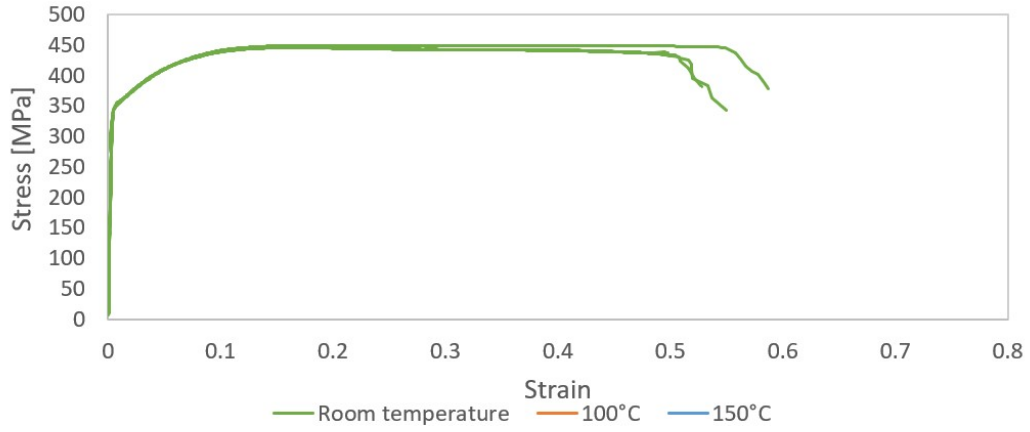

Figure A.20: Stress-strain curves for alloy M, aging time 20 minutes

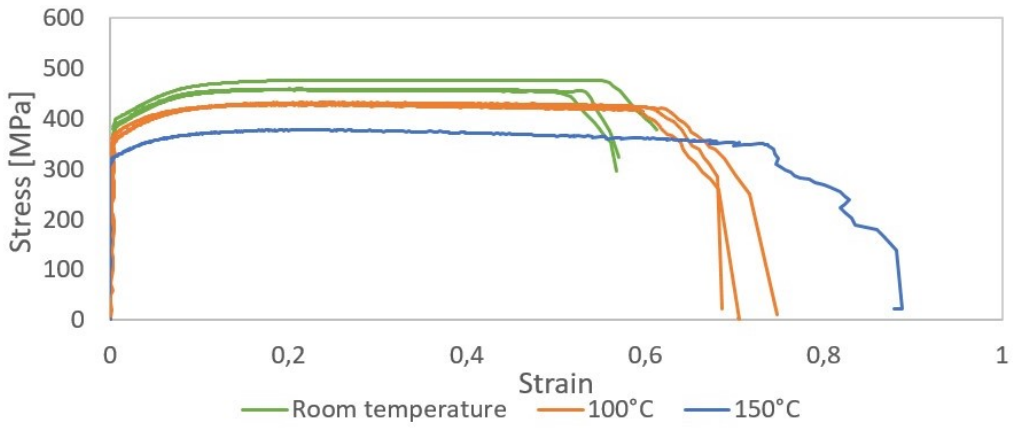

Figure A.21: Stress-strain curves for alloy M, aging time 1 hour

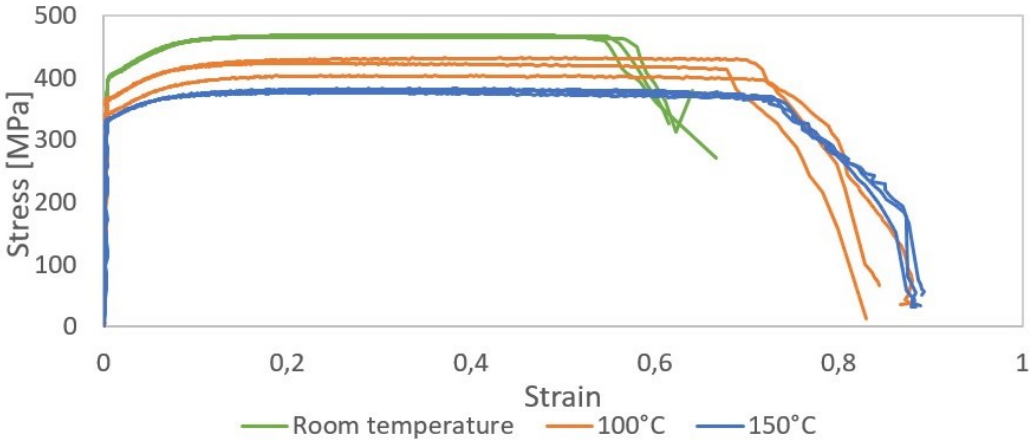

Figure A.22: Stress-strain curves for alloy S, aging time 3 hours

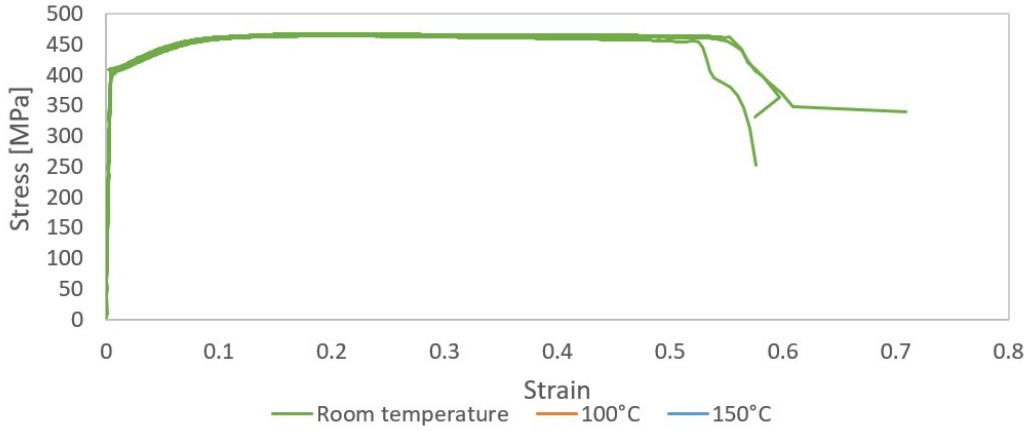

Figure A.23: Stress-strain curves for alloy M, aging time 5 hours

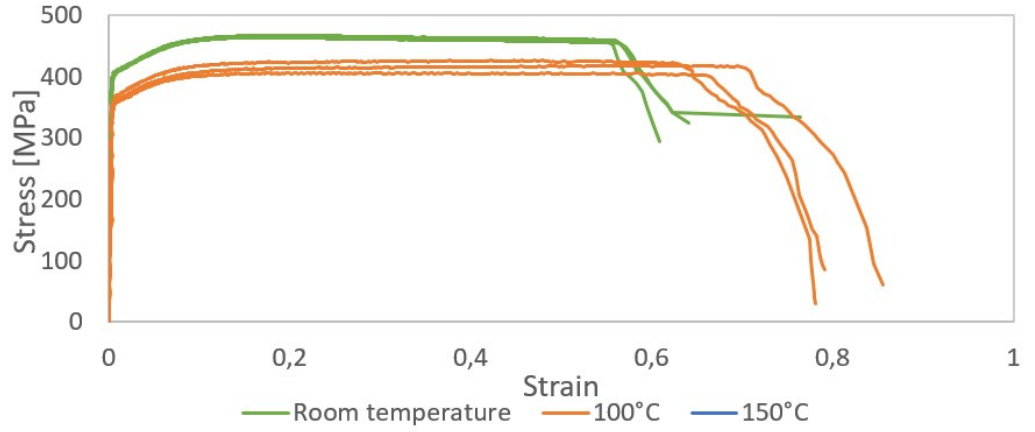

Figure A.24: Stress-strain curves for alloy M, aging time 12 hours

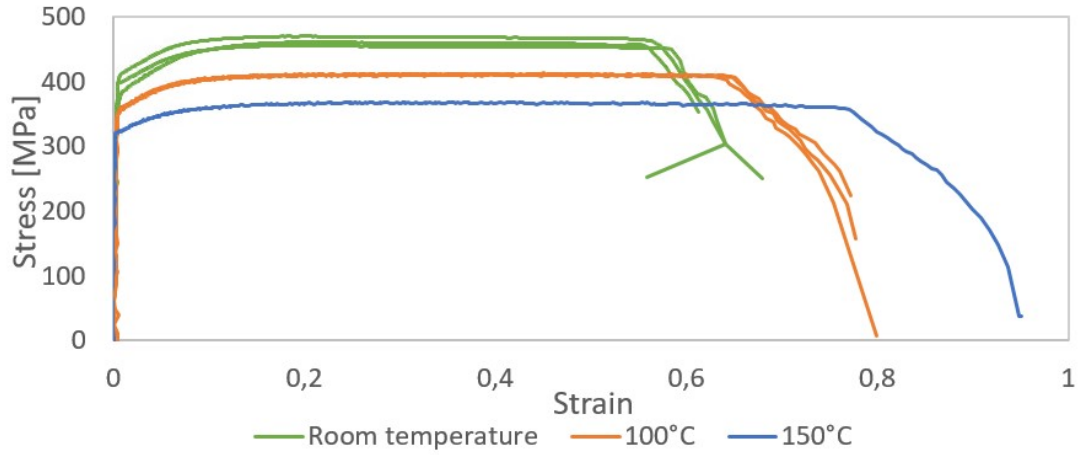

Figure A.25: Stress-strain curves for alloy M, aging time 24 hours

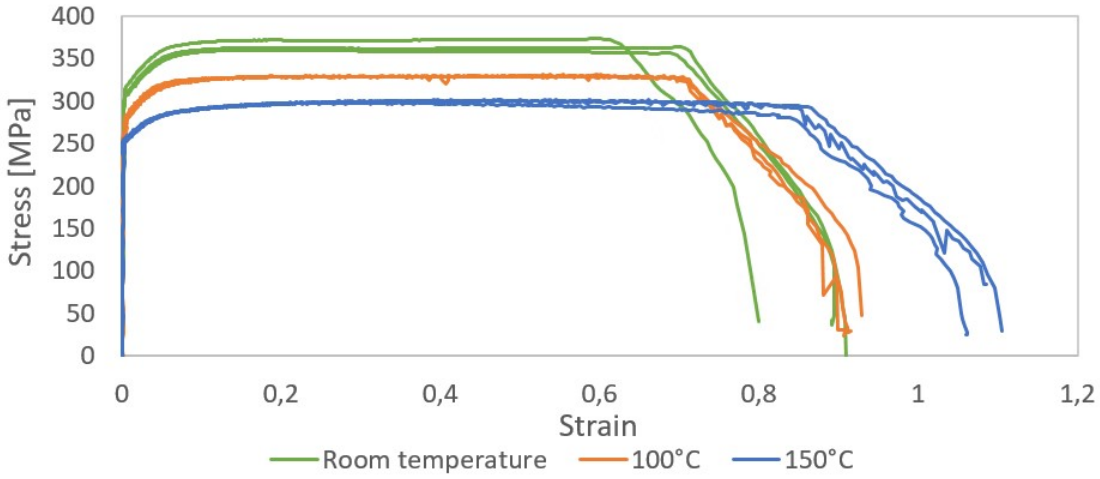

Figure A.26: Stress-strain curves for alloy M, aging time 1 week

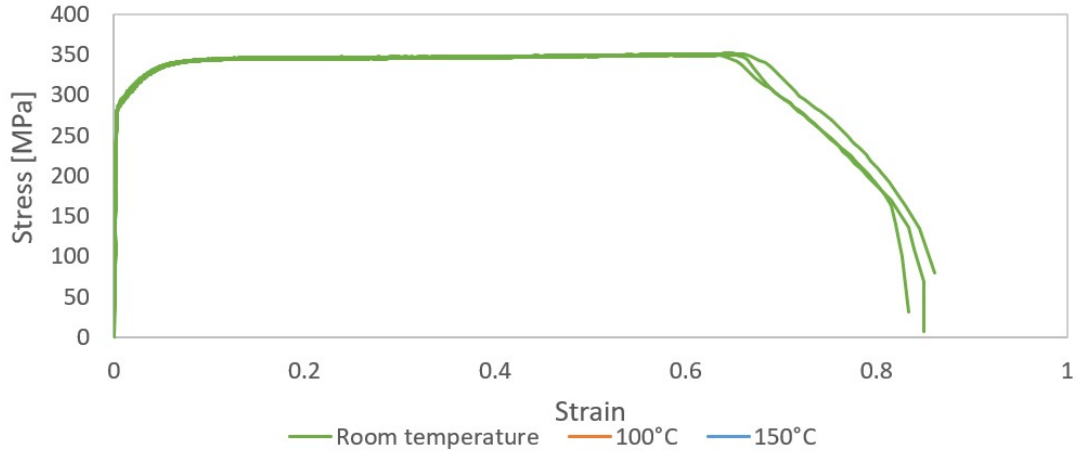

Figure A.27: Stress-strain curves for alloy M, aging time 2 weeks

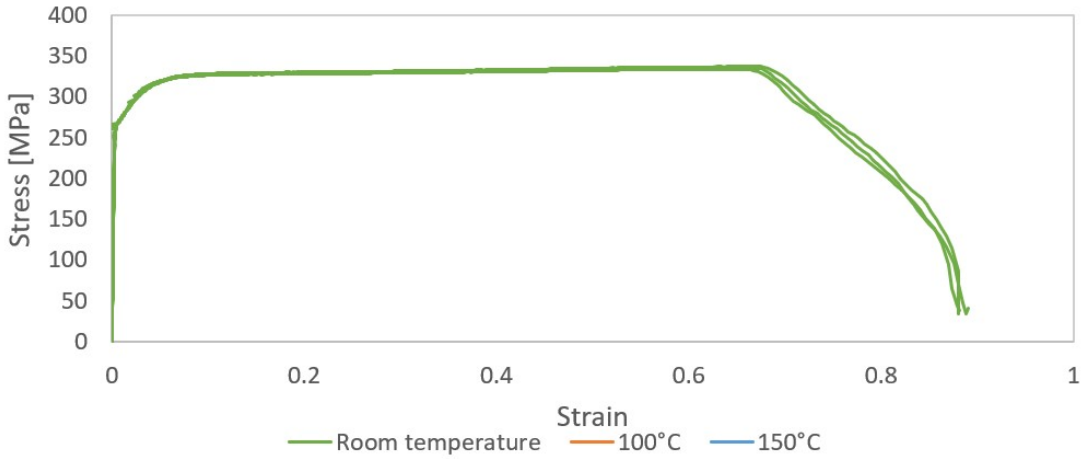

Figure A.28: Stress-strain curves for alloy M, aging time 1 month

B Kocks-Mecking curves

B.1 Alloy S

All Kocks-Mecking curves are presented below. In each figure, all results for one alloy and aging condition are presented.

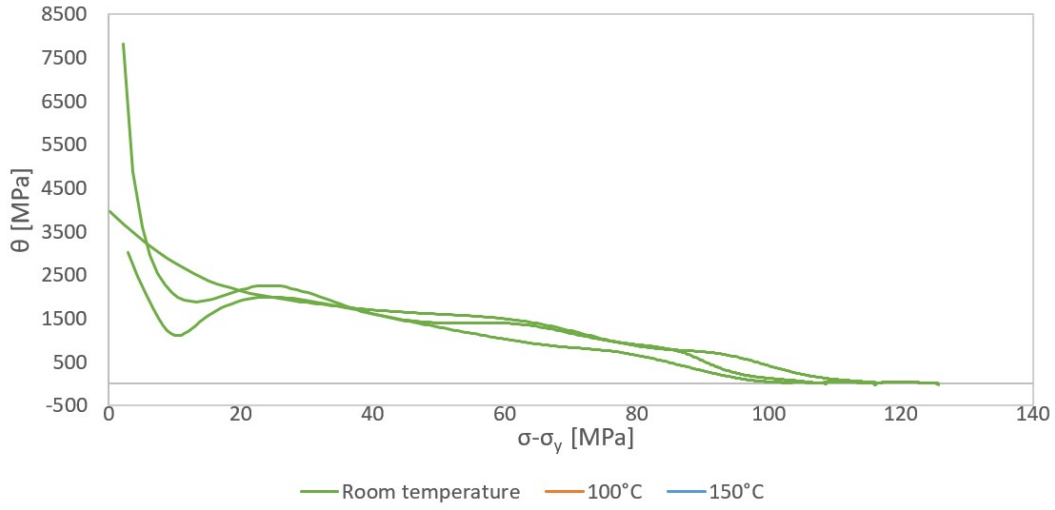

Figure B.1: Kocks-Mecking curves for alloy S, aging time 20 minutes

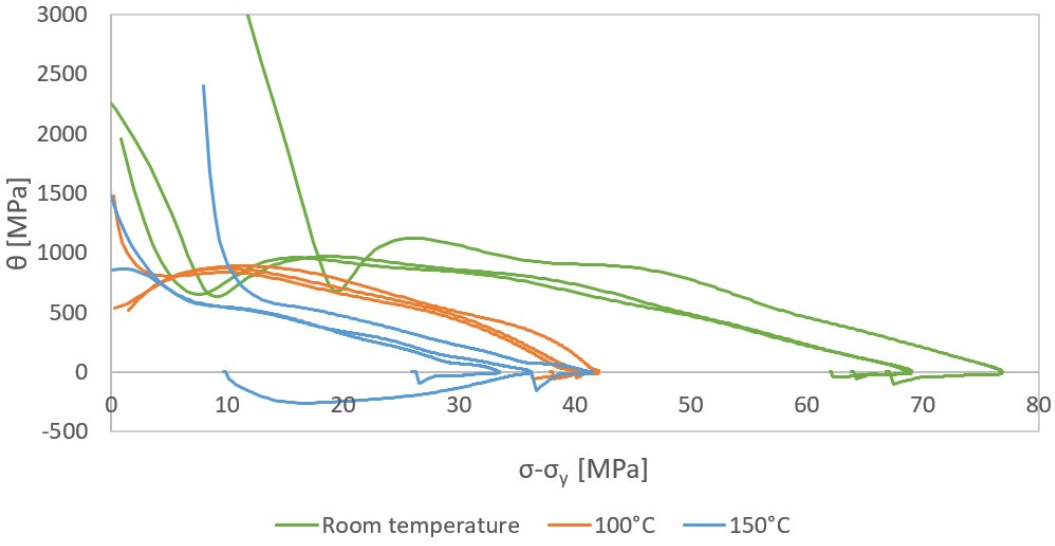

Figure B.2: Kocks-Mecking curves for alloy S, aging time 1 hour

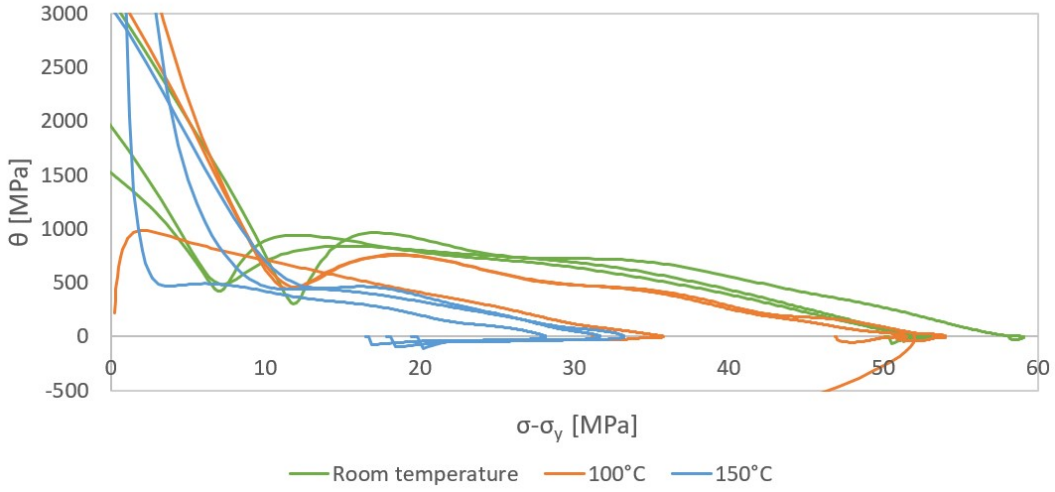

Figure B.3: Kocks-Mecking curves for alloy S, aging time 3 hours

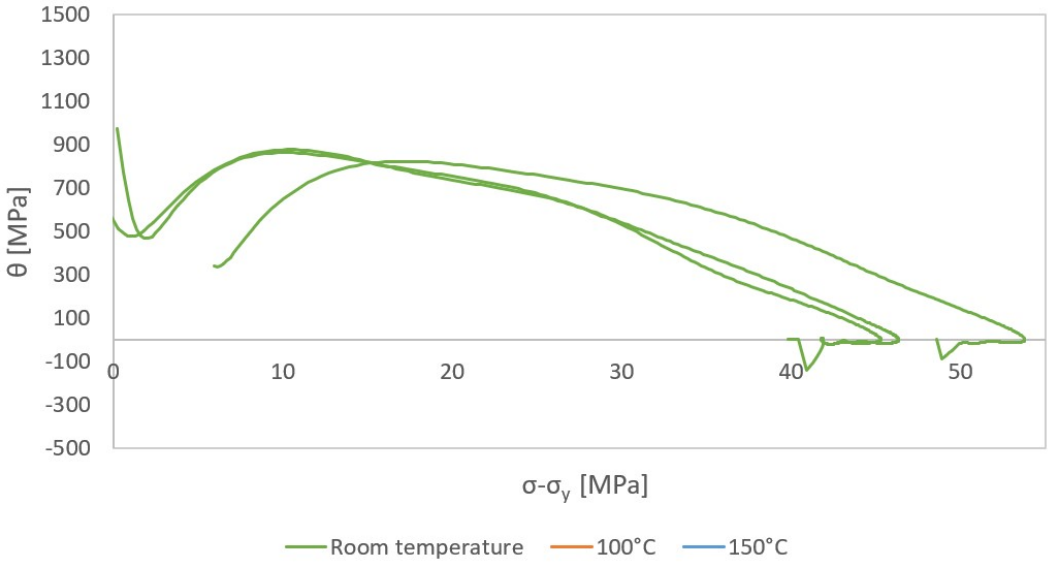

Figure B.4: Kocks-Mecking curves for alloy S, aging time 5 hours

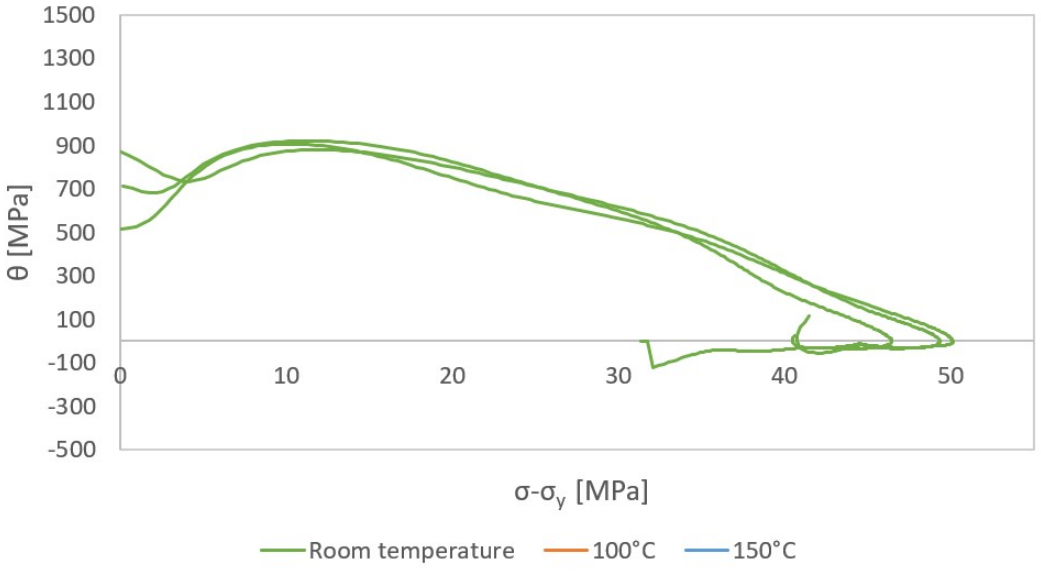

Figure B.5: Kocks-Mecking curves for alloy S, aging time 12 hours

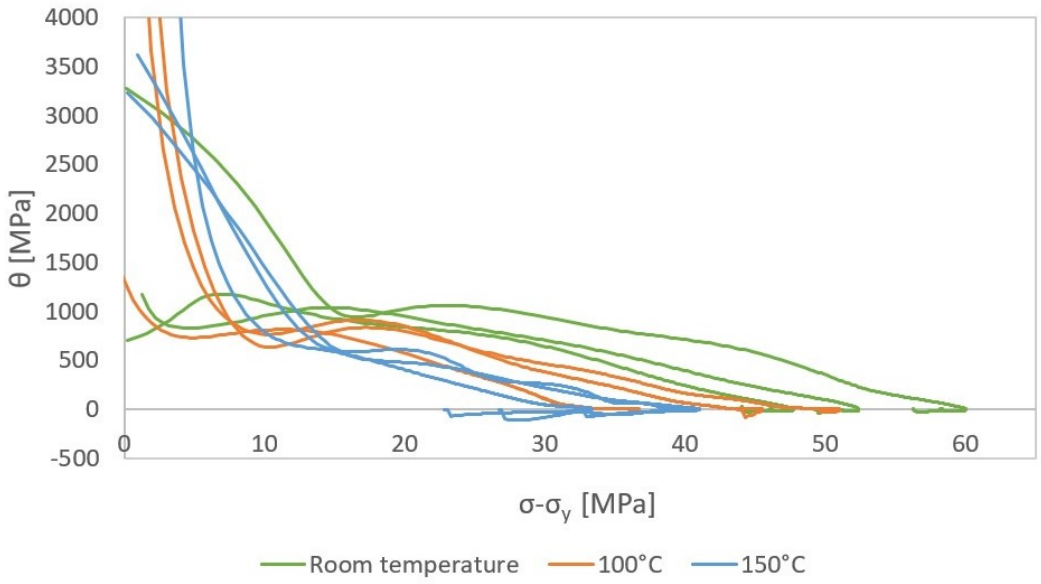

Figure B.6: Kocks-Mecking curves for alloy S, aging time 24 hours

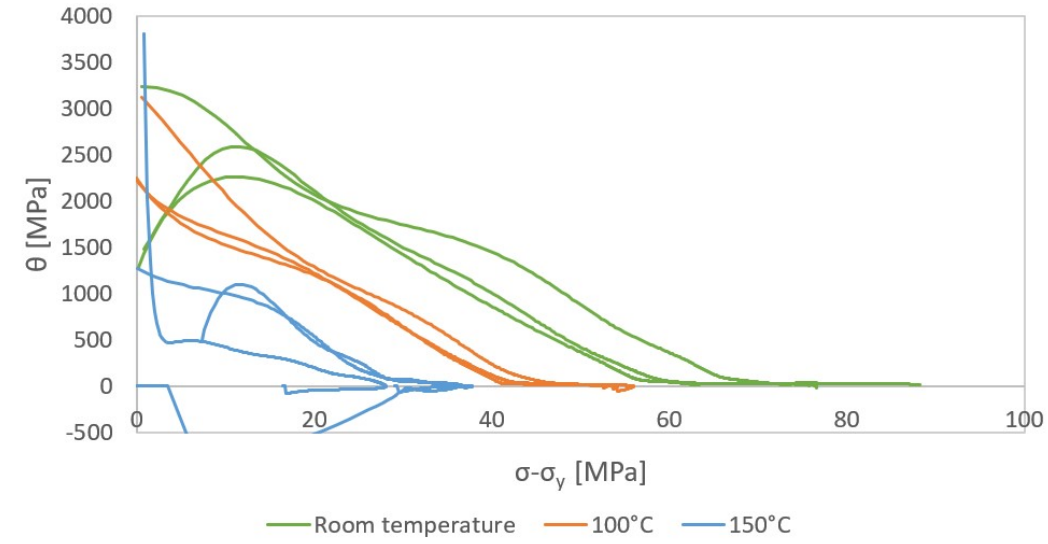

Figure B.7: Kocks-Mecking curves for alloy S, aging time 1 week

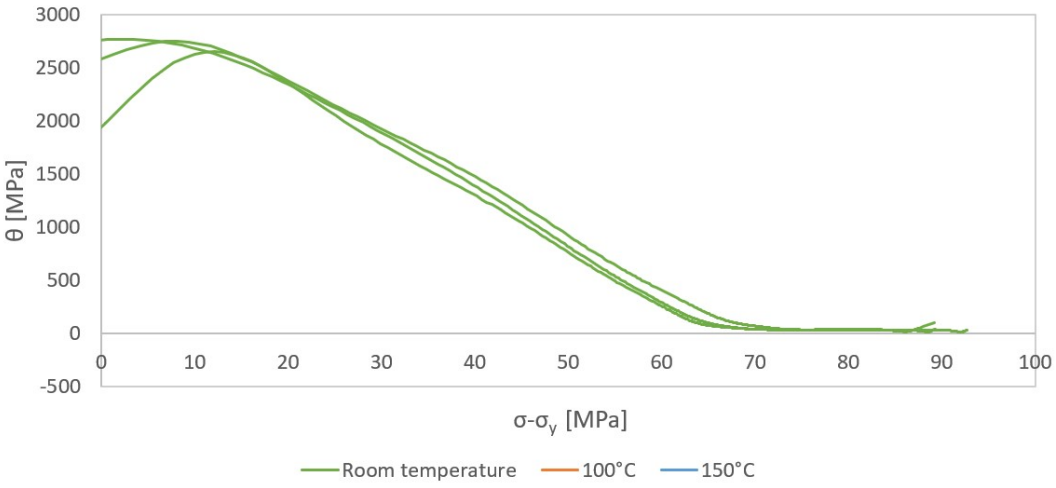

Figure B.8: Kocks-Mecking curves for alloy S, aging time 2 weeks

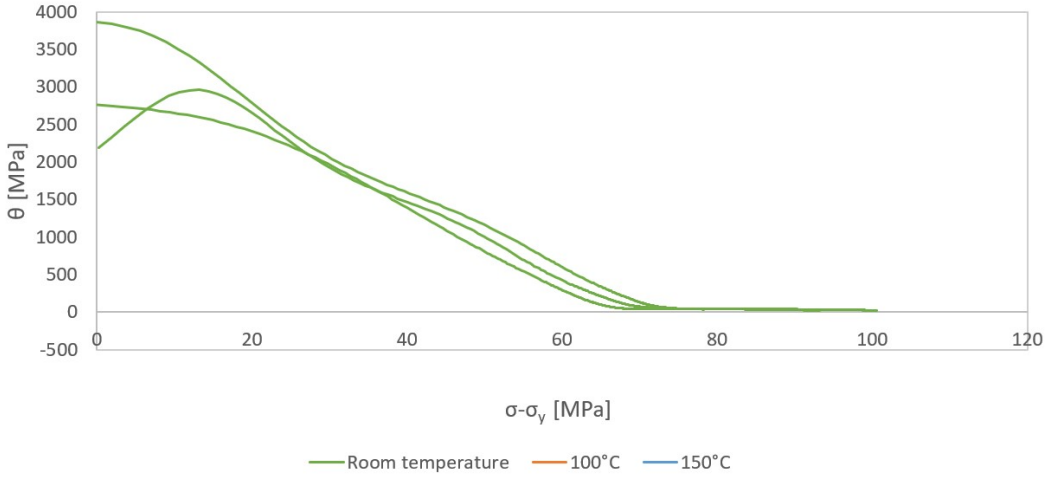

Figure B.9: Kocks-Mecking curves for alloy S, aging time 1 month

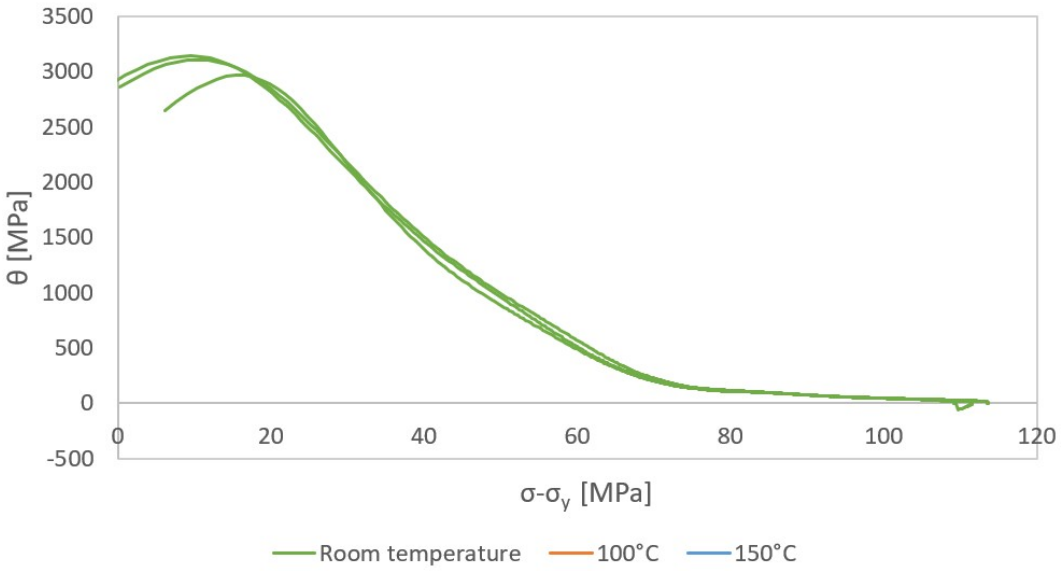

Figure B.10: Kocks-Mecking curves for alloy S, aging time 24 hours at 250°C

B.2 Alloy C

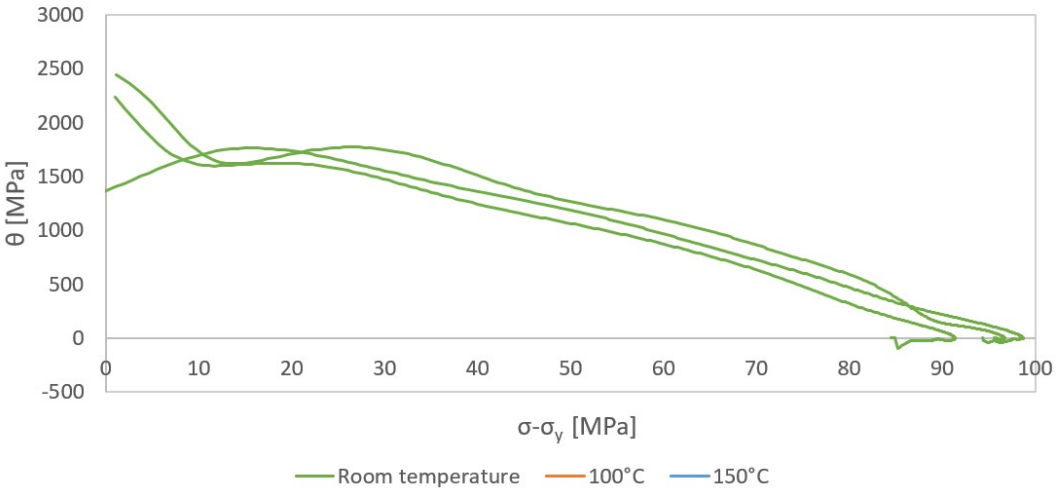

Figure B.11: Kocks-Mecking curves for alloy C, aging time 20 minutes

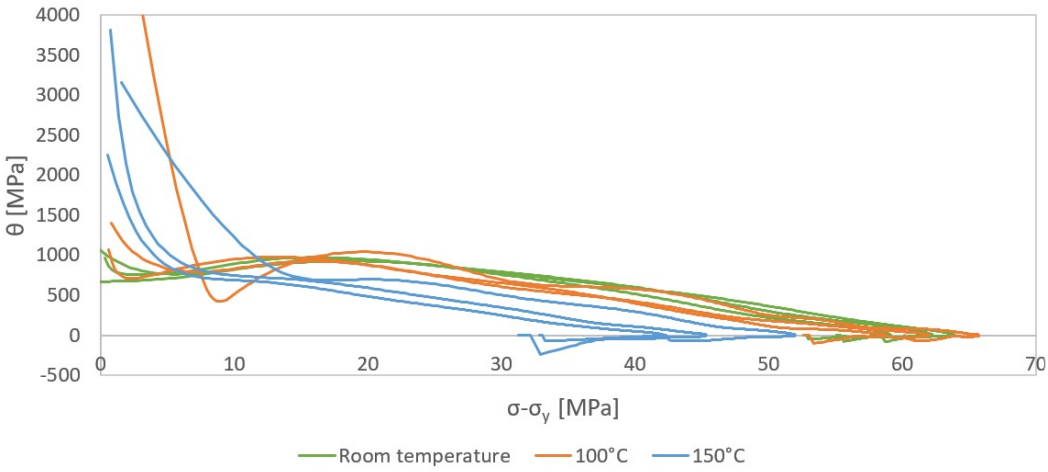

Figure B.12: Kocks-Mecking curves for alloy C, aging time 1 hour

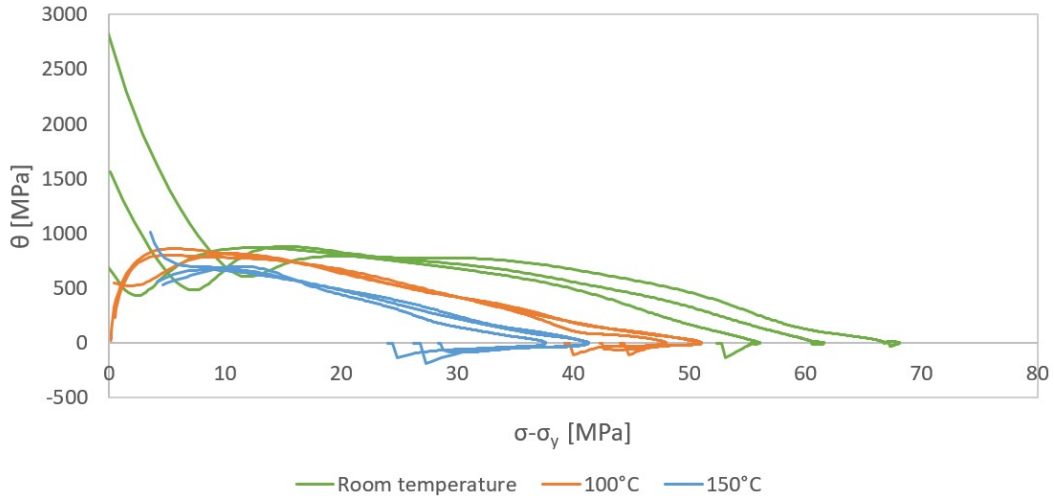

Figure B.13: Kocks-Mecking curves for alloy C, aging time 3 hours

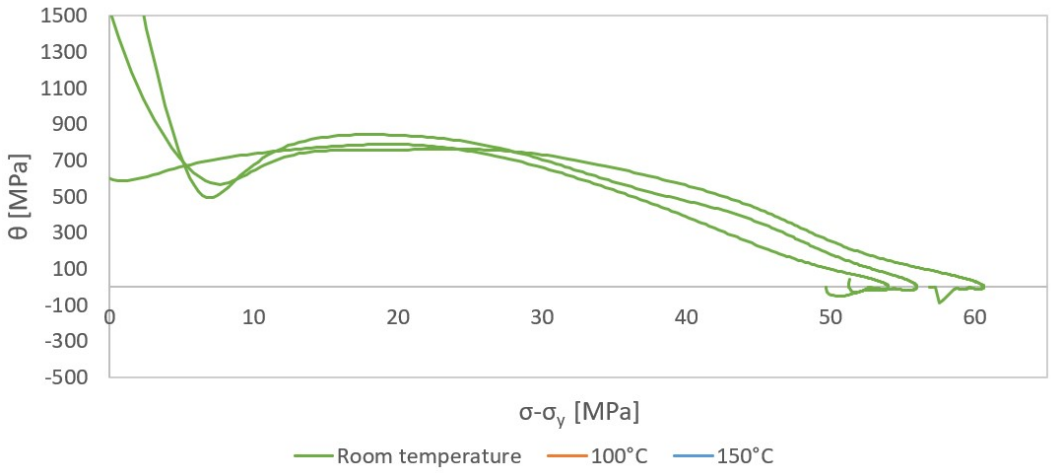

Figure B.14: Kocks-Mecking curves for alloy C, aging time 5 hours

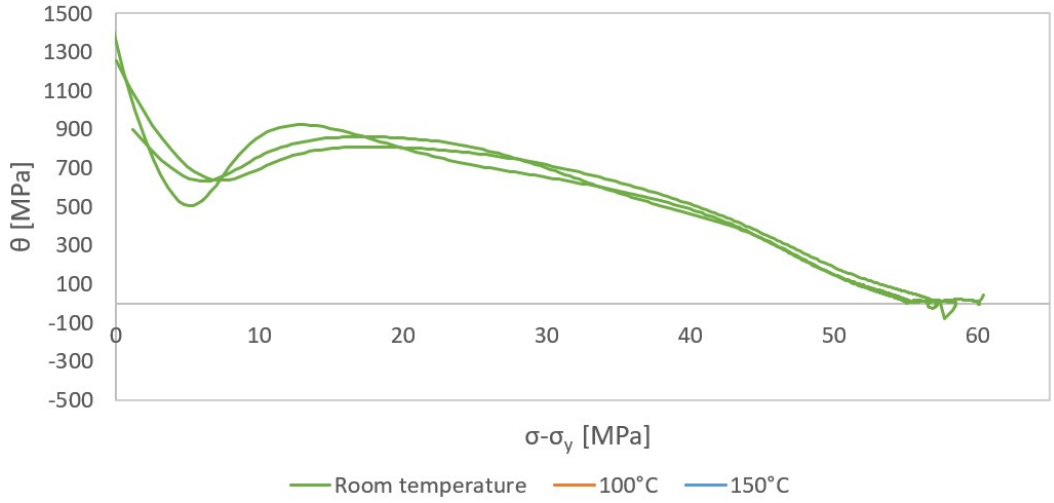

Figure B.15: Kocks-Mecking curves for alloy C, aging time 12 hours

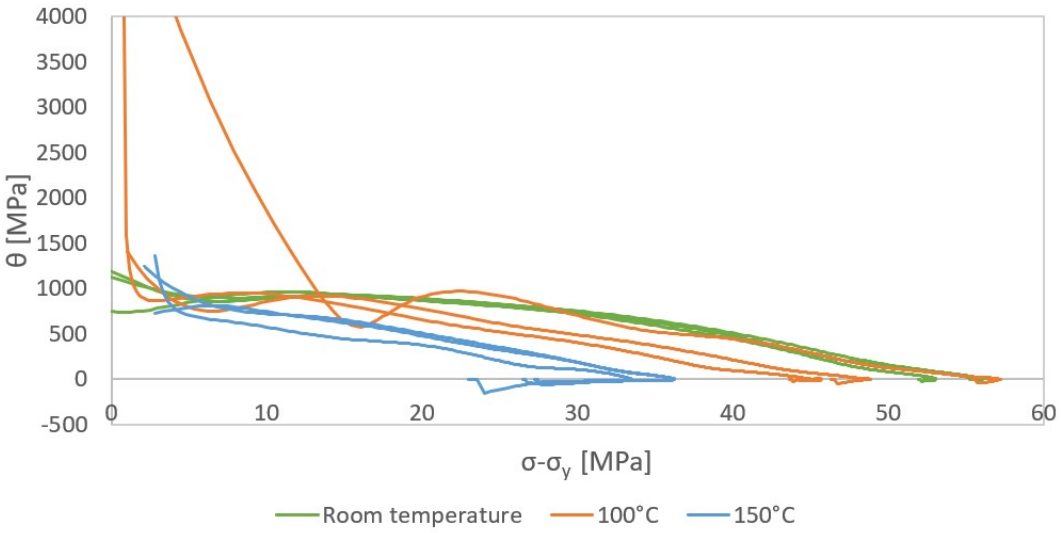

Figure B.16: Kocks-Mecking curves for alloy C, aging time 24 hours

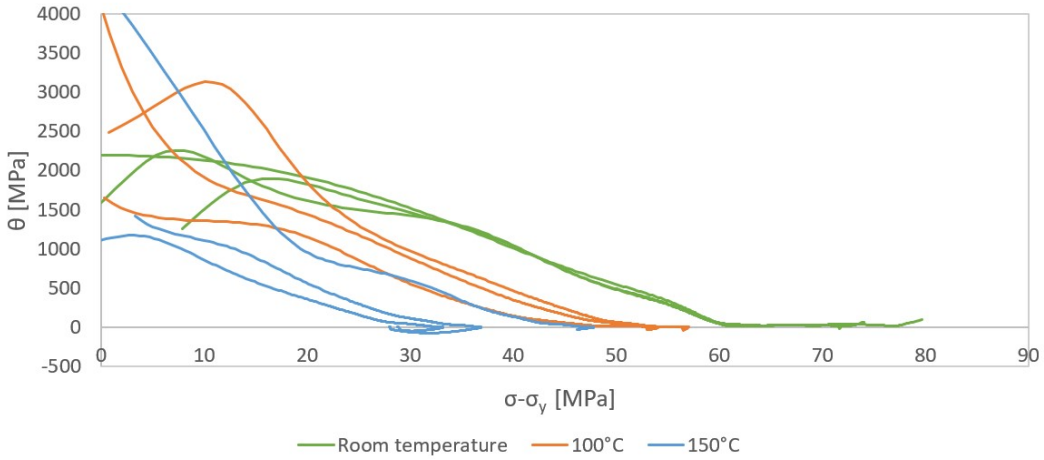

Figure B.17: Kocks-Mecking curves for alloy C, aging time 1 week

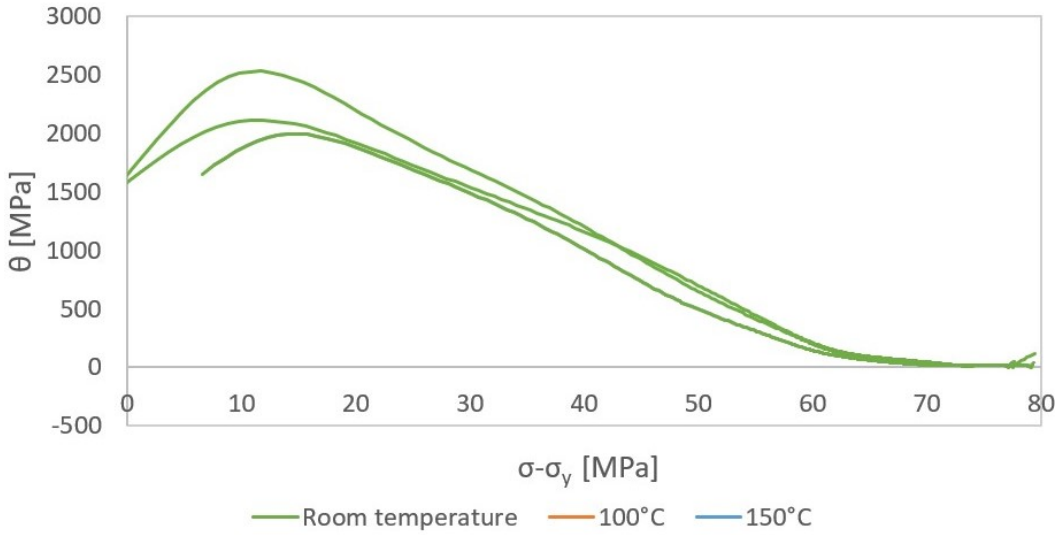

Figure B.18: Kocks-Mecking curves for alloy C, aging time 2 week

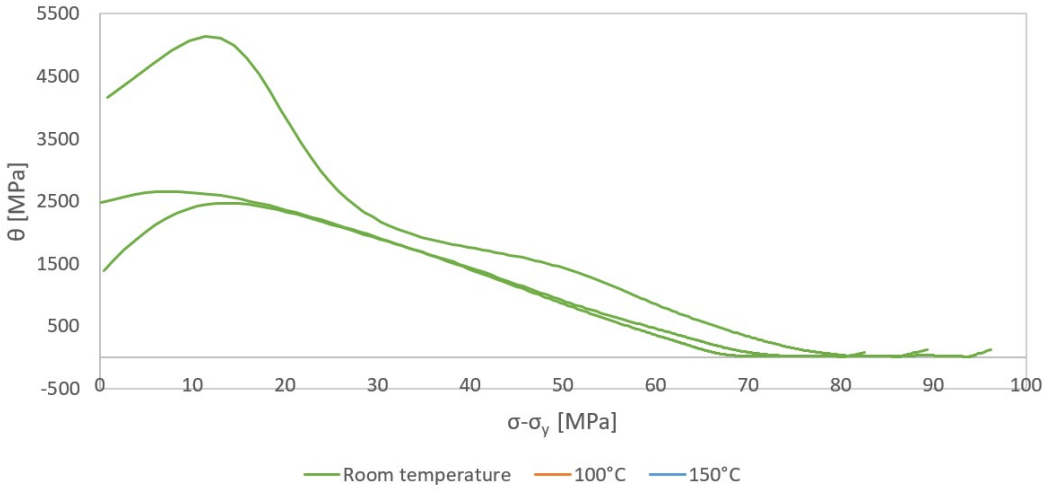

Figure B.19: Kocks-Mecking curves for alloy C, aging time 1 month

B.3 Alloy M

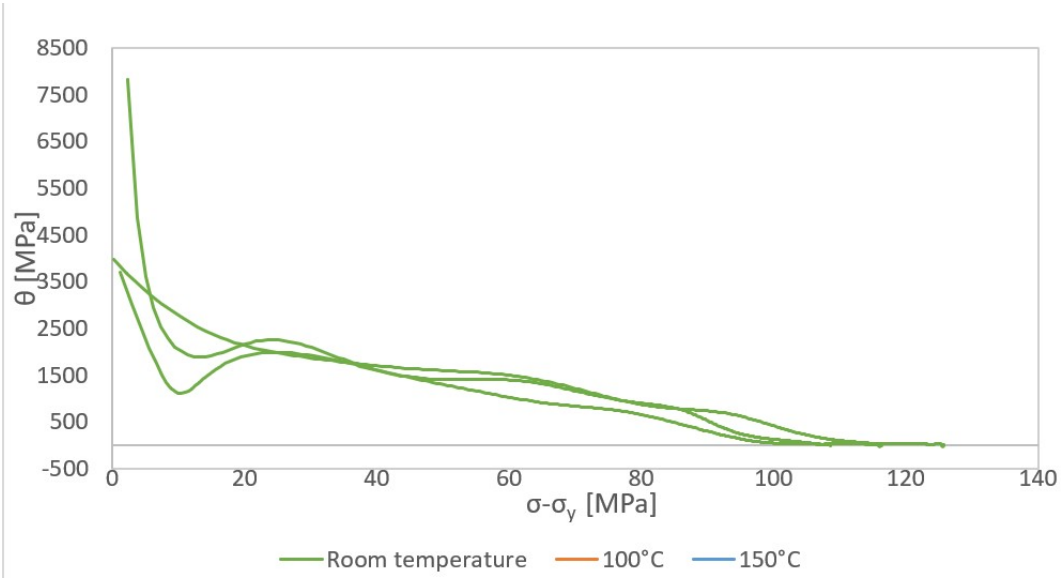

Figure B.20: Kocks-Mecking curves for alloy M, aging time 20 minutes

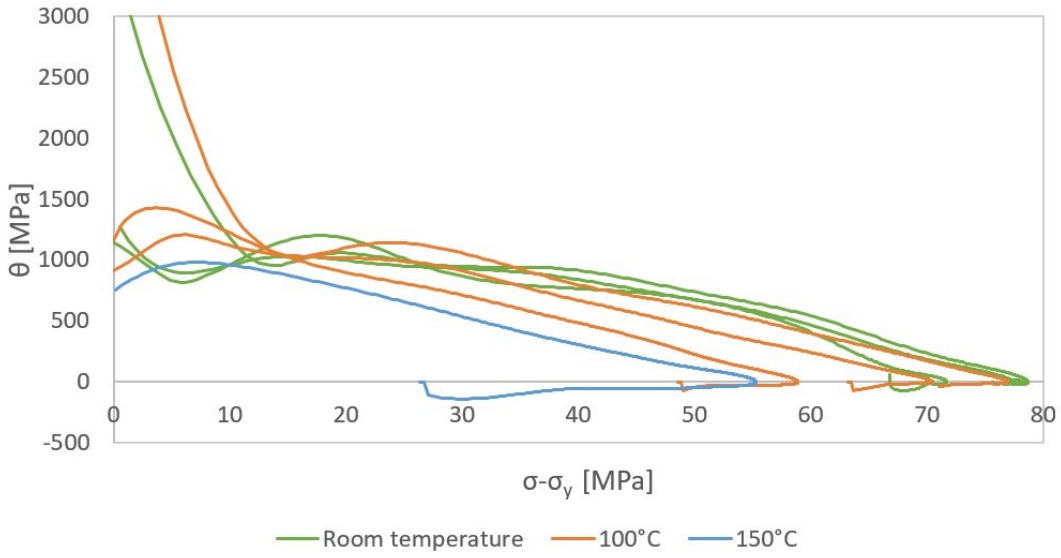

Figure B.21: Kocks-Mecking curves for alloy M, aging time 1 hour

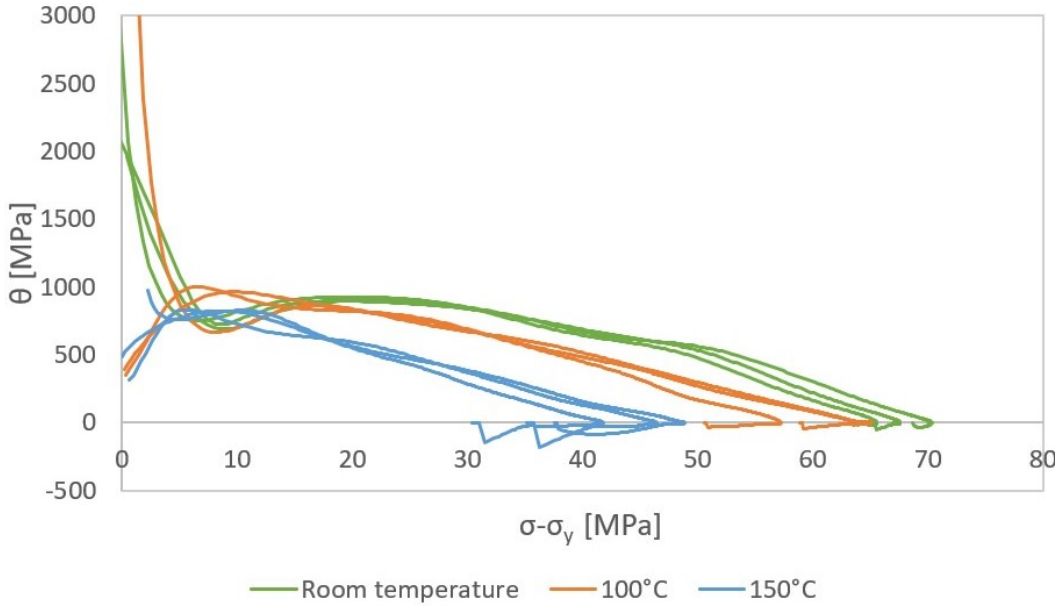

Figure B.22: Kocks-Mecking curves for alloy S, aging time 3 hours

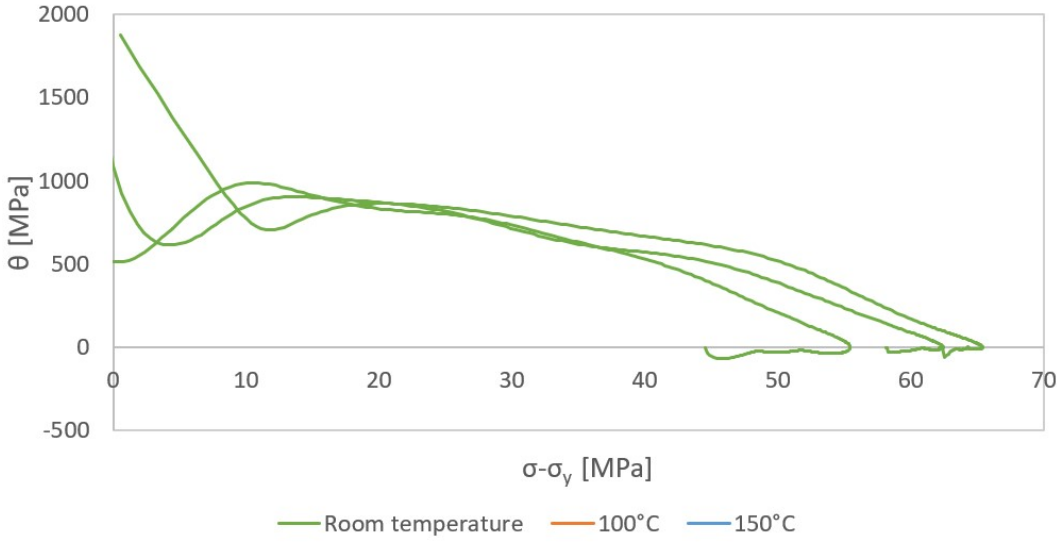

Figure B.23: Kocks-Mecking curves for alloy M, aging time 5 hours

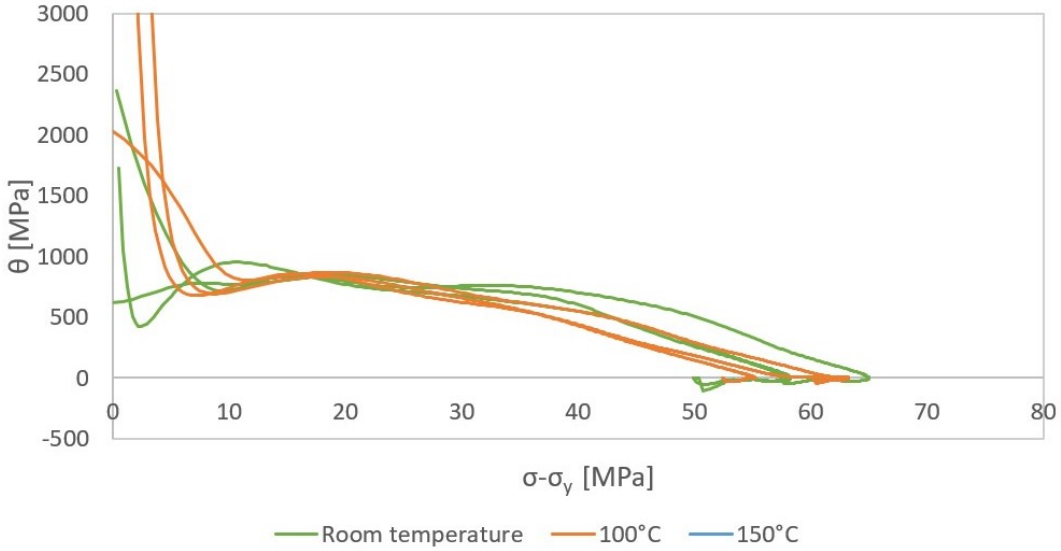

Figure B.24: Kocks-Mecking curves for alloy M, aging time 12 hours

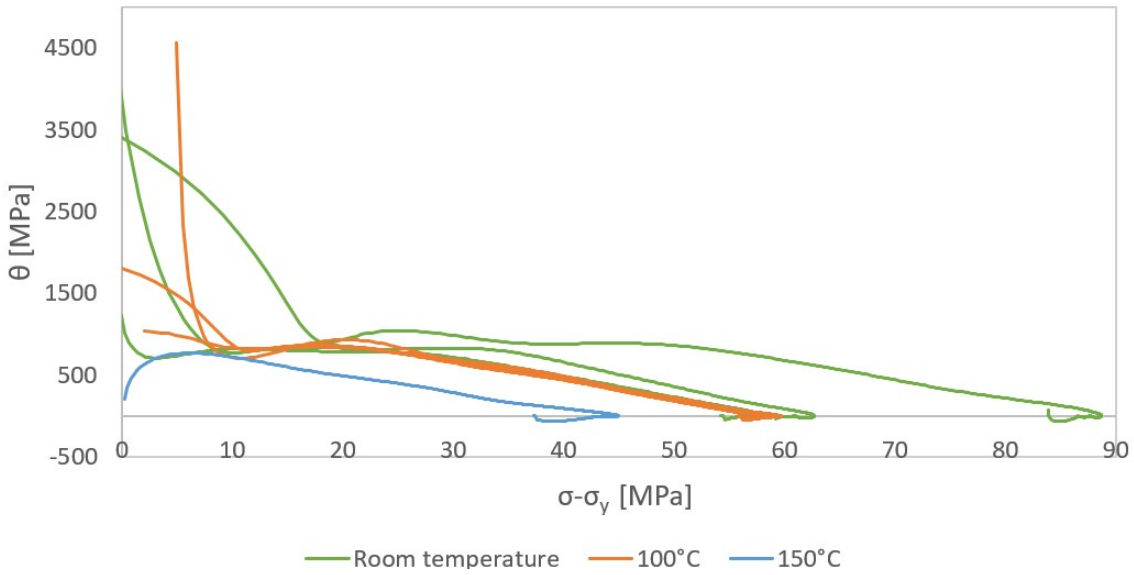

Figure B.25: Kocks-Mecking curves for alloy M, aging time 24 hours

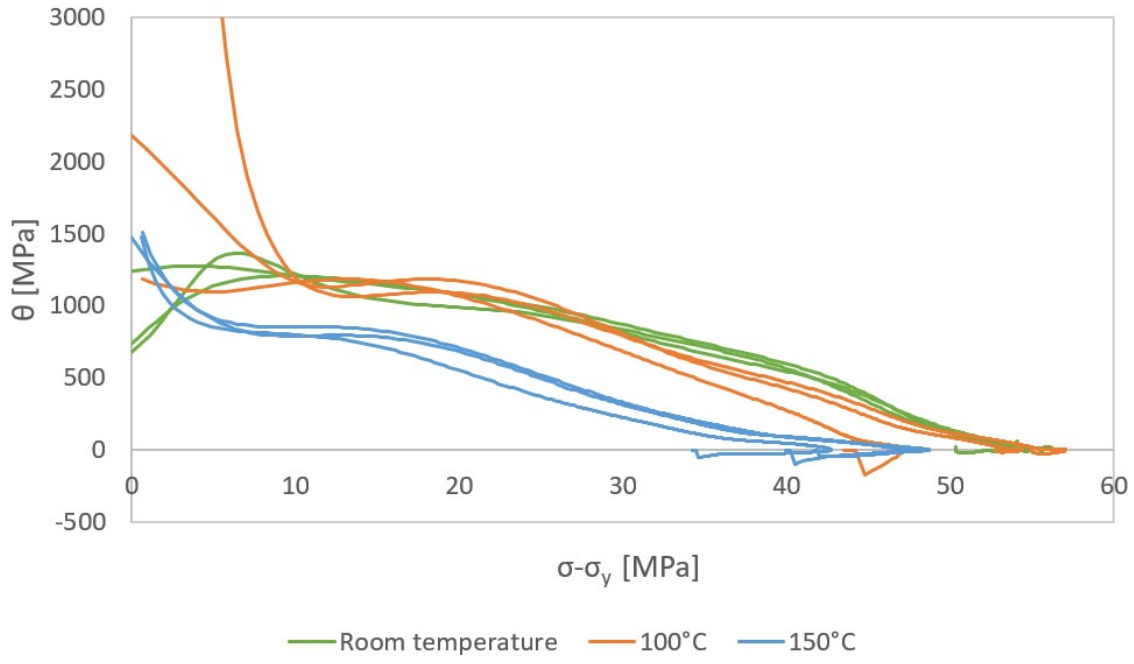

Figure B.26: Kocks-Mecking curves for alloy M, aging time 1 week

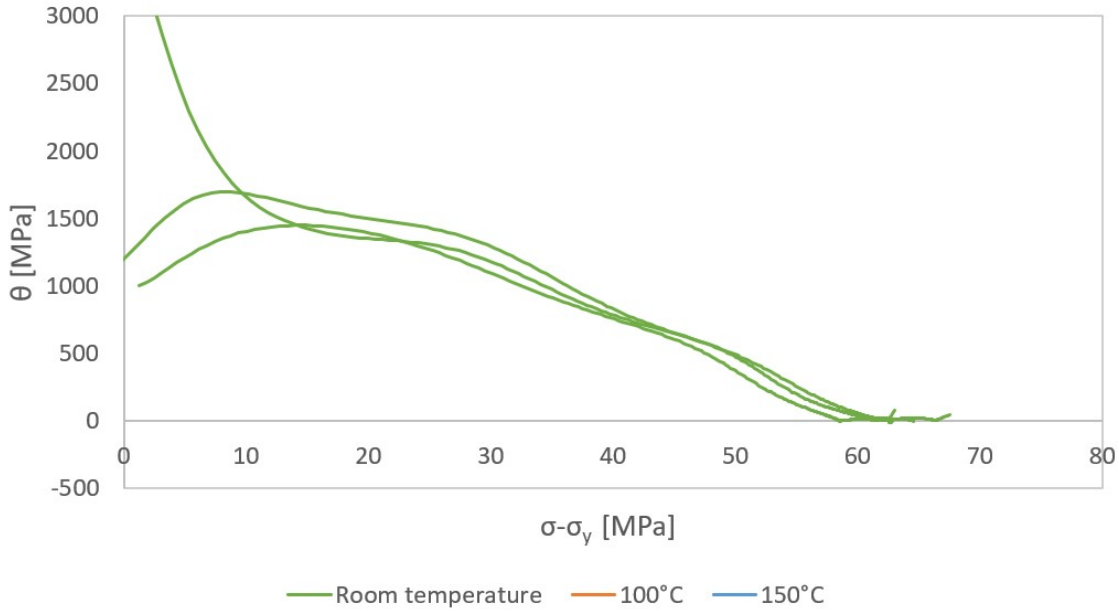

Figure B.27: Kocks-Mecking curves for alloy M, aging time 2 weeks

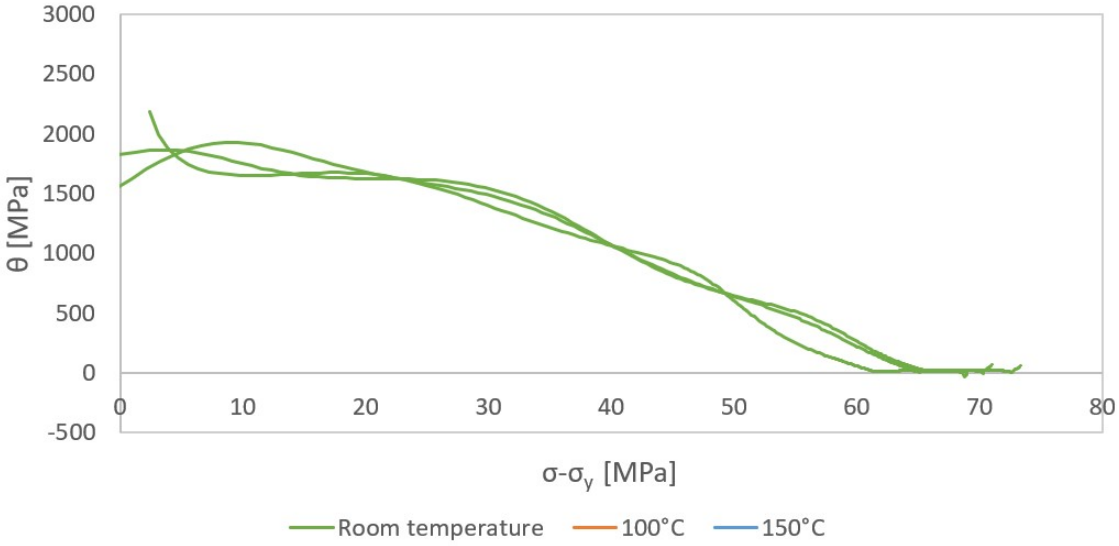

Figure B.28: Kocks-Mecking curves for alloy M, aging time 1 month